DESIGN PRINCIPLES AND DEVELOPMENTS OF INTEGRATED SOLAR FLOW BATTERIES

by

WENJIE LI

A dissertation submitted in partial fulfillment of

the requirements for the degree of

DOCTOR OF PHILOSOPHY

(CHEMISTRY)

at the

UNIVERSITY OF WISCONSIN-MADISON

2019

Date of final oral examination: September 4th, 2019

The dissertation is approved by the following members of the Final Oral Committee:

Song Jin, Professor, Chemistry
Kyoung-Shin Choi, Professor, Chemistry
Shannon Stahl, Professor, Chemistry
Dane Morgan, Professor, Materials Science and Engineering

PREFACE

DESIGN PRINCIPLES AND DEVELOPMENTS OF INTEGRATED SOLAR FLOW BATTERIES

WENJIE LI, PH.D.

UNIVERSITY OF WISCONSIN-MADISON

2019

The tremendous amount of solar energy received by the earth makes it the most appealing renewable energy source. However, challenges posed by the intermittency of solar energy source necessitate the integration of efficient solar energy conversion with scalable energy storage systems. This thesis revolves around the study and development of solar flow batteries (SFBs), a novel approach that integrates solar energy conversion and electrochemical storage. The unique integrated design of SFBs offers a practical solution to provide uninterruptable power supply on demand by a single standalone device regardless of the ebb and flow of solar irradiation. Although connecting photovoltaics (PVs) with batteries, as adopted by some solar farms nowadays, can provide the same uninterruptable power supply, the high capital cost and large footprint of two separate devices limit the market cases feasible for this option. In contrast, monolithically integrated SFBs may represent a more compact, and cost-effective approach for off-grid electrification. My graduate research has focused on three interconnected aspects for SFBs: (1) understanding the operation mechanisms of SFB devices; (2) developing the design principles and modeling methods to maximize the performance of SFBs; (3) the demonstration and device optimization of SFBs.

Chapter 1 reviews fundamental working principles, characterization methods, mechanistic understandings and research advancements of SFBs. First, I discuss the working mechanism of SFBs and the two most important building blocks for SFBs: redox flow batteries (RFBs) and photoelectrochemical (PEC) cells. The electrochemical theory governing cell potential of RFBs and photovoltage of photoelectrodes is also quantitatively described. Then, I present a set of experimental protocols for characterizing redox couples, RFBs, photoelectrodes and SFBs to promote comparable assessment and discussion of important figure of merits of SFBs. Solar-to-output electricity efficiency (SOEE) is the round-trip energy efficiency of SFBs, to which I have devoted the most attention. To reveal the design principles for highly efficient SFB devices, I introduce a quantitative simulation method for SFBs and discuss insights generated from such simulations. Next, I review the historical and recent development of SFBs and identify the state-of-the-art demonstrations at each development stage with more emphasis on our own research efforts in the development SFBs built with PV cell photoelectrodes. Finally, I preview some promising future studies for improving both the scientific and technical understandings of SFBs.

Chapter 2 follows up on the groundwork laid in Chapter 1 by presenting our first proof-of-concept SFB demonstration by integrating regenerative silicon solar cells and 9,10-anthraquinone-2,7-disulfonic acid (AQDS)/1,2-benzoquinone-3,5-disulfonic acid (BQDS) redox cuuples. I describe the general design along with the operation principles for SFBs that consist of two photoelectrodes and two inert electrodes. The integrated device can be directly charged by solar light without external bias, and discharged like normal RFBs with an energy storage density of 1.15 Wh/L. More importantly, I introduce the new figure of merit, solar-to-output electricity efficiency (SOEE), specifically for characterizing the time-shifted energy conversion efficiency of SFBs. Our first prototype SFB device showed an average SOEE of around 1.7% over ten cycles without significant performance optimization. The concept demonstrated herein exploits a previously undeveloped design connecting two major energy technologies and promises a general approach for storing solar energy electrochemically with high theoretical storage capacity and efficiency.

Chapter 3 builds upon comprehensive mechanism study and deeper understanding of the operation principles of SFBs. In light of the mechanistic understanding, I developed a set of design principles for highly efficient integrated SFB devices. The most crucial idea behind these principles is that, with the available high performance solar cells and RFBs, the RFB cell voltage should be matched as close as possible to the maximum power point of the photoelectrode, which demands carefully chosen redox couples and photoelectrode materials. Such rational design principles led to the successful demonstration of a high performance SFB device with highly efficient and high photovoltage tandem III-V solar cells and high voltage 4-OH-TEMPO/MV RFBs. Enabled by high efficiency photoelectrode, properly matched redox couples, and carefully designed flow field architecture, a record SOEE of 14.1% has been achieved for the SFB. More importantly, this study lays out the design pathway for us to achieve even higher SOEE, potentially using much less expensive solar cell materials.

Chapter 4 focuses more on improving the lifetime of SFBs, which, though very important, has received much less attention than efficiency. Generally, two major challenges could prevent SFBs from reaching long device lifetime: instability of redox couples and corrosion of photoelectrodes by electrolytes. In collaboration with Prof. Michael Aziz and Prof. Roy Gordon's team at Harvard University that provided us with stable organic redox molecules (BTMAP-

Vi/BTMAP-Fc), I carefully studied the device failing mechanisms and applied the understanding to design robust organic redox molecules, low corrosiveness neutral electrolytes, and stable photoelectrodes for long lifetime SFBs. These efforts have successfully extended the continuous operation lifetime of Si photoelectrode based SFB device from 10 hours to longer than 200 hours. By employing the SFB design principles discussed in Chapter 3 and further the newly developed concept of instantaneous SOEE ($\mathrm{SOEE_{ins}}$), we boosted the SOEE from the 1.7% for our first prototype presented in Chapter 2 more than three-fold to 5.4% in this SFB using the same silicon photoelectrodes.

Inspired by the previous SFB demonstrations using III-V tandem junction solar cells (Chapter 3) and Si single junction solar cells (Chapter 4), in Chapter 5, I present the design of $(\mathrm{FAPbI_3})_{0.83}(\mathrm{MAPbBr_3})_{0.17}$ perovskite/silicon tandem junction solar cells specifically for aqueous organic SFBs that takes advantage of not only highly efficient tandem junction design for achieving high efficiency but also the robust silicon semiconductor electrolyte contact for high stability. I also discribe a new modeling method to analyse the best matched redox couples for the perovskite/Si cells, which guided us to the selection of BTMAP-Vi/$\mathrm{N^{Me}}$-TEMPO redox couples. I show that these efforts have not only led to a new record solar-to-output electricity efficiency (*SOEE*) of 14.9% for SFBs, but also expanded the performance dimensions that can be well-covered by a single SFB device, including device lifetime, capacity utilization rate, power conversion efficiency utilization rate, and low cost.

The following appendices provide complementary information to the work presented in the main chapters. Specifically, Appendix 1, 2, 3, and 4 provide additional figures and tables pertaining to Chapters 2, 3, 4, and 5, respectively.

The body of thesis presented here constitute a significant advance toward a compatible approach for harvesting, storing and utilizing the intermittent solar energy with high energy conversion efficiency and energy storage density. With our continuously evoling understanding of SFBs, I have pushed the boudaries along various dimentions for SFBs. The conceptual breakthrough and technological advancements presented here not only shed light on the future developments of SFBs, but also should translate to other integrated solar rechargeble battery devices, offering strategies for improving the performance of those devices.

ACKNOWLEDGMENTS

I still can’t believe five years have gone so fast and I am standing at the end of my graduate school journey now.

First and foremost, I must dedicate my deepest gratitude to my father Renqiu Li and my mother Lvping Liu. My career as a chemist started from the balcony at home, where I practiced standard technics that I am still using today as well as crazy random experiments that I don’t want to try again. Although my parents probably didn’t know much about what I was setting up by the sink, they always trust me and are willing to provide any support that I might need. Thank you, for your constant supports that carry me through the long journey from the balcony lab to where I am now, for your encouragements that make me ready to take on the next challenge, and for the family you created with your endless love. I also need to thank my amazing sister, Wenhui Li, who keeps me accompanied for countless summer break days and only occasionally beats me up.

I must also express my sincere appreciations to my PhD advisor, Professor Song Jin, who has helped me grow as a scientist and as a person with his exceptional coaching. I have always been impressed by his passion and enthusiasm, which was the biggest source of encouragement I had in graduate school that kept me excited about science and discoveries. The trust and freedom he granted to me to explore my own research interests together with his most detailed dedication and advices have shaped my graduate study in an extraordinary way that I never anticipated. I hope I can pass on the passion, knowledge and skills Song taught me to more young students.

I would like to acknowledge my committee members, Professor Dane Morgan and Professor Kyoung-Shin Choi for being on my committee all of these years and providing critical comments, valuable advices and warm encouragements. I would also like to thank the other member of my reading committee, Professor Shannon Stahl. It has been a great opportunity for me to work with him and his team on the redox reservoir project. I have learned immeasurable lessons through my interaction and meetings with him.

During my graduate study, I have been working with many collaborators, who made important contributions to the research work presented in this dissertation. For the demonstration of SFBs, Prof. Jr-Hau He and Dr. Hui-Chun Fu from King Abdullah University of Science and Technology have made crucial contributions to the fabrication of silicon and III-V photoelectrodes, and I appreciate their support and patience in the starting stage of my graduate study. I thank Prof. Michael Aziz, Prof. Roy Gordon, Dr. Marc-Antoni Goulet and Emily Kerr from Harvard University for providing redox couples and sharing many useful instructions and insightful discussions on general redox flow battery operating principles. I also appreciate the help from Prof. Leo Liu and Bo Hu from Utah State University for providing additional redox couples. Furthermore, it would not have been possible for me to carry out the research on perovskite/Si tandem junction cells without the help from Prof. Anita Ho-Baillie and Dr. Jianghui Zheng form University of New South Wales. In addition, I would like to thank everyone in the machine shop, electronics shop and glass shop, especially Tracy Drier, Steve Myers, and Kendall Schneider for realizing many generations of my special electrochemical device designs.

I am indebted to all members of the Jin Group, past and present. I treasure the time, help, care, friendship, inspirations and enjoyments they shared with me in the group. In particular, I would like to thank my mentor, Dr. Linsen Li, who is someone I always look up to, during and after his time in UW-Madison. Linsen has influenced me in many ways with his deep passion for science and incredible patience to my detailed questions. I must also acknowledge senior members in Jin group, Dr. Miguel Cabán-Acevedo, Dr. Leekyoung Hwang, Dr. Audrey Forticaux, Dr. Qi Ding, Dr. Melinda Shearer and Dr. Matthew Stolt, who provided invaluable training to me in many aspects when I was trying to find my feet in graduate school. Special thanks to Dr. Yongping Fu for countless insightful discussions through the last five years. Furthermore, I am grateful to my awesome and always helpful classmate Dr. Lianna Dang, people that I shared potentiostat experiences with, Dr. Yifan Dong, Hongyuan Sheng, Dr. Ying Yang and Atilla Veyssal, and other people that I have been closely working with, Dr. Dong Liang, Kyle Czech, Nitish Mathur, Matthew Hautzinger, Dongxu Pan, Natalia Spitha, Abe Wu (Ge group), Tim Tiambeng, David Roberts, Chris Roy and Dominic Ross. I would especially like to thank Yuzhou Zhao, who was constantly ready to debate about my brilliant scientific ideas, worked with me on various technical projects during late lab hours, and took shaky footage of my snowboarding skills.

Certainly, the last five years would not have been so enjoyable without the support and encouragement from my friends both in Madison and elsewhere. The many new friends in Madison have made this foreign city a warm place for me to live and explore. I enjoyed every bubble tea trips, movie nights, hot pot parties and snow adventures. In addition, I would like to thank many remote friends, in particular, Dr. Pu Duan, Yudi Ding, Dr. Ziwei Guo, Dr. Hongbin Liu, Dr. Xiangwen Gao and Shuqi Zhang for sharing enjoyable moments and providing constant supports.

And lastly, I must express my special appreciation to Zhili (Stella) Tang, for cheering my accomplishments, listening to my complaints, and most importantly, spending many normal days with me. She is the one that enables my potential with her pure and simple love.

Wenjie Li, 08/27/2019

TABLE OF CONTENTS

CHAPTER 1 DESIGN PRINCIPLES FOR INTEGRATED SOLAR FLOW BATTERIES

CHAPTER 2 INTEGRATED PHOTOELECTROCHEMICAL SOLAR ENERGY CONVERSION AND ORGANIC REDOX FLOW BATTERY DEVICES

CHAPTER 3 14.1%-EFFICIENT MONOLITHICALLY INTEGRATED SOLAR FLOW BATTERY

CHAPTER 4 A LONG LIFETIME AQUEOUS ORGANIC SOLAR FLOW BATTERY

CHAPTER 5 PEROVSKITE/SILICON TANDEM SOLAR CELL POWERED HIGH PERFORMANCE SOLAR FLOW BATTERY

APPENDIX 1 SUPPLEMENTARY INFORMATION FOR CHAPTER 2

APPENDIX 2 SUPPLEMENTARY INFORMATION FOR CHAPTER 3

APPENDIX 3 SUPPLEMENTARY INFORMATION FOR CHAPTER 4

APPENDIX 4 SUPPLEMENTARY INFORMATION FOR CHAPTER 5

LIST OF FIGURES

LIST OF TABLES

CHAPTER 1

Design Principles for Integrated Solar Flow Batteries

1.1 Abstract

Due to the intermittent nature of sunlight, practical round-trip solar energy utilization systems require both efficient solar energy conversion and inexpensive large-scale energy storage. Conventional round-trip solar energy utilization systems typically rely on the combination of two or more separated devices to fulfill such requirement. Integrated solar flow batteries (SFBs) are a novel type of devices that integrate solar energy conversion and electrochemical storage. In SFBs, solar energy is absorbed by photoelectrodes and converted into chemical energy by charging up redox couples dissolved in electrolytes in contact with the photoelectrodes. To deliver electricity on demand, the reverse redox reactions are carried out to release chemical energy stored in redox couples as one would do in the discharge of a normal RFB. Enabled by its the unique integrated design, all the functions that are demanded by round trip solar energy utilization systems can be performed by a single SFB device. Leveraging rapidly developing parallel technologies of photovoltaic cells and redox flow batteries (RFBs), significant progress has been made in the field of SFBs in the last few years. This *Account* aims to provide a general reference and tutorial for researchers that are interested in SFBs, and help to facilitate the development of this field.

The operation principle of SFBs is built on the working mechanism of RFBs and photoelectrochemical (PEC) cells. We describe the basic concept and important features of RFBs and redox couples. Emphasis is placed on the quantitative understanding of RFB cell potentials. We also introduce different type of photoelectrochemical cells and highlight two different

photoelectrode designs that are commonly seen in SFB literatures: simple semiconductor photoelectrodes and PV cell photoelectrodes. A set of experimental protocols for characterizing redox couples, RFBs, photoelectrodes and SFBs are presented to promote comparable assessment and discussion of important figure of merits of SFBs.

Solar-to-output electricity efficiency (SOEE) is the round trip energy efficiency of SFBs and has received substantial research focus. We develop a quantitative simulation method to find the relationship between device SOEE and cell potential, and reveal the design principles for highly efficient SFBs. We review the historical development of SFBs and identify the state-of-the-art demonstrations at each development stages with more emphasis on our own research efforts in the development SFBs built with PV cell photoelectrodes. In the end, we preview some promising future studies for improving both the scientific and technical understandings of SFBs.

1.2 Introduction

The increasing efforts devoted to adopting solar energy as a clean and renewable energy source have created major challenges for electrical grid stabilization due to the intermittent and diffuse nature of sunlight. To this end, three major functions are generally pursued in practical round trip solar energy utilization: solar energy conversion, storage and delivery. Completing these functions typically rely on the combination of two or more separated devices, such as photovoltaic (PV) cells and reversible batteries, or photoelectrochemical (PEC) solar fuel generation devices and fuel cells.[1,2] Recently, integrated solar flow batteries (SFBs) has emerged as a novel approach and received growing research interests.[3] SFBs monolithically integrate efficient solar semiconductors with redox flow batteries (RFBs) by sharing the same electrolytes and redox couples. Such design combines the function of each individual components so that the three major steps mentioned above can be performed on demand in a single device. Compared with the approaches that rely on separated devices, SFBs may represent a more compact and cost-effective approach for off-grid electrification.

Although the fundamental working principles of integrated PEC solar energy conversion and electrochemical energy storage were demonstrated as early as 1970s[4] with integrated solar rechargeable batteries, the lack of "flowing electrolytes" clearly differentiates them from SFBs.[5,6] Similar to the case in RFBs, the "flowing electrolytes" in SFBs decouples the energy conversion and storage components, which allows for easily scaling up the energy storage capacity of SFBs by using bigger electrolyte storing tanks. The early prototype SFBs were demonstrated by the integration of dye sensitized solar cell (DSSC) and non-aqueous redox couples, however, with extremely low operating currents (<0.1 mA/cm^2) and efficiencies (< 0.1%).[7,8] Since then, considerable research has been carried out towards higher device performance and deeper mechanistic understanding. [9-11] For example, the device design using separated photoelectrochemical/RFB chambers[12] are replaced by monolithically integrated device design,[13] the choices of redox couples are greatly expanded,[3] the match between solar components and redox couples are better rationalized,[14] and the characterization methods are further developed.[15] As a result, SFBs demonstrated nowadays can deliver much higher efficiency and larger capacity with longer lifetime and lower cost. [16]

Our research work in the field of SFBs are mainly focused on the following three interconnected aspects: (1) understanding the operation mechanisms of SFB devices; (2) developing the design principles and modeling methods to maximize the performance of SFBs; (3) the demonstration and device optimization of SFBs. However, after several year's research, we find the field is still in its infancy with a diverse set of nomenclatures, device designs, experimental methods and technological maturities. The scattered information in the literature complicate the fair comparison between SFBs and may also impede further developments in this field. Therefore, in this *Account* we present unified nomenclatures and comprehensive comparison between different device designs with the goal of providing clarity and consistency to the discussion of SFBs. More importantly, we identify key parameters of SFBs and establish a set of experimental protocols for comparable characterization of these parameters and concise identification of the state-of-the-art SFB designs. Building on the understanding of the operation mechanisms of SFBs, we reveal the design principles underlying the state-of-the-art demonstrations and discuss the pathways for future improvements. We hope these efforts can bring the scattered pieces in SFB literatures together and present a holistic viewpoint on the field of SFB. The aim of this *Account* is to serve as a general reference and tutorial for researchers who are trying to push the boundaries of SFB research, as well as beginners who are interested in learning more about this field.

1.3 Working mechanism of SFBs and their components

RFBs and redox couples. Some researchers like to consider SFBs a special type of RFBs. This is partially true because, for most of SFB demonstrations, the device platform and redox couples are directly adopted from RFBs (Figure 1.1).[17,18] The RFB device (Figure 1.1a) consists of an energy converting unit, where the electrical energy is reversibly converted to chemical energy (charging) and vice versa (discharging). In such energy converting unit, the electrons (or holes) can reduce (or oxidize) redox couples in liquid electrolytes and the electrical energy can be stored as chemical energy during charging and released during discharging.[19] Additional electrolytes are stored in external tanks and pumped through the cell to charge or discharge the battery. The use of liquid electrolytes in RFBs allows convenient and low-cost scale up of the energy storage capacity without larger cells, such as the case for Li-ion or other solid-state batteries; instead, scaling up the energy capacityonly entails increasing the amount of redox active species in storage tanks without scaling up the power generation components. The energy storage capacity is limited only by the size of the tanks, making scale-up relatively easy, with cost-per-unit of energy storage generally lower than non-flowing and solid-state batteries (such as Li-ion batteries), which makes them more attractive at larger scale.[17] Such advantage also holds true for SFBs (Figure 1.1b) because SFBs and RFBs share the same decoupled power/energy device design.

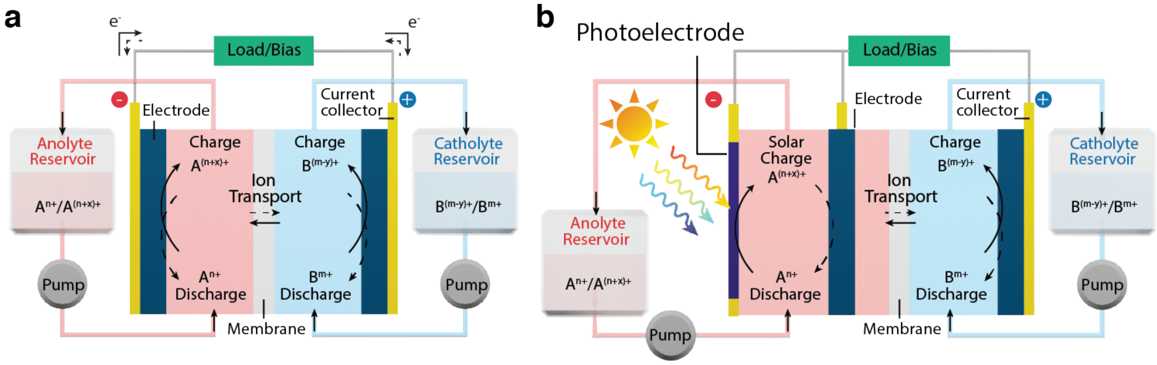

Figure 1.1. Schematic structure of typical RFB and SFB devices. a. Schematic design of a typical RFB device that consists of decoupled cell stack and electrolyte reservoirs. **b.** Schematic design of a typical SFB device that monolithically integrates a RFB and a photoelectrode.

For both RFBs and SFBs, one major scientific challenge lies in the design of proper redox couples.[17,20] These redox active species dissolved in anolyte and catholyte not only directly determine the cell potential and energy density of SFBs, but also have significant influence on the performance and stability of photoelectrodes.[21] The discussion below introduces some basic concepts of redox couples in RFBs and SFBs with the assumption that the redox species concentration (C), volume and number of electrons transferred in redox reactions (n) of anolyte and catholyte are equal.

The formal potential (E^0) of a redox couple is the measured potential (*vs.* reference electrode) of a redox couple pair in unity ratio under the designated condition (such as certain supporting electrolyte concentration). The formal cell potential (E^0_{cell}) is thus given by:

$$E^0_{cell} = E^0_{anode} - E^0_{cathode}, \tag{1}$$

where E^0_{anode} and $E^0_{cathode}$ are the formal potentials of anolyte and catholyte redox couples, respectively. Note that we define positive electrode (higher E^0) as anode and negative electrode (lower E^0) as cathode to align with the discussion of photoelectrodes later, which is opposite to that in some RFB literatures.[19] The concentration of oxidative (ox) and reductive (red) species changes due to charging/discharging of the device and we can use state-of-charge (SOC) to quantify such concentration change:

$$SOC = \frac{C^{ox}_{anode}}{C^{ox}_{anode}+C^{red}_{anode}}\ (or\ \frac{C^{red}_{cathode}}{C^{oxi}_{cathode}+C^{red}_{cathode}}).^{22} \tag{2}$$

Accordingly, the equilibrium cell potential (E^{eq}_{cell}, also often referred as open circuit voltage, OCV) also changes, which can be estimated by Nernst equation:

$$E^{eq}_{cell} = E^{eq}_{anode} - E^{eq}_{cathode} = E^0_{cell} - \frac{RT}{nF}\ln\left[\frac{1-SOC}{SOC}\right]^2, \tag{3}$$

where E^{eq}_{anode} and $E^{eq}_{cathode}$ are the equilibrium potential of anolyte and catholyte redox couples, respectively, R is standard gas constant, T is temperature (in K), n is number of electrons transferred, F is the Faraday constant.[22,23] The energy density U of RFBs/SFBs is given by: $U = \frac{nFCE^0_{cell}}{N}$, where C is the concentration of redox couples, N is the number of reservoirs (typically equals 2).[19] It can be seen that the solubility and E^0 of redox couples determine the theoretical limit of U. Another important aspect to consider is the reaction kinetics of the redox couples, which is governed by standard rate constant (k^0) and diffusion coefficient (D). To design high performance

SFBs, the key requirements for redox couples are: 1) suitable E^0 (will be discussed in detail later); 2) facile redox kinetics; 3) robust chemical and electrochemical stability; 4) non-corrosive and compatibility with semiconductor; 5) high solubility; 6) low cost.

Photoelectrodes are the solar energy conversion components in SFBs that set the limit of the overall device efficiency. Regardless of the diverse designs of photoelectrodes reported in SFB literatures, the device operation principles are in fact very similar. Here we first consider the most fundamental scenario: simple semiconductor-liquid junction cells (as shown in Figure 1.2a). In these cells, illumination of semiconductors results in the excitation of electrons and holes, and the photoexcited minority carriers can oxidize (for n-type semiconductors) or reduce (for p-type semiconductors) redox couples with appropriate formal potentials on semiconductor surface to allow the photo-generated carriers to be collected; while the photo-generated majority carriers will migrate to the bulk of the semiconductors, get collected and flow through the external circuit of the cells to the counter electrode to regenerate the redox couples. Because redox couples are recirculated between semiconductors and counter electrodes, this type of cells is often called regenerative solar cells.[24] We can further add an ion-selective membrane between the semiconductor and counter electrode to create two separated chambers and use two different redox couples in these chambers (Figure 1.2b). In these cells, because redox couples can't migrate through the membrane and get regenerated, they will be accumulated as the charged form (oxidize form on n-type semiconductors and reduce form on corresponding counter electrodes). PEC fuel generating cells are usually constructed with such configuration using consumable redox species (such as H_2O for PEC water splitting cells or CO_2 for CO_2 reduction cells).[25,26] On the other hand, for SFBs, these redox species are reversible redox couples so that the accumulation of these redox couples can result in an increasing cell potential between the two chambers (equation 3) as a means to store solar energy.

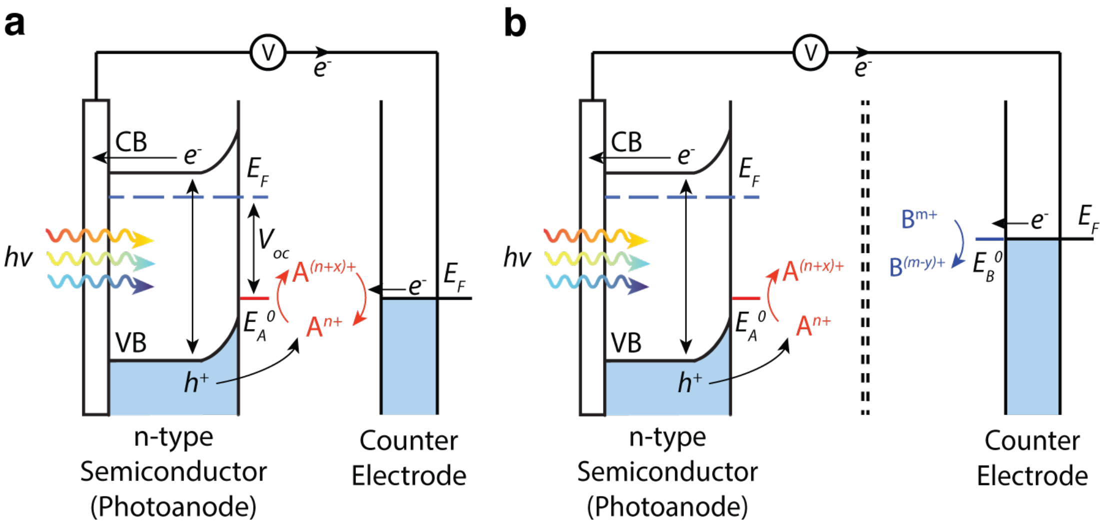

Figure 1.2. Working principle of two different type of PEC cells. **a**, Working principle of a PEC regenerative liquid junction cell with a n-type semiconductor photoanode and one redox couple. Redox species A^{n+} are oxidized to $A^{(n+x)+}$ by photogenerated holes on photoanode, while $A^{(n+x)+}$ are reduced back to A^{n+} on counter electrode. The overall effect is the direct out-put of electricity. **b**, Working principle of a photoelectrosyntheic cell with a n-type semiconductor photoanode and two redox couples. Redox species A^{n+} are oxidized to $A^{(n+x)+}$ by photogenerated holes on photoanode, while redox species B^{m+} in the other chamber are reduced to $B^{(m-y)+}$. The overall effect is accumulation of $A^{(n+x)+}$ and $B^{(m-y)+}$, or photoelectrolysis of consumable A^{n+} and B^{m+} species.

In the aforementioned PEC semiconductor-liquid junction cells, the open circuit potential (V_{oc}) of photoelectrodes is mainly determined by potential difference between E_{eq} of the redox couples in contact with the photoelectrodes and the Fermi level (E_F) of the photoelectrodes. A high V_{oc} thus requires both large semiconductor bandgap (E_g) and well matched redox couple E_{eq}. What complicates such design is that large E_g often leads to sacrifice in light absorption range and photocurrent. Consequently, E_g needs be carefully optimized for best overall power conversion efficiency (PCE) of photoelectrodes.[21] (Note that, DSSC photoelectrodes used in some early SFB demonstrations also fall into this category.) To avoid such complexity, photoelectrodes with internal solid-state p/n junctions (or buried junctions) have been employed in some SFB demonstrations. Unlike that of semiconductor-liquid junction cells, the V_{oc} of the photoelectrodes with solid-state junctions arises from the Fermi level difference between the solid semiconductor materials that are in contact internally, thus the V_{oc} is independent of the nature of solid-liquid junction. Hence, such photoelectrodes exhibit almost identical V_{oc} regardless of what redox couples are used to form the external solid-liquid junction. Because these photoelectrodes are often fabricated from photovoltaic cells (PVs), a previous taxonomy report suggests calling them PV-biased electrosynthetic cells.[24] The use of PV cells in SFBs separates the properties of photoelectrodes and the other components of SFBs, allowing for independent study and optimization of them. To date, the photoelectrodes of record holding SFBs are all fabricated from PVs.[14-16] However, it should be noted although PV cells are good for mechanistic study and proof-of-concept demonstration of high performance SFBs, they usually have much higher manufacturing cost than simple semiconductors.[27,28] We think both designs are worth studying for future developments of SFBs in different directions.

Working mechanism of SFBs. The schematic illustrations of RFB (Figure 1.1) and photoelectrosynthetic cell (Figure 1.2b) show great structural similarities between these two devices: two chambers separated by a membrane, the use of liquid electrolytes and reversible redox reaction in each chamber. Integrating these two separated devices into a monolithic SFB thus come naturally. As illustrated in Figure 1.1b, the general design for typical integrated solar flow battery devices consists of three electrodes, namely a photoelectrode, an inert cathode and an inert anode. In such integrated SFB devices, solar energy is absorbed by semiconductor photoelectrodes and the photoexcited carriers are collected at the semiconductor-liquid electrolyte interface to convert the redox couples in the electrolytes to fully charge up the device (i.e. store the solar energy into the electrolytes). This process is basically the same as that in photoelectrosyntheic cells (Figure 1.2b). Depends on the specific photoelectrodes used, the SFBs can have either two photoelectrodes (two side illumination)[12,13,15] or one photoelectrode.[14,16] When electricity is needed, the charged up redox couples will be discharged on the surface of inert electrodes as one would do in the discharge of a normal redox flow battery to generate electricity. The electrodes are connected differently in energy delivery and storage mode: the cathode and anode are connected with an external load to discharge the SFB (Figure 1.3a), while the photocathode and photoanode are connected to allow solar-driven unassisted device recharge (Figure 1.3b). We can also operate this device just as a PV solar cell by cycling the redox couples between the photoelectrodes and the counter electrodes that are in the same chamber to directly extract the electricity out, which is how regenerative photoelectrochemical solar cells work (Figure 1.2a and 1.3c). Because external bias is not needed under any configurations, SFBs can work stand-alone.

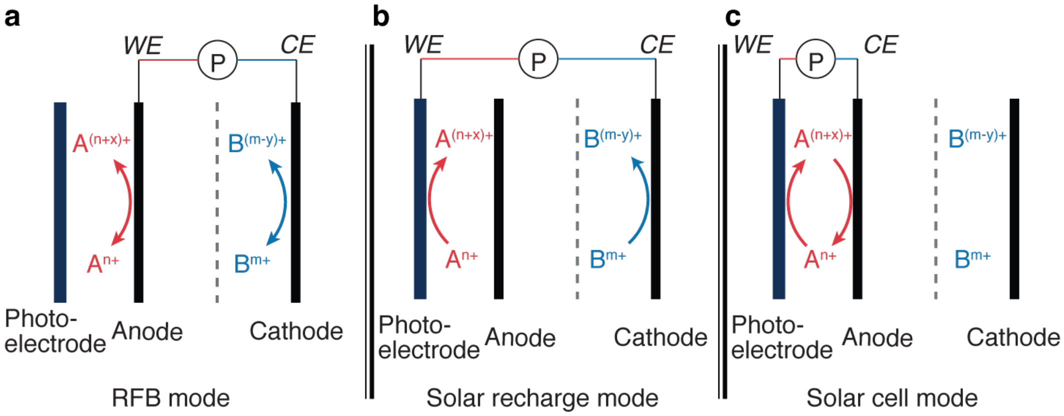

Figure 1.3. Operation modes of SFBs. **a**, RFB mode that allows for charring/discharging of both redox couples A and B on inert electrodes. **b**, Solar recharge mode that allows for photocharging redox couple A and B on photoelectrode and inert electrode, respectively. **c**, Solar cell mode that allows for photocharging and simultaneous discharging of the same redox couple A on photoelectrode and inert electrode, respectively.

1.4 Characterization methods for SFBs

To promote comparable characterization and discussion of SFB, herein we suggest these typical characterization methods to be used as standard practices in SFB studies.

RFBs and redox couples. Because we are specifically interested in "fast redox" couples that undergo reversible redox reactions, the discussion below are all based on reversible redox reactions unless otherwise specified. The electrochemical performance of redox couples are typically studied with a 3-electrode setup using a working electrode, a reference electrode and a counter electrode. With such setup up, cyclic voltammetries (CVs) are first performed in a wide voltage range (typically the stability range of the solvent) to find possible redox features and then switched to a narrow range to study the individual redox reactions and estimate E^0 of each redox reaction from the average potential of anodic and cathodic peaks in CV: $E^0 = ½ (E_{pa} + E_{pc})$, where E_{pa} and E_{pc} are anodic and cathodic peak potentials, respectively (Figure 1.4a). By varying scan rate in CVs, the kinetics properties (D and k^0) of redox couples can also be quantitatively estimated using *Randles-Sevèik equation* and *method of Nicholson*.[23] However, because the existence of charging current overlapping with Faradic current and uncompensated resistance, kinetics information obtained from CV is usually not very accurate. Thus, CV usually only serve as a quick diagnostic tool for the redox kinetics. To study the redox kinetics in a more careful manner, rotating-disk electrode (RDE) can be used, in which the working electrode is rotated at different speeds to obtain the current-voltage (*I-V*) responses under controlled stead-state conditions. Either CV or linear scan voltammetry (LSV) can be used in RDE and ideally, they would result in identical *I-V* responses. *Levich equation* and *Koutecký–Levich equation* are then applied to these *I-V* data to extract D and k^0, respectively.[23] Besides CV and RDE, it is also useful to study the appropriate electrolyte composition (supporting salt, pH, *etc*.) and solubility of redox couples before using them for RFB measurements.

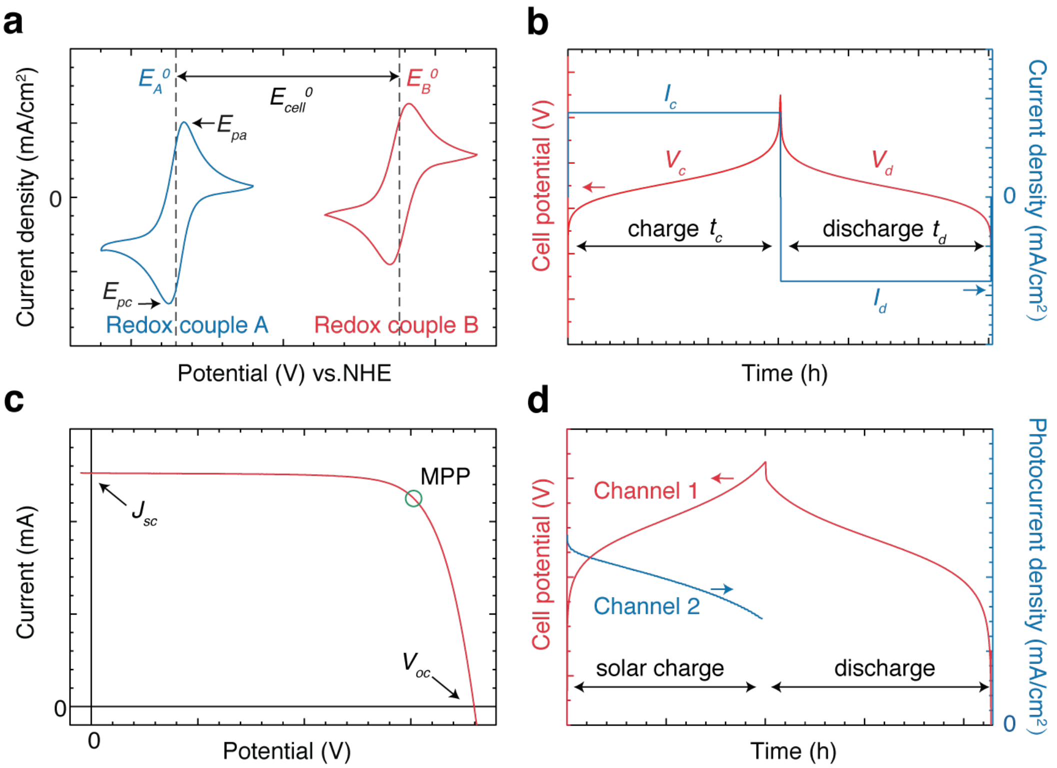

Figure 1.4. Typical characterization methods involved in SFB research. **a**, Cyclic voltammograms for two redox couples A and B. **b**, Galvanostatic cycling profile of RFBs in one cycle, showing both cell voltage and applied current. **c**, *I*-*V* curve of solid-state PV cells (or photoelectrodes measured under solar cell mode). **d**, One cycle of SFB cycling profiles measured with two synchronized potentiostat channels, showing the cell potential recorded by channel 1 and photocurrent density recorded by channel 2.

Because the field of RFB is quickly evolving and many new characterization methods are being developed,[29] here we only introduce the basic techniques closely related to SFB research. To obtained the most relevant RFB data, we use the same SFB device to perform the RFB tests (by replacing the photoelectrode/current collector assemblies with plain graphite current collectors). Ideally, these tests should be carried out in oxygen-free environment to avoid the oxygen induced degradation of redox couples. We usually start with electrochemical impedance spectroscopy (EIS) as a means to measure the high frequency resistance (R_{hf}). EIS is also performed periodically between other tests to assess the overall impedance characteristic of RFBs at different stages. LSVs are then performed to obtain the *I-V* characteristics of RFBs, from which DC resistance (R_{dc}), maximum power and OCV can be calculated.[30] The most important measurements for RFBs is the cycling tests, which are usually performed galvanostatically with appropriate upper and lower voltage cutoffs. From cycling tests we can not only determine the energy density of RFBs but also calculate their Coulombic efficiency (CE = $\frac{\int I_d t_d}{\int I_c t_c}$, where I is current, t is time, and subscription d and c stand for charging and discharging, respectively), voltage efficiency (VE = $\frac{\frac{\int V_d t_d}{\int t_d}}{\frac{\int V_c t_c}{\int t_c}}$, where V is cell potential) and energy efficiency (EE = CE×VE = $\frac{\int P_d t_d}{\int P_c t_c}$, where P is power) (Figure 1.4b).[19] Moreover, cycling tests also reveal the lifetime of RFBs, which is usually determined by chemical stability and membrane permeability of redox couples. It is recommended to evaluate the lifetime of RFBs based on temporal capacity decay rate ($\frac{capacity\ (t_0) - capacity\ (t_1)}{(t_1 - t_0)}$) rather than cycle decay rate, because unlike that of solid-state batteries, the stability of RFBs are believed to be independent of cycle numbers.[29]

Photoelectrodes. As discussed in the previous section, although photoelectrodes based on both simple semiconductors and PV cells each has cons and pros, the state-of-the-art SFB devices reported so far are all built with PV cell based photoelectrodes. Hence, we specifically focus on the characterization of PV cell based photoelectrodes in the discussion below. Before fabrication into photoelectrodes suitable in SFBs, solid-state Ohmic contacts are made to the front and back side of the cells and two-electrode LSVs are measured under either AM 1.5 G illumination or dark condition to characterize their open circuit potential (V_{oc}), short circuit current density (J_{sc}), fill factor (FF), power conversion efficiency (PCE), and maximum power point (MPP) (Figure 1.4c). The PV cells are then fabricated into photoelectrodes to characterize their PEC solar performance with the configuration of either solar cell mode or solar recharge mode. The electrolytes should contain either generally fast redox couples (e.g., ferro/ferricyanide) or specific redox couples that will be used for further SFB characterazations. As mentioned before, the internal junction in these photoelectrodes would generally result in V_{oc} and J_{sc} that are very close to those measured from solid-state PV cells. However, the FF of photoelectrode could greatly decrease if electrochemical kinetics limitation is reached during LSV measurement.[15] We can quantitatively understand such limitation by first examine the *Bulter-Volmer equation* for simple one-electron transfer reaction at solid-liquid interface:

$$i = FAk^0[C_O(0,t)e^{-\alpha f\eta} - C_R(0,t)e^{(1-\alpha)f\eta}] \quad (4)$$

, where A is electrode area, f is F/RT, α is transfer coefficient, η is overpotential, F, k^0, R and T have their usual meanings as in the previous equations.[23,31] There are several ways to increase the maximum kinetics current i at given η, such as increasing the redox couple concentration, or using redox couples that have larger k^0. Based on our experience, the photocurrents generated on the photoelectrode-electrolyte interfaces are usually large enough that mass transfer may also limit the electrochemical kinetics current, which can be improved by increasing electrolyte flow rate.

SFBs. To perform cycling tests of SFBs, two synchronized potentiostat channels are needed. Channel 1 is configured under RFB mode (Figure 1.3a) to monitor the cell potential and channel 2 is configured under solar recharge mode (Figure 1.3b) to monitor the photocurrent. During the solar charging process, channel 1 is set to open circuit to measure cell OCV and channel 2 is set to short circuit to measure photocurrent generated by the photoelectrode under simulated illumination. The charging process can either have a time limit or a cell voltage limit to control the capacity utilization range. However, due to the possible decay of the overall cell capacity and photocurrent, time limit would usually result in undesired shifts in the actual capacity utilization range, especially during long term cycling tests. Hence, setting upper voltage limits in Channel 1 during solar charging processes is preferred. During the discharging process, simulated illumination is blocked by a potentiostat-synchronized beam block, channel 2 is set to galvanostatic discharging mode with a lower potential limit, the same as that used in the discharging of RFBs, and channel 1 is set to open circuit to isolate photoelectrode from this process.

After cycling tests, CE ($\frac{\int I_d t_d}{\int I_c t_c}$) and VE ($\frac{\frac{\int V_d t_d}{\int t_d}}{\frac{\int V_c t_c}{\int t_c}}$) can be calculated based on the same equation as for RFBs (Figure 1.4d). Note that for CE, I_d, t_d are from extracted channel 1, while I_c, t_c are extracted from channel 2; for VE, all the data come from channel 1. For SFBs, CE×VE only gives the energy efficiency of the energy storage part without accounting for the solar energy conversion efficiency, thus a more comprehensive round trip energy efficiency, solar-to-output electricity efficiency (SOEE) need to be introduced:[13]

$$SOEE = \frac{E_{electrical,out}}{E_{illumination}} = \frac{\int I_d V_d dt}{\int SAdt}, \tag{5}$$

where $E_{electrical,out}$ is the output electrical energy, $E_{illumination}$ is the input solar energy, S is the irradiance of simulated solar illumination, A is the active area of photoelectrode.

1.5 Voltage matching and SOEE$_{ins}$

SOEE is undoubtedly the most important figure of merit of SFBs that has attracted most attention in the field. In this section, we describe our mechanistic understanding on SOEE and discuss design principles for improving SOEE of SFBs.

In Figure 1.5a, we plot the *I-V* curve (red curve) of a hypothetical photoelectrode. During the solar charging process of the SFB built with this photoelectrode, the actual operating current should be somewhere on this curve, which is determined by the *I-V* response of the energy storage component (i.e., the RFB component). Assuming an arbitrary E_{cell}^{0}, we can then simulate the *I-V* response of the energy storage component based on equation 2 and a simplified linear *I-V* response:[22]

$$E_{cell} = E_{cell}^{0} - \frac{RT}{nF}\ln\left[\frac{1-SOC}{SOC}\right]^{2} + IR_{dc}. \tag{6}$$

By overlaying I-E_{cell} (blue lines in Figure 1.5a) with *I-V* curve of the photoelectrode, we can find the operating point as the intersection of these two curves (green circles in Figure 1.5a). As suggested by equation 5, the operating point would change with SOC as I-E_{cell} line changes. Such change indicates that the power conversion efficiency of photoelectrodes as well as the SOEE of SFBs should also be influenced by SOC. To quantitatively understand the relationship between SOEE and SOC, we need to examine the power conversion efficiency of the SFB at certain a SOC. We define this as the instantaneous solar-to-output electricity efficiency ($\mathrm{SOEE_{ins}}$) with the following equation:[15]

$$SOEE_{ins} = \frac{P_{electrical,in}}{P_{illumination}} \times PE_{internal} = \frac{I_{operating}V_{operating}}{SA} \times CE \times VE, \tag{7}$$

where $P_{electrical,in}$ is the input electrical power provided by photoelectrode, $P_{illumination}$ is the power of illumination provided by solar simulator, $PE_{internal}$ is the internal (only consider the energy storage part) power conversion efficiency of SFB, $I_{operating}$ and $V_{operating}$ are the photocurrent and cell voltage at operating point.[15] From equation 5 and 6, we not only can simulate the $SOEE_{ins}$-SOC relationship (Figure 1.5b), but also estimate the overall SOEE by calculating the integral average $\mathrm{SOEE_{ins}}$ with respect to SOC. More importantly, the simulation method introduced herein can be used to calculate the overall SOEE with different E^0_{cell}s and offer a qualitative way for identifying the best matched E^0_{cell} for a given photoelectrode to maximize the SOEE (Figure 1.5c).[16] Optimized E^0_{cell} can be achieved by designing proper redox couple pairs for a given photelectrode, which is relatively easy to accomplish using organic or organometallic redox couples due to their great tunability in terms of molecular structures and electrochemical properties (Figure 1.5d). Alternatively, the match between E^0_{cell}s and photoelectrodes can also be optimized by designing proper photoelectrodes with desired *I-V* characteristics. And of course, the most feasible way may lie in the combination of both strategies. In addition to the voltage matching, VE could also influence the $SOEE_{ins}$ as shown in equation 7. From the following equation: $VE = \frac{E^0_{cell}+IR_{DC}}{E^0_{cell}-IR_{DC}}$, we can see that VE increases with E^0_{cell}, and thus a high E^0_{cell} is generally more advantageous than low E^0_{cell}. To match with a high E^0_{cell}, high photovoltage photoelectrodes are desired, which partially explained why SFBs with tandem junction photoelectrodes[16] exhibited much higher SOEE than those with single junction photoelectrodes.[15]

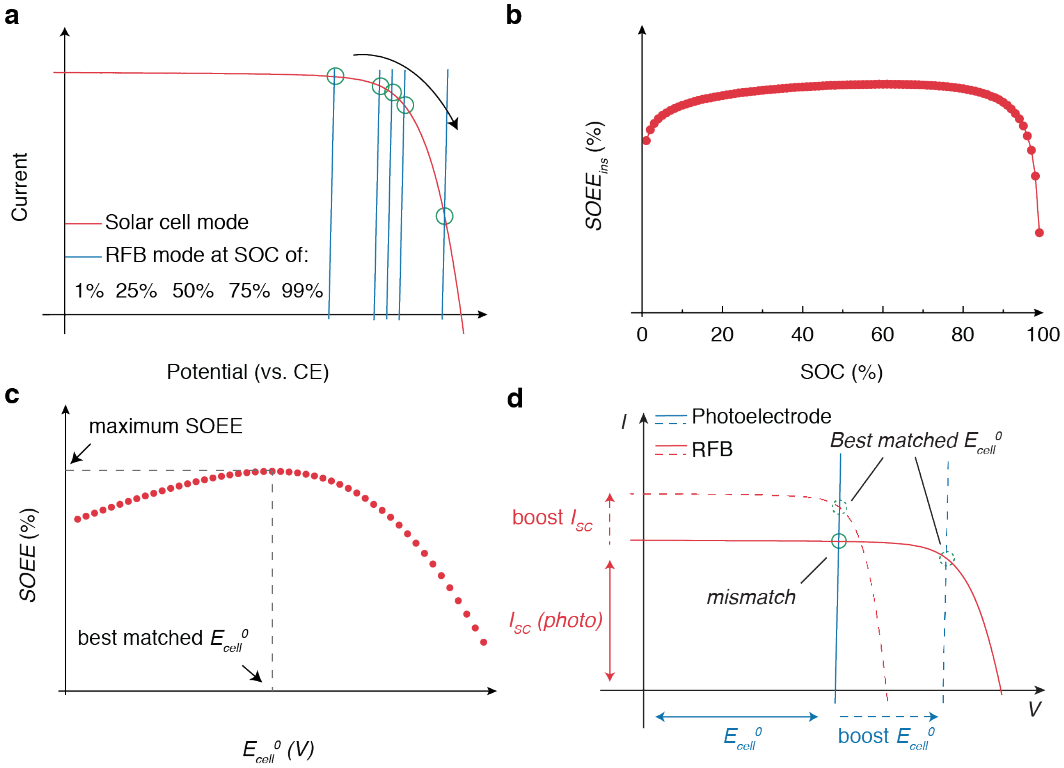

Figure 1.5. Numerical simulation method for finding best matched E_{cell}^0 with hypothetical photoelectrode. a, Overlaid I-V curve of a hypothetical SFB measured under solar cell mode and RFB mode at different SOCs. **b**, Numerically calculated $SOEE_{ins}$ at different SOCs, showing a non-constant behavior of $SOEE_{ins}$ during the solar charging process. **c**, Overall SOEE with respect to E_{cell}^0, from which the best matched E_{cell}^0 can be identified. **d**. Overlaid *I-V* curve of a hypothetical SFB measured under solar cell mode and RFB mode, showing the scenarios of working voltage mismatch (solid curves) and ideal match (dashed curves).

1.6 Important figure of merits besides SOEE

In addition to SOEE, many other figures of merits of SFBs should also be studied and improved in order to enable practical devices for real applications. Here we introduce some key points that we believe deserve particular attention at the early stage of SFB research.

PCE utilization rate is a parameter directly related to SOEE, which is defined as the ratio of SOEE (of SFB) to PCE (of photoelectrodes): $PCE\ utilization\ rate = \frac{SOEE}{PCE}$.[16] This ratio serves as a qualitative measure of the voltage matching between photoelectrodes and redox couples that discussed in the previous section. High PCE utilization rates are desired for SFBs to make sure the solar energy conversion ability of photoelectrodes is not hindered by the voltage matching, and a well designed SFB should generally deliver a PCE utilization rate higher than 80%.[16] However, because of the SOC dependence of $SOEE_{ins}$, it is impossible to achieve 100% PCE utilization rate.

Lifetime is probably the second most important factor to consider other than overall device efficiency for any energy harvest and storage devices, including SFBs. Stable redox couples, low-permeability membranes and robust photoelectrodes are all necessary for long lifetime SFBs. For early SFB demonstrations, especially those with organic redox couples, the poor stability of redox couples and high membrane permeability often limit the lifetime of SFBs.[10,13,32] However, recent years have seen the emerging of much more stable organic redox couples,[18] such as those functionalized with alky ammonium side chains,[33,34] which make the stability issue of redox couples less problematic than the photocorrosion of photoelectrodes. In addition, the design of stable redox couples and robust photoelectrodes are not independent because there are many common grounds between these two components. For example, the composition of electrolytes (such as solvent, supporting salt and pH) can exert strong influence on the stability of both redox couples[35] and photoelectrodes.[36] Because the stability of both the photoelectrodes and redox couples are not sensitive to cycle numbers, "lifetime" is preferred than "cycle life" for quantifying the stability of SFBs. By far, the longest continuous operation lifetime for SFBs is 200 hours,[15] and should be further extended for practical applications. Similar to the design principle for boosting *SOEEs*, a combinational strategy may be more effective to extend the lifetime of SFBs in the future.

Energy density for SFBs resembles that for RFBs introduced earlier, and can be improved by both increasing the concentration of redox couples and enlarging formal cell potentials. Theoretically the energy density of SFBs can be as high as that of RFBs. However, the energy density for existing SFB demonstrations is usually fairly low (<1 WhL^{-1}) because the photocurrents generated by the lab-scale photoelectrodes are too small to charge up high energy density devices in a reasonable amount of time (< 8 h, considering the effective sunshine hours in a typical day).[14] Nonetheless, thanks to the decoupled nature of energy and power components in SFBs, this power/energy mismatch can be avoided by using photoelectrodes with larger geometrical area in the more practical devices in the future.

Capacity utilization rate is the ratio of the effectively utilized capacity to the total capacity of SFBs, which is an often overlooked parameter in the SFB literature. A high capacity utilization rate (>80%) is essential for practical SFBs, otherwise part or much of the redox species in the electrolytes would be wasted. Three main reasons could prevent previous SFB demonstrations from reaching a high capacity utilization rate: 1) the photovoltage generated by photoelectrodes is not high enough to charge the SFB to a high SOC; 2) the photocurrent generated by the photoelectrodes is too small to turn over significant amount of redox couples in a reasonable amount of time; 3) the stability of the photoelectrodes, or redox couples, or devices is not good enough to demonstrate a high capacity utilization rate. Furthermore, because the SOEE$_{ins}$ changes with SOC, the overall SOEE of SFBs could be altered with different SOC utilization range (Figure 1.5b), thus it is important to report the actual SOC utilization range for a fair comparison of SOEE.[15,16]

Cost is the last factor to consider, but a very crucial one when it comes to practical applications. For redox couples, organic molecules have received particularly interests recently because they only contain earth abundant elements and thus advantageous to achieve a low eventual manufacturing cost. [3,18] For photoelectrodes, silicon based photoelectrodes are especially cheap, but the SOEE is rather limited;[15] on the other hand, III-V based photoelectrodes can enable a high SOEE, but have extremely high manufacturing cost.[14] To this end, Si/perovskite tandem junction photoelectrodes has emerged as an eclectic approach to reach a good balance between performance and cost.[16] To better guide the future developments of SFBs, careful modeling and cost estimation are urgently needed to quantify the "cost-effectiveness" of different SFB designs, which have already been studied for some RFB systems.[37] These analogs would also better inform us on how to best achieve the cost benefits for SFBs.

1.7 Summary of recent progress and the state-of-the-art of SFBs

In this section, we briefly review the historical and recent development of SFBs and identify the state-of-the-art demonstrations at each development stages. The SOEE and device lifetime (based on operation time) of key SFB demonstrations are summarized in Figure 1.6.

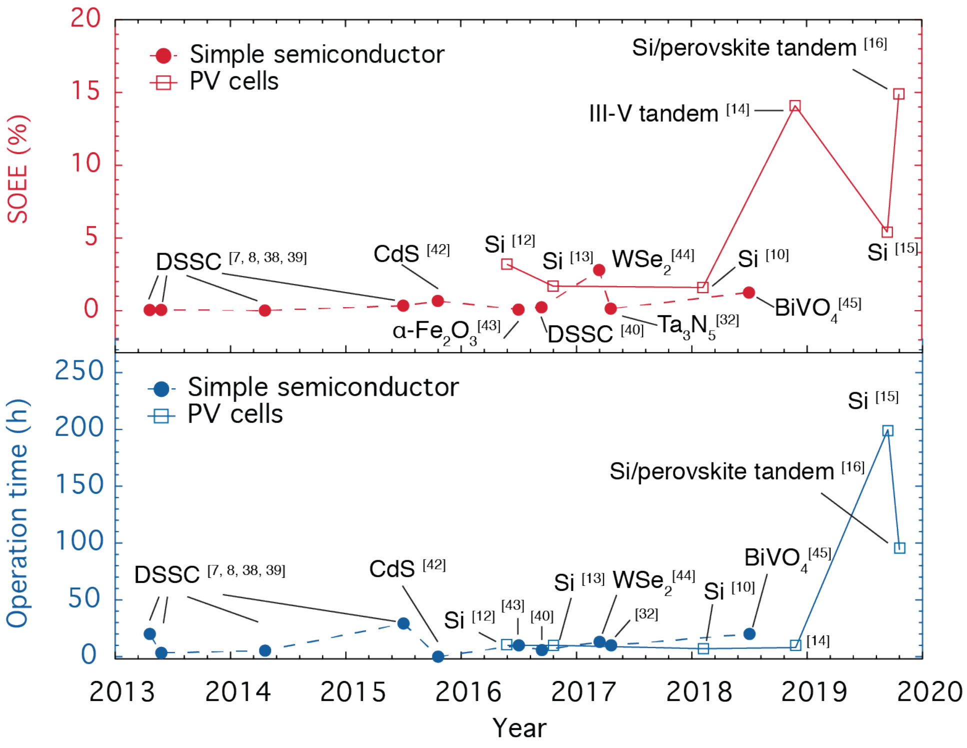

Figure 1.6. Summary of SFBs in terms of SOEE and operation time. **a**, SOEE of SFB built with simple semiconductor photoelectrodes (solid circles) and PV cell photoelectrodes (empty squares). **b**, Continuous operation time reported for SFBs built with simple semiconductor photoelectrodes (solid circles) and PV cell photoelectrodes (empty squares).

SFBs with simple semiconductor photoelectrodes. Due to ease of fabrication, the simple semiconductor photoelectrodes can be found in most of the early SFB demonstrations. For example, because DSSCs can be easily fabricated at low cost, several SFB demonstrations using DSSC photoelectrodes together with I^-/I^{3-} redox couples have been reported (Figure 1.7a).[7,8,38-40] Interestingly, due to the stability requirement of organometallic sensitizing dyes,[41] non-aqueous electrolytes were used to make the liquid junction with DSSC photoelectrodes in most of these SFB demonstrations. However, owing to the intrinsic low solar energy conversion efficiency of these DSSC photoelectrodes and less optimized redox couple choices, these early attempts have nerve been able to reach a SOEE higher than 1%. Other than the TiO_2 that are commonly seen in DSSC photoelectrodes, many other semiconductor materials of various efficiencies including CdS,[42] α-Fe_2O_3,[43] WSe_2,[44] Ta_3N_5[32], $BiVO_4$[45], GaP[46] and InP[46] have also been investigated for SFB applications. Aqueous electrolytes were used in most of the later studies possibly due to the fast emergence of new aqueous redox couples from recent RFB reserach. By far the highest SOEE in this category is 2.8%, which was achieved by the integration of a single-crystal WSe_2 photoelectrode and $AQSH_2/AQS$-I^-/I_3^- redox couples (Figure 1.7b).[44] Other than SOEE, the other important figures of merits are less studied for SFBs in this category, and thus should be incorporated into the future development plans. In addition, many semiconductor materials[47] that have been extensively studied in the early days for PEC liquid junction solar cells can also be interesting to examine for SFBs in the future. Good examples are the family of III-Vs, such as GaAs,[48] and the family of cadmium chalcogenides, such as Cd(Se,Te),[49] due to their suitable and tunable band gaps, strong light absorption and high carrier mobility.

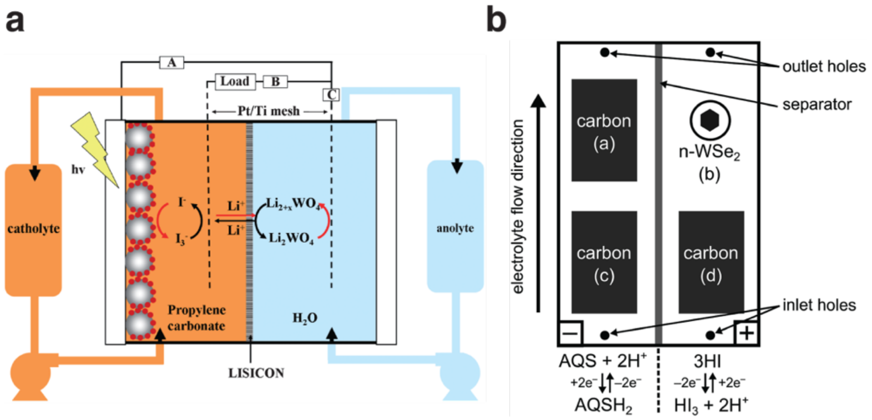

Figure 1.7. Schematic designs of two representative SFBs with simple semiconductor photoelectrodes. **a**, SFB built with TiO_2 DSSC photoelectrodes and I^-/I_3^-- $Li_{2+x}WO_3/Li_2WO_3$ redox couples **b**, SFB built with a single-crystal WSe_2 photoelectrode and $AQSH_2/AQS$-I^-/I_3^- redox couples. Panel **a** reproduced from ref. 8, panel **b** reproduced from ref. 44.

SFBs with PV cell photoelectrodes. Both Li et al.[12] and Wedege et al.[10] have reported prototype SFB devices using silicon PV cell based photoelectrodes, however, with separated PEC charging cell and RFB cell (electrolytes are circulated between two devices) (Figure 1.8a, b). In 2016, we demonstrated the first monolithically integrated SFB with PV cell based photoelectrodes using silicon PV cells and AQDS/BQDS redox couples (Figure 1.8c, d).[13] Our prototype SFB showed an average SOEE of around 1.7% over ten cycles. Although quite impressive among other SFBs reported till that time, 1.7 % was still far lower than the record efficiency for comparable technologies, such as that for PEC water splitting cells (>12%).[50]

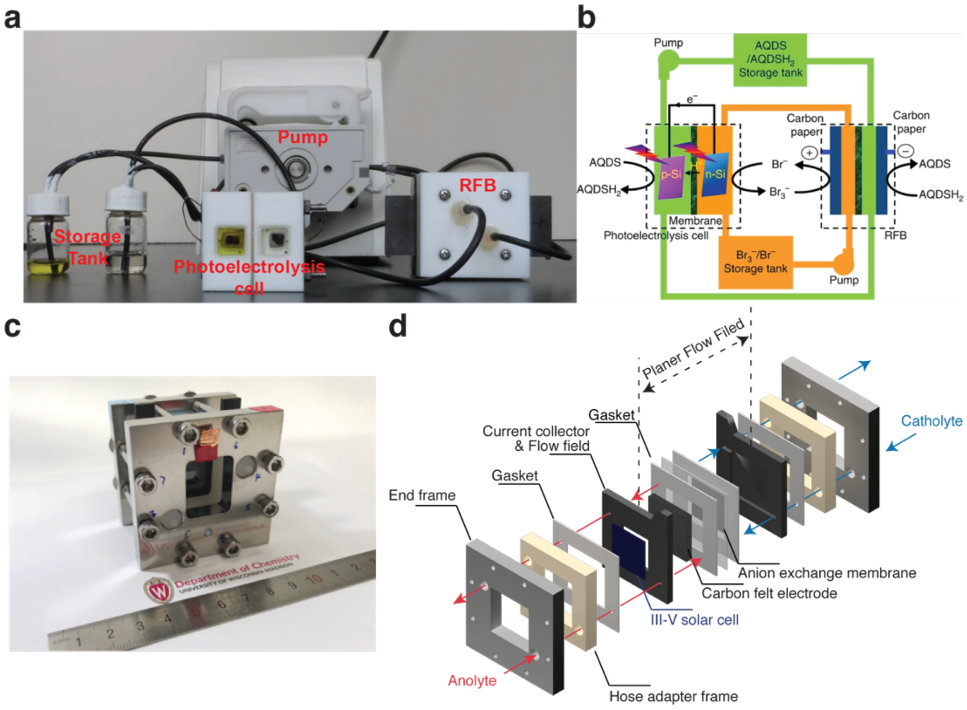

Figure 1.8. Photographs and schematic designs of two different type of SFB devices. **a-b**, A decoupled SFB device with separated PEC charging cell and RFB cell. **c-d**, A monolithically integrated SFB device than can perform all the functions in a single cell. Panel **a** and **b** reproduced from ref. 12, panel **c** and **d** reproduced from ref. 14.

After demonstrating the proof-of-concept SFB device, we carefully studied the working mechanisms and design principles for SFBs and successfully demonstrated a high-performance SFB device using highly efficient and high photovoltage tandem III-V solar cells and high voltage 4-OH-TEMPO/MV redox couples. Enabled by highly efficient photoelectrodes, properly matched redox couples, and carefully designed flow field design, a record SOEE of 14.1% has been achieved for the SFB (Figure 1.9a).[14] With the rational design principles developed in this study, we were also able to further optimize our proof-of-concept SFB device with the same Si photoelectrode design and better voltage matched BTMAP-Vi/Fc redox couples. The efforts have not only boosted the SOEE from 1.7% to 5.4%, but also produced the longest continuous cycling time for SFBs of 200 hours with low corrosiveness neutral electrolytes and well-protected silicon photelectrodes (Figure 1.9b).[15] These demonstrations have push the boundaries along various dimensions for SFBs, but at the cost of significant drawbacks in other dimensions, such as the imbalance between high SOEE and long life time. To combine all the merits of the pervious demonstrations, we redesigned all the critical components of SFBs with a revised design principle based on aforementioned numerical modeling, and developed properly matched perovskite/Si tandem junction photoelectrodes and BTMAP-Vi/N^{Me}-TEMPO redox couples (Figure 1.9c).[16] These advances enabled the state-of-the-art SFB demonstration with highest SOEE and PCE utilization rate, longest continuous cycling time, near unity capacity utilization rate and uncompromised low cost (Figure 1.9d).

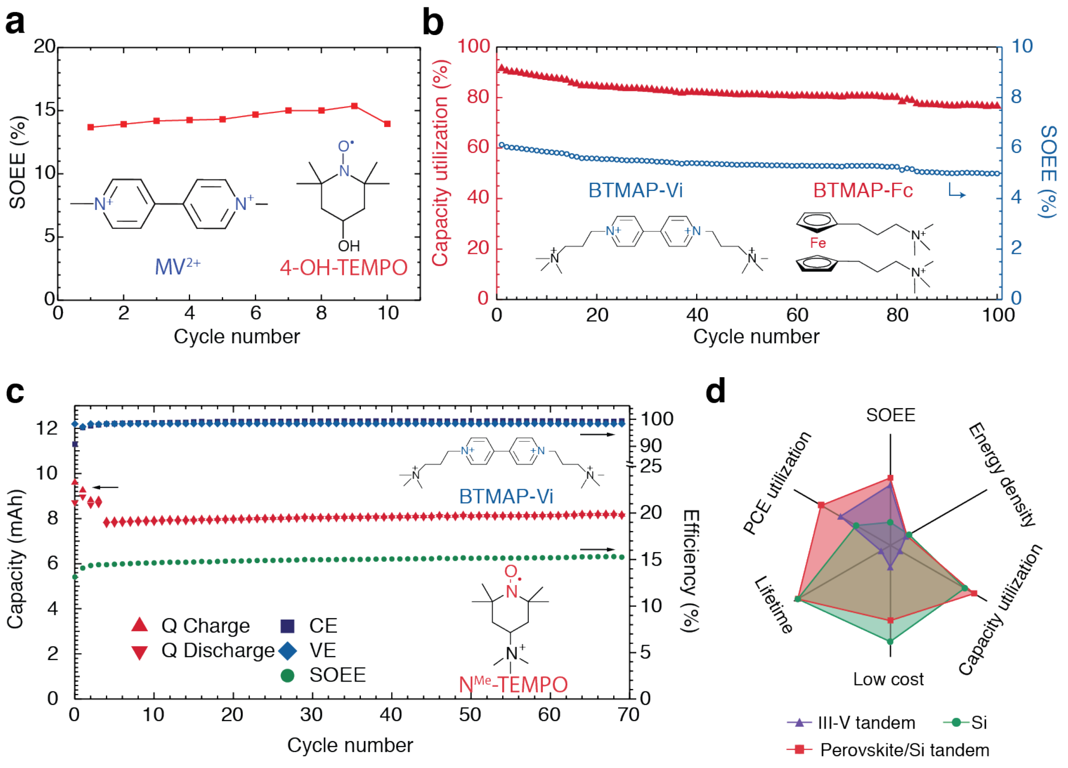

Figure 1.9. Cycling profile and performance comparison of 3 state-of-the-art SFB demonstrations. **a,** SFB built with III-V tandem junction photoelectrode and $MVCl_2$/4-OH-TEMPO redox couples. **b,** SFB built with two single junction silicon photoelectrodes and BTMAP-Vi/Fc redox couples. **c**, SFB built with perovskite/silicon photoelectrode and BTMAP-Vi/N^{Me}-TEMPO redox couples. **d**, Comparison of the three SFB demonstrations in a multivariate radar chart. Panel **a** reproduced from ref. 14, Panel **b** reproduced from ref. 15, panel **c** and **d** reproduced from ref. 16.

1.8 Conclusion and outlook

Even though SFB is a relatively young approach for energy conversation and storage, it has seen rapid growth in the last few years. The working mechanisms, design principles and device demonstrations presented herein have laid a solid foundation for future developments of SFBs, which should include both fundamental understandings and technical advancements. In particular, most of the redox couples and photoelectrode materials used for SFBs were directly adopted from previous studies in RFBs,[18] PEC cells[47] and PVs.[51] To further improve the performance and reduce cost of SFBs, it is necessary to design novel materials specifically suitable for SFBs. For example, is it possible to design materials that can serve as both photoelectrodes and redox couples? Will there be materials that can enable membrane-less SFBs? These challenges entail fundamental material innovations that are currently absent in the field.

The design principles developed so far are mainly based on the macroscopic understandings of energy transfer processes in SFBs. SFBs are multicomponent device that involves electron transfer through many interfaces. It is crucial to have clear microscopic mechanistic understandings of each electron transfer steps before they can be rationally improved. For example, the electron transfer at the photoelectrode/liquid junction is a rarely studied but undoubtedly important process.[52] Although such process may seem to be similar to that in PEC fuel generating cells,[53] the vastly different photoelectrode surfaces (often without catalysts), greatly varied redox couples and their constantly changing concentrations may result in electron transfer mechanisms not previously reported. We anticipate that such fundamental study can lead to valuable insights into the further improving of the fill factors of photoelectrodes.[15]

Because SFBs lie in an interdisciplinary field between PEC cells and RFBs, the design of SFBs have been greatly influenced by the previous studies in these two fields. The state-of-the-art SFB devices feature a “zero-gap” device design that is directly modified from the most commonly used device design for RFBs.[54] Certainly, this device design has provided a convenient platform for early stage research of SFBs. However, it is unknown whether this device structure can make the most of the SFB concept when scaled-up. For practical applications, RFB cells contain multiple stacks in one cell to boost the power capability.[19] But it is challenging to incorporate such multi-stack design into the current SFB device framework. On the other hand, the unique integration in SFBs may also bring additional functional benefits over the PV plus battery approach. For example, the liquid electrolytes in SFBs can act as coolant for photoelectrodes,[55] which is a necessary component for concentrated PV systems,[56] but comes for "free" in SFBs. The development of SFBs should aim to enable a complementary rather than competing approach with existing solar energy utilization technologies. Aside from technological advancements, the identification of niche applications specifically for SFBs is important to enhance the practical implantation of SFBs. For example, the monolithically integrated nature of SFBs is especially advantageous for stand-alone off-grid electrification applications in rural areas.

1.9 References

1. Lewis, N. S. Research opportunities to advance solar energy utilization. *Science* **351**, aad1920 (2016).

2. Rugolo, J. & Aziz, M. J. Electricity storage for intermittent renewable sources. *Energy Environ. Sci.* **5**, 7151-7160 (2012).

3. Wedege, K., Bae, D., Smith, W. A., Mendes, A. & Bentien, A. Solar Redox Flow Batteries with Organic Redox Couples in Aqueous Electrolytes: A Minireview. *J. Phys. Chem. C* **122**, 25729-25740 (2018).

4. Hodes, G., Manassen, J. & Cahen, D. Photoelectrochemical energy conversion and storage using polycrystalline chalcogenide electrodes. *Nature* **261**, 403-404 (1976).

5. Gurung, A. & Qiao, Q. Q. Solar Charging Batteries: Advances, Challenges, and Opportunities. *Joule* **2**, 1217-1230 (2018).

6. Luo, B., Ye, D. & Wang, L. Recent Progress on Integrated Energy Conversion and Storage Systems. *Adv. Sci.* **488**, 1700104-1700115 (2017).

7. Liu, P., Cao, Y. l., Li, G. R., Gao, X. P., Ai, X. P. & Yang, H. X. A Solar Rechargeable Flow Battery Based on Photoregeneration of Two Soluble Redox Couples. *Chemsuschem* **6**, 802-806 (2013).

8. Yan, N. F., Li, G. R. & Gao, X. P. Solar rechargeable redox flow battery based on Li2WO4/LiI couples in dual-phase electrolytes. *J. Mater. Chem. A* **1**, 7012-7014 (2013).

9. Yu, Z. S., Leilaeioun, M. & Holman, Z. Selecting tandem partners for silicon solar cells. *Nat. Energy* **1**, 16137 (2016).

10. Wedege, K., Bae, D., Dražević, E., Mendes, A., Vesborg, P. C. K. & Bentien, A. Unbiased, complete solar charging of a neutral flow battery by a single Si photocathode. *RSC Adv.* **8**, 6331-6340 (2018).

11. Cao, L. Y., Skyllas-Kazacos, M. & Wang, D. W. Solar Redox Flow Batteries: Mechanism, Design, and Measurement. *Adv. Sustain. Syst.* **2** (2018).

12. Liao, S., Zong, X., Seger, B., Pedersen, T., Yao, T., Ding, C., Shi, J., Chen, J. & Li, C. Integrating a dual-silicon photoelectrochemical cell into a redox flow battery for unassisted photocharging. *Nat. Commun.* **7**, 11474-11478 (2016).

13. Li, W., Fu, H.-C., Li, L., Caban-Acevedo, M., He, J.-H. & Jin, S. Integrated photoelectrochemical solar energy conversion and organic redox flow battery devices. *Angew. Chem. Int. Ed.* **55**, 13104-13108 (2016).

14. Li, W., Fu, H.-C., Zhao, Y., He, J.-H. & Jin, S. 14.1% Efficient Monolithically Integrated Solar Flow Battery. *Chem* **4**, 2644-2657 (2018).

15. Li, W., Kerr, E., Goulet, M.-A., Fu, H.-C., Zhao, Y., Yang, Y., Veyssal, A., He, J.-H., Gordon, R. G., Aziz, M. J. & Jin, S. A Long Lifetime Aqueous Organic Solar Flow Battery. *Adv. Energy. Mater.* **9**, 1900918 (2019).

16. Li, W., Zheng, J., Hu, B., Fu, H.-C., Zhao, Y., He, J.-H., Liu, T. L., Ho-Baillie, A. & Jin, S. Perovskite/Si Tandem Solar Cell Powered High Performance Solar Flow Battery. *Chapter 5* (2019).

17. Park, M., Ryu, J., Wang, W. & Cho, J. Material design and engineering of next-generation flow-battery technologies. *Nat. Rev. Mater.* **2**, 16080-16018 (2016).

18. Wei, X. L., Pan, W. X., Duan, W. T., Hollas, A., Yang, Z., Li, B., Nie, Z. M., Liu, J., Reed, D., Wang, W. & Sprenkle, V. Materials and Systems for Organic Redox Flow Batteries: Status and Challenges. *ACS Energy Lett.* **2**, 2187-2204 (2017).

19. Weber, A. Z., Mench, M. M., Meyers, J. P., Ross, P. N., Gostick, J. T. & Liu, Q. Redox flow batteries: A review. *J. Appl. Electrochem.* **41**, 1137-1164 (2011).

20. Soloveichik, G. L. Flow Batteries: Current Status and Trends. *Chem. Rev.* **115**, 11533-11558 (2015).

21. Kamat, P. V., Tvrdy, K., Baker, D. R. & Radich, J. G. Beyond Photovoltaics: Semiconductor Nanoarchitectures for Liquid-Junction Solar Cells. *Chem. Rev.* **110**, 6664-6688 (2010).

22. You, D. J., Zhang, H. M. & Chen, J. A simple model for the vanadium redox battery. *Electrochim. Acta* **54**, 6827-6836 (2009).

23. Bard, A. J. & Faulkner, L. R. *Electrochemical Methods: Fundamentals and Applications, 2nd Edition*. (Wiley, 2000).

24. Nielander, A. C., Shaner, M. R., Papadantonakis, K. M., Francis, S. A. & Lewis, N. S. A taxonomy for solar fuels generators. *Energy Environ. Sci.* **8**, 16-25 (2014).

25. Walter, M. G., Warren, E. L., McKone, J. R., Boettcher, S. W., Mi, Q., Santori, E. A. & Lewis, N. S. Solar water splitting cells. *Chem. Rev.* **110**, 6446-6473 (2010).

26. Jin, S. What Else Can Photoelectrochemical Solar Energy Conversion Do Besides Water Splitting and CO2 Reduction? *ACS Energy Lett.* **3**, 2610-2612 (2018).

27. Nozik, A. J. Photoelectrochemistry - Applications to Solar-Energy Conversion. *Annu. Rev. Phys. Chem.* **29**, 189-222 (1978).

28. Ardo, S. *et al.* Pathways to electrochemical solar-hydrogen technologies. *Energy Environ. Sci.* **11**, 2768-2783 (2018).

29. Goulet, M. A. & Aziz, M. J. Flow Battery Molecular Reactant Stability Determined by Symmetric Cell Cycling Methods. *J. Electrochem. Soc.* **165**, A1466-A1477 (2018).

30. Huskinson, B., Marshak, M. P., Suh, C., Er, S., Gerhardt, M. R., Galvin, C. J., Chen, X., Aspuru-Guzik, A., Gordon, R. G. & Aziz, M. J. A metal-free organic-inorganic aqueous flow battery. *Nature* **505**, 195-198 (2014).

31. Tan, M. X., Laibinis, P. E., Nguyen, S. T., Kesselman, J. M., Stanton, C. E. & Lewis, N. S. Principles and Applications of Semiconductor Photoelectrochemistry. *Prog. Inorg. Chem.* **41**, 21-144 (1994).

32. Cheng, Q., Fan, W., He, Y., Ma, P., Vanka, S., Fan, S., Mi, Z. & Wang, D. Photorechargeable high voltage redox battery enabled by Ta_3N_5 and GaN/Si dual-photoelectrode. *Adv. Mater.* **351**, 1700312-1700318 (2017).

33. Beh, E. S., De Porcellinis, D., Gracia, R. L., Xia, K. T., Gordon, R. G. & Aziz, M. J. A Neutral pH Aqueous Organic-Organometallic Redox Flow Battery with Extremely High Capacity Retention. *ACS Energy Lett.* **2**, 639-644 (2017).

34. Hu, B., DeBruler, C., Rhodes, Z. & Liu, T. L. Long-Cycling Aqueous Organic Redox Flow Battery (AORFB) toward Sustainable and Safe Energy Storage. *J. Am. Chem. Soc.* **139**, 1207-1214 (2017).

35. Luo, J., Sam, A., Hu, B., DeBruler, C., Wei, X. L., Wang, W. & Liu, T. L. Unraveling pH dependent cycling stability of ferricyanide/ferrocyanide in redox flow batteries. *Nano Energy* **42**, 215-221 (2017).

36. Bae, D., Seger, B., Vesborg, P. C. K., Hansen, O. & Chorkendorff, I. Strategies for stable water splitting via protected photoelectrodes. *Chem. Soc. Rev.* **46**, 1933-1954 (2017).

37. Darling, R. M., Gallagher, K. G., Kowalski, J. A., Ha, S. & Brushett, F. R. Pathways to low-cost electrochemical energy storage: a comparison of aqueous and nonaqueous flow batteries. *Energy Environ. Sci.* **7**, 3459-3477 (2014).

38. Yan, N. F., Li, G. R. & Gao, X. P. Electroactive Organic Compounds as Anode-Active Materials for Solar Rechargeable Redox Flow Battery in Dual-Phase Electrolytes. *J. Electrochem. Soc.* **161**, A736-A741 (2014).

39. Yu, M. Z., McCulloch, W. D., Beauchamp, D. R., Huang, Z. J., Ren, X. D. & Wu, Y. Y. Aqueous Lithium-Iodine Solar Flow Battery for the Simultaneous Conversion and Storage of Solar Energy. *J. Am. Chem. Soc.* **137**, 8332-8335 (2015).

40. McCulloch, W. D., Yu, M. Z. & Wu, Y. Y. pH-Tuning a Solar Redox Flow Battery for Integrated Energy Conversion and Storage. *ACS Energy Lett.* **1**, 578-582 (2016).

41. Wu, J., Lan, Z., Lin, J., Huang, M., Huang, Y., Fan, L. & Luo, G. Electrolytes in Dye-Sensitized Solar Cells. *Chem. Rev.* **115**, 2136-2173 (2015).

42. Azevedo, J., Seipp, T., Burfeind, J., Sousa, C., Bentien, A., Araújo, J. P. & Mendes, A. Unbiased solar energy storage: Photoelectrochemical redox flow battery. *Nano Energy* **22**, 396-405 (2016).

43. Wedege, K., Azevedo, J., Khataee, A., Bentien, A. & Mendes, A. Direct solar charging of an organic-inorganic, stable, and aqueous alkaline redox flow battery with a hematite photoanode. *Angew. Chem. Int. Ed.* **55**, 7142-7147 (2016).

44. McKone, J. R., DiSalvo, F. J. & Abruna, H. D. Solar energy conversion, storage, and release using an integrated solar-driven redox flow battery. *J. Mater. Chem. A* **5**, 5362-5372 (2017).

45. Zhou, Y., Zhang, S., Ding, Y., Zhang, L., Zhang, C., Zhang, X., Zhao, Y. & Yu, G. Efficient Solar Energy Harvesting and Storage through a Robust Photocatalyst Driving Reversible Redox Reactions. *Adv. Mater.* **103**, 1802294-1802297 (2018).

46. Durant, B. K., She, Y., Wang, P., Kraus, T. & Parkinson, B. A. Solar Charged Redox Flow Battery: A Tandem Photoelectrochemical Approach. *J. Electrochem. Soc.* **166**, H3001-H3008 (2018).

47. Sivula, K. & van de Krol, R. Semiconducting materials for photoelectrochemical energy conversion. *Nat. Rev. Mater.* **1**, 15010 (2016).

48. Chang, K., Heller, A., Schwartz, B., Menezes, S. & Miller, B. Stable semiconductor liquid junction cell with 9 percent solar-to-electrical conversion efficiency. *Science* **196**, 1097-1099 (1977).

49. Levy-Clement, C., Triboulet, R., Rioux, J., Etcheberry, A., Licht, S. & Tenne, R. Ternary Cd (Se, Te) alloy semiconductors: Synthesis, material characterization, and high - efficiency photoelectrochemical cells. *J. Appl. Phys.* **58**, 4703-4708 (1985).

50. Khaselev, O. & Turner, J. A. A monolithic photovoltaic-photoelectrochemical device for hydrogen production via water splitting. *Science* **280**, 425-427 (1998).

51. Green, M. A., Hishikawa, Y., Dunlop, E. D., Levi, D. H., Hohl-Ebinger, J., Yoshita, M. & Ho-Baillie, A. W. Y. Solar cell efficiency tables (Version 53). *Progress in Photovoltaics: Research and Applications* **27**, 3-12 (2019).

52. Lewis, N. S. Mechanistic studies of light-induced charge separation at semiconductor/liquid interfaces. *Accounts. Chem. Res.* **23**, 176-183 (1990).

53. Nellist, M. R., Laskowski, F. A. L., Lin, F. D., Mills, T. J. & Boettcher, S. W. Semiconductor-Electrocatalyst Interfaces: Theory, Experiment, and Applications in Photoelectrochemical Water Splitting. *Accounts. Chem. Res.* **49**, 733-740 (2016).

54. Aaron, D. S., Liu, Q., Tang, Z., Grim, G. M., Papandrew, A. B., Turhan, A., Zawodzinski, T. A. & Mench, M. M. Dramatic performance gains in vanadium redox flow batteries through modified cell architecture. *J. Power Sources* **206**, 450-453 (2012).

55. Tembhurne, S., Nandjou, F. & Haussener, S. A thermally synergistic photo-electrochemical hydrogen generator operating under concentrated solar irradiation. *Nat. Energy* **4**, 399-407 (2019).

56. Royne, A., Dey, C. J. & Mills, D. R. Cooling of photovoltaic cells under concentrated illumination: a critical review. *Sol. Energy Mater. Sol. Cells* **86**, 451-483 (2005).

CHAPTER 2

Integrated Photoelectrochemical Solar Energy Conversion and Organic Redox Flow Battery Devices*

2.1 Abstract

The practical utilization of solar energy demands not only efficient energy conversion but also inexpensive large scale energy storage. Building on mature regenerative photoelectrochemical solar cells and emerging electrochemical redox flow batteries (RFBs), more efficient, scalable, compact and cost-effective hybrid energy conversion and storage devices could be realized. Here we present a novel integrated photoelectrochemical solar energy conversion and electrochemical storage device by integrating regenerative silicon solar cells and 9,10-anthraquinone-2,7-disulfonic acid (AQDS)/1,2-benzoquinone-3,5-disulfonic acid (BQDS) RFBs. The integrated device can be directly charged by solar light without external bias, and discharged like normal RFBs with an energy storage density of 1.15 Wh/L and a solar-to-output electricity efficiency (SOEE) of 1.7% over many cycles. The concept demonstrated here exploits a previously undeveloped design connecting two major energy technologies and promises a general approach for storing solar energy electrochemically with high theoretical storage capacity and efficiency.

---

* This chapter was originally published in *Angew. Chem. Int. Ed.* **55**, 13104-13108 (2016), in collaboration with Fu, H.-C., Li, L., Caban-Acevedo, M., He, J.-H. and Jin, S.

2.2 Introduction

Renewable energy technologies generally rely on harvesting energy from our most readily exploitable and only truly limitless source: the Sun. With the development over several decades, photovoltaic (PV) solar cells convert solar energy to electricity with increasing efficiency and decreasing cost.[1] However, the intermittent nature of sunlight necessitates the storage of the photo-generated electricity, therefore further large-scale deployment of solar cells also depends on scalable and inexpensive grid-level energy storage solutions.[2] These would demand new grid-level electrochemical energy storage solutions, such as RFBs.[3,4] The use of liquid electrolytes in RFBs allows convenient and low-cost scale up of the energy storage capacity without larger cells, such as the case for Li-ion batteries; instead, scaling up the energy capacity only entails increasing the amount of redox active species in storage tanks without scaling up the power generation components. Another potential solution would be to directly store solar energy in the chemical bonds of molecular fuels (such as hydrogen gas or hydrocarbons)[5-7] that could be stored, transported, combusted, or ultimately consumed on demand using a fuel cell device to generate electricity. Despite the intense studies since the 1970s,[8] photoelectrochemical (PEC) solar fuel devices have not become commercially viable so far, which is at least partially due to the kinetic barriers (i.e. large overpotentials) for generating chemical fuels from photoexcited carriers at semiconductor-liquid interface, e.g. hydrogen evolution reaction (HER)[9-11] and oxygen evolution reaction (OER)[12,13] for the case of PEC water splitting, that limit the efficiency of such devices.[5] In contrast, many other redox reactions have facile kinetics (small overpotentials) on the surface of common semiconductors and inert electrodes, which facilitates the collection of the photo-generated carriers from semiconductors and leads to efficient "regenerative" PEC solar cells.[14,15]

Moreover, the liquid electrolytes containing redox couples utilized in regenerative PEC solar cells are also exactly what are needed for energy storage in RFBs.[3,4] In RFBs, the electrons (or holes) can be stored in redox couples in aqueous (or non-aqueous) solutions as chemical energy. Specifically, the recently demonstrated RFBs with quinone-based redox couples[16,17] are particularly attractive for coupling with PEC devices. In these RFBs, both catholyte and anolyte are aqueous electrolytes that contain non-metal organic redox species, thus reducing the material cost ($30-40/kWh) compared with the more developed vanadium RFBs ($81/kWh).[16,17] These RFBs can also have a relatively high energy density exceeding 50 Wh/L, due to the high aqueous solubility (> 1 M) of functionalized quinones. Moreover, quinone-based redox couples such as AQDS and BQDS undergo rapid and reversible electron transfer on many electrodes (such as carbon) without any special catalysts.[17] The fast kinetics of these redox couples is a significant advantage over the OER and HER processes in PEC water splitting because it can enable unassisted solar-driven charging with less overpotential penalty as well as higher charge (and discharge) power densities.

We note that there have been preliminary efforts[18] to combine solar energy conversion devices. However, when TiO_2 liquid junction solar cells[19] and dye-sensitized solar cells[20] were integrated with RFBs,[21,22] due to the intrinsic efficiency limits of these solar energy conversion devices, these devices suffered from low photocharging current densities (<1.5 mA/cm^2) and low overall efficiencies.[18] Even though using separated charging/discharging flow chambers instead of an integrated device design is an slight improvement from simply connecting a solar PV device with a RFB,[23] the more complicated device design, higher cost, and low discharge capacity would limit its potential for practical applications. We argue that fully integrating highly efficient regenerative solar cells, such as those based on Si and other mature semiconductors,[1,24] with appropriately potential-matched redox couples that can be used in RFBs in one PEC device will be a more effective strategy. Here we report an integrated PEC solar energy conversion and electrochemical storage device by integrating silicon solar cells in aqueous electrolytes with RFBs using the same pair of organic quinone based redox couples. We demonstrated that such an integrated PEC-RFB device can be charged under solar illumination without external electric bias and discharged at a current density of 10 mA/cm^2 with a maximum output voltage of 0.41 V and a discharge capacity of 3.5 Ah/L over many cycles. This integrated device can utilize solar energy efficiently -- an overall direct solar-to-output electricity efficiency (SOEE) of 1.7% have been achieved without significant performance optimization.

2.3 Results and Discussion

2.3.1 Integrated PEC-RFB device design

As illustrated in Figure 2.1a, our general integrated device design consists of four electrodes, namely a photocathode and a photoanode (that can be made of Si semiconductor), a cathode and an anode made of carbon felt. Quinone-based organic redox couple AQDS is used as the catholyte and BQDS as the anolyte (Figure 2.1b) for both the RFB and PEC cells. In such an integrated PEC-RFB device, solar energy is absorbed by semiconductor electrodes and photoexcited carriers are collected at the semiconductor-liquid electrolyte interface and used to convert the redox couples in the RFB to fully charge up the battery (reduce AQDS to $AQDSH_2$ and oxidize $BQDSH_2$ to BQDS). When electricity is needed, the charged up redox couples will be discharged on the surface of carbon felt electrodes as one would do in the discharge of a RFB to generate the electricity. The electrodes are connected differently in energy delivery and storage mode: the cathode and anode are connected with an external load to discharge the RFB, while the photocathode and photoanode are connected to allow solar-driven unassisted battery recharge. The formal potentials (E^0) for AQDS and BQDS redox couples are 0.21 V and 0.89 V, respectively (Figure 2.1b), therefore the photovoltage generated at the Si photoelectrode- liquid junctions is high enough (about 0.55V + 0.55 V)[9] to drive the battery charge process so that no external electric voltage or energy is needed. A potentiostat will be connected between the photocathode and photoanode to monitor the charging current during our test but not needed for actual device cycling operation. Two electrolyte reservoirs are used to store the catholyte and anolyte, which are constantly pumped through the flow cell.

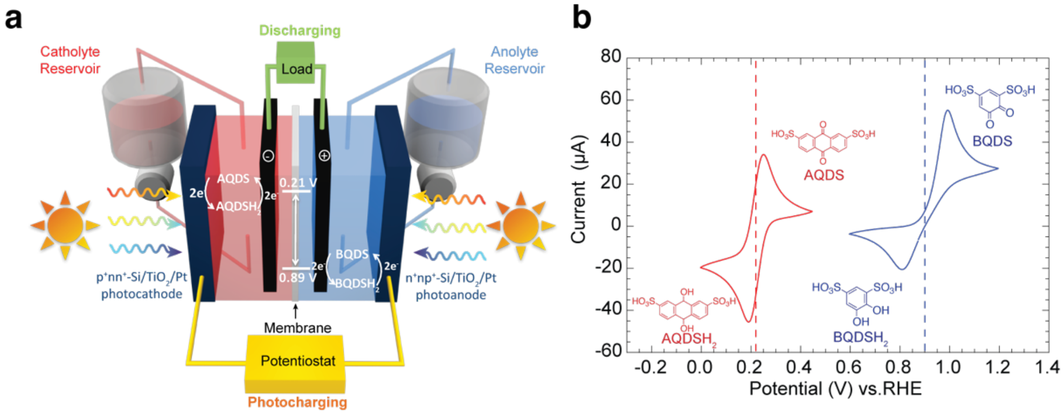

Figure 2.1. Scheme of the integrated PEC-RFB device and characterization of redox couples. a, Scheme of integrated PEC-RFB device using AQDS/BQDS redox couples in catholyte/anolyte. **b**, Cyclic voltammogram of 5 mM AQDS (red curve) and 5 mM BQDS (blue curve) in 1 M H_2SO_4 scanned at 10 mV/s on a glassy carbon electrode.

2.3.2 Performance of AQDS/BQDS RFB

To demonstrate this integrated PEC-RFB device, we first developed and studied the individual components. The RFB was built using aqueous solutions of 0.1 M AQDS and 0.1 M $BQDSH_2$ as catholyte and anolyte, respectively, 1 M sulfuric acid as supporting electrolyte, a Nafion 212 membrane and 2 carbon felt electrodes (Figure A1.1); similar to a recently reported organic RFB.[17] Figure 2.2a shows the representative cycling curves, using voltage cut-offs of 0 V and 1.0 V, at a constant charging/discharging current of 10 mA/cm^2. The RFB had a very stable and reproducible cycling performance with a current efficiency around 96%. Polarization curves and open-circuit potentials (V_{oc}) of the RFB at various states of charge (SOCs) are shown in Figure 2.2b. The V_{oc} increased from 0.39 V to 0.55 V as the SOC increased from 10% to 90%, which provides an easy way to monitor the battery's SOC. Considering the possible overpotential caused by diffusion limits and ohmic resistance, this V_{oc} is specifically suitable for being charged by two Si photoelectrodes connected in series, which have a total theoretical voltage of about 1.1 V.[1] We also note that, as shown in previous reports,[25,26] the chemistry of $BQDSH_2$ is complex and the first charging cycle involved an "activation reaction" of $BQDSH_2$. Consequently, all the $BQDSH_2$ we used in RFB and PEC characterization was pre-activated in a Teflon H-cell by constant-potential electrolysis.

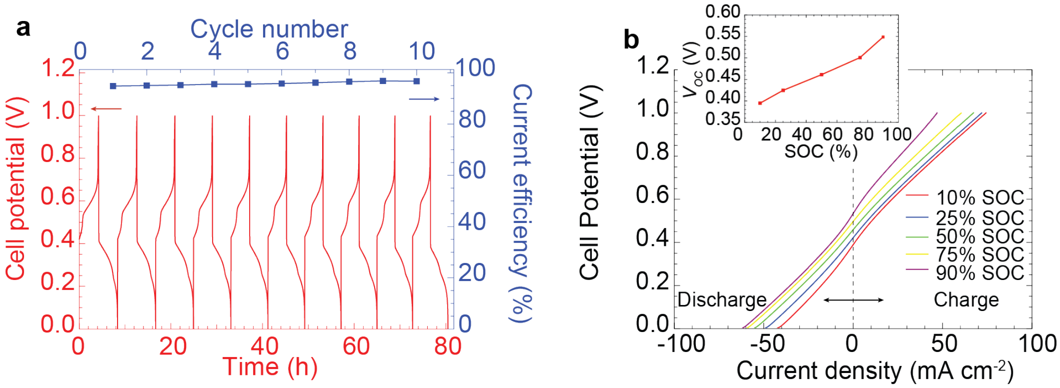

Figure 2.2. Representative RFB device performance. a, Cell cycling behavior at 10 mA/cm^2 using 0.1 M AQDS+1 M H_2SO_4 as catholyte and 0.1 M $BQDSH_2$ + 1 M H_2SO_4 as anolyte. **b**, cell potential versus current density at six different SOCs; inset shows the cell open circuit potential at different SOCs.

2.3.3 Photoelectrochemical characterization of silicon photoelectrodes

We then designed silicon photocathodes and photoanodes as regenerative photoelectrodes in AQDS and $BQDSH_2$ aqueous electrolytes, respectively. Because of the dark color of the concentrated AQDS/BQDS solutions, we designed the photoelectrodes to be illuminated from the back side: a p^+nn^+ Si solar cell (called type A) was used as photocathode (Figure 2.3a) and a n^+np^+ Si solar cell (type B) was used as photoanode (Figure 2.3c). A key here is to protect silicon from the formation of insulating silicon oxides on the surface, yet preserve the fast kinetics of AQDS and BQDS redox couples. A Ti/TiO_2 (5/40 nm) protection layer was deposited using sputter coating and atomic layer deposition (ALD) on the electrolyte side of the photoelectrodes, followed by a 5 nm layer of sputter coated Pt to facilitate the charge transfers at the photoelectrode-liquid interface (Figure 2.3a-c). It is well known that AQDS and BQDS have fast kinetics on glassy carbon,[17] therefore the Pt layer here was only used for minimizing the charge extraction barrier on the surface of Si, but not a specific catalyst for the AQDS reduction or $BQDSH_2$ oxidation reactions.[27,28] Other inexpensive but stable metals such as tungsten and molybdenum, also have the potential to reduce the charge extraction barrier and enable similar PEC performance for these redox reactions (Figure A1.2).

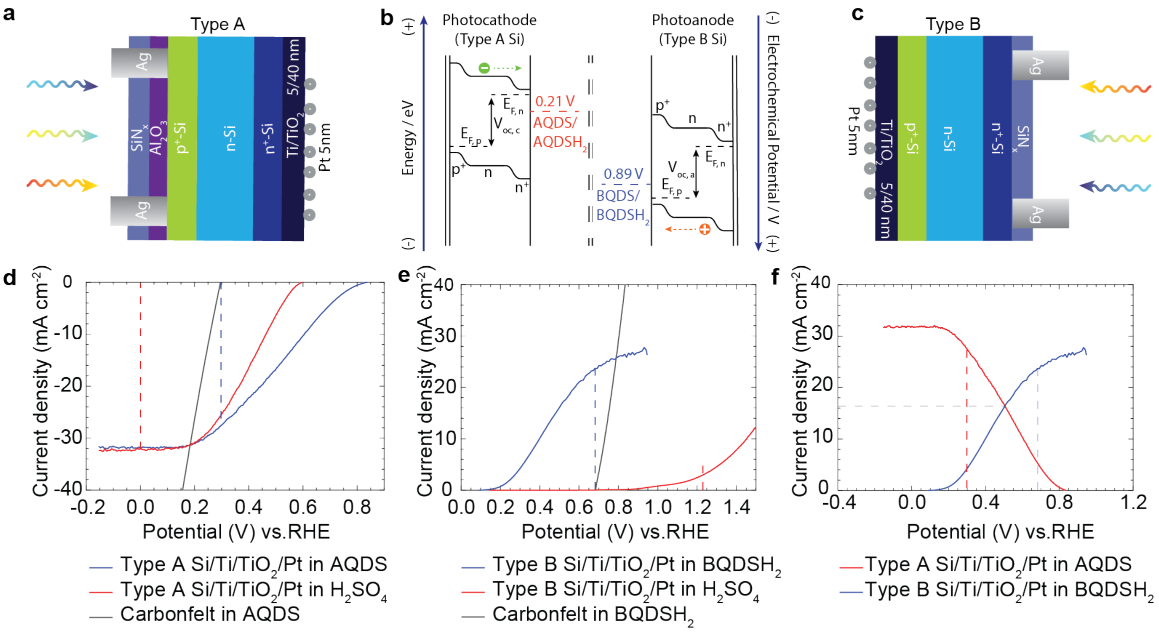

Figure 2.3. Energy diagram and solar performance of silicon photoelectrodes. a, Cross-section schematic of type A p^+nn^+-Si/Ti/TiO_2/Pt photocathode. **b**, band diagram for the photocharging process. **c**, cross-section schematic of type B n^+np^+-Si/Ti/TiO_2/Pt photoanode. **d-e**, J-V data for **d** type A p^+nn^+-Si/Ti/TiO_2/Pt electrode measured in 0.1 M AQDS solution or 1 M H_2SO_4 solution; **e** type B n^+np^+-Si/Ti/TiO_2/Pt electrode measured in 0.1 M $BQDSH_2$ solution or 1 M H_2SO_4 solution. **f**, Overlaid J-V data for type A p^+nn^+-Si/Ti/TiO_2/Pt electrode measured in 0.1 M AQDS solution with type B n^+np^+-Si/Ti/TiO_2/Pt electrode measured in 0.1 M $BQDSH_2$ solution, the intersection shows the maximum power point.

We first evaluated the PEC responses of these Ti/TiO_2/Pt coated Si photoelectrodes in 0.1 M AQDS, 0.1 M $BQDSH_2$ as well as in 1 M H_2SO_4 using a three-electrode configuration under simulated 1 Sun (100 mW/cm^2) solar illumination. To determine the equilibrium potential (E_{eq}) of AQDS reduction and $BQDSH_2$ oxidation reaction, linear sweep voltammetry (LSV) scans first were carried out using a 2 cm^2 carbon felt as the working electrode, thus E_{on} as well as the short circuit current density (J_{sc}) of the device can be determined based on E_{eq}. Due to the existence of the buried *pn* junction in the Si cells, the E_{on} maintained the same value (0.55 V) for the type A cell in both AQDS solution and H_2SO_4 solution (Figure 2.3d);[29] while for the type B cell in $BQDSH_2$ solution, the apparent E_{on} was a little lower (Figure 2.3e), perhaps due to the relatively slower diffusion and kinetics of $BQDSH_2$. The overlaid current density-potential scans (Figure 2.3f) predict a theoretical maximum operating current density of 16.4 mA/cm^2 for the integrated PEC-RFB device out of a J_{sc} of 27.4 mA/cm^2 for photocathode and a J_{sc} of 23.7 mA/cm^2 for photoanode. The operating current density is mainly limited by the poor fill factors (*FF*) of the two current PEC cells, especially the type B cell, which may be attributed to the limited surface area of the photoelectrodes and the lower diffusion rate of organic redox couples.

2.3.4 Integrated PEC-RFB device characterization

In light of the excellent and reproducible performance of the RFB as well as the reasonable performance from the regenerative PEC cell components, we built the integrated PEC-RFB devices. To characterize the charging-discharging performance, two potentiostats were used: potentiostat 1 was connected between two photoelectrodes to monitor the photocurrent (blue curve in Figure 2.4a); potentiostat 2 was connected between two carbon felt electrodes to monitor the potential difference between the two electrodes (red curve in Figure 2.4a). During photocharging, the photoelectrodes were illuminated with an EKE-type illuminator at 1 Sun and no external bias was provided. The V_{oc} of the flow battery increased with time owing to the increasing SOC. At the same time, the photocurrent decreased slightly because when higher potential was needed to charge the battery, lower current could be drawn from the solar cells. During the discharging process, the illumination was turned off and the integrated device was discharged as a normal RFB at a rate of -10 mA/cm^2 until the cell potential reached 0 V. By integrating the charging/discharging current with respect to time, the charge injected to and drawn from the integrated device as well as the current efficiency can be calculated. The integrated device had a very stable and reproducible cycling performance over ten cycles with a current efficiency around 91% (Figure 2.4b), which means most of the photoexcited charges can be stored in the aqueous AQDS/BQDS redox couples and redrawn from the integrated device without significant loss caused by side reactions such as HER and OER. Long-term charging/discharging test reveals that the integrated device can be photocharged without external bias to about 80% SOC in 7.3 hours and discharged with a capacity of 3.5 Ah/L (Figure A1.3).

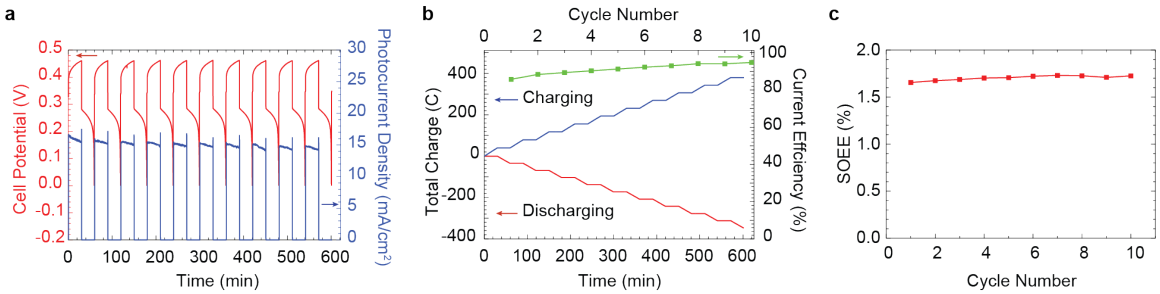

Figure 2.4. The operation and performance of the integrated PEC-RFB device. a, cell cycling behavior with no bias potential during charging process and a current density of -10 mA/cm^2 during discharging process. **b**, total charge and current efficiency of the cell. **c**, cell SOEE at different cycles.

In order to quantitatively evaluate the efficiency of the integrated PEC-RFB device, here we propose a new Figure.of merit for this type of integrated solar-RFB devices: solar-to-output electricity efficiency (SOEE), which is defined by the ratio of the usable electrical energy delivered by the integrated device ($E_{\text{discharging}}$) over the total solar energy input ($E_{\text{illumination}}$). The SOEE can be calculated using equation 1:

$$SOEE\ (\%) = \frac{E_{discharging}}{E_{illumination}} = \frac{\int I_{out}V_{out}dt}{\int SAdt} \tag{1}$$

where I_{out} is the output (discharging) current, V_{out} is the output voltage, S is the total incident solar irradiance, and A is the *total* illumination areas of photoanode and photocathode. A typical integrated device showed an average SOEE of around 1.7% over ten cycles (Figure 2.4c).

The slight photocurrent density decay shown in Figure 2.4a can be attributed to the photocorrosion of the Si photoelectrodes, which was confirmed by two-electrode PEC measurements of the photoelectrodes before and after cycling test (Figure A1.4). The long term stability of the Si photoelectrodes can be further improved by optimizing the protection layer such as increasing the TiO_2 layer thickness and post growth annealing.[27,30] One of the limitations on the SOEE of the current integrated device is the poor *FF* of the photoelectrodes, which could be significantly improved by incorporating redox couples that have higher diffusion rates and even faster kinetics, or optimizing the electrolyte flow,[3] or increasing the surface area of the photoelectrodes by introducing nanostructures on the surface.

Because there have been significant technological developments in regenerative PEC solar cells[24] and RFBs,[4] we are building on two reasonably mature or rapidly maturing technologies to make a previously unexploited connection to develop a new technology that have a clear pathway for improvement. Fundamentally, the working potential of the integrated device can be further enlarged by replacing redox couples that have higher E^0 in anolyte as well as those with lower E^0 in catholyte, to fully utilize the voltage window of aqueous solution (1.23 V or even higher when considering the overpotentials for HER and OER) and increase device energy density. For example, the recently reported RFB based on 2,6-dihydroxyanthraquinone (2,6-DHAQ) and ferri-ferrocyanide redox couples has a V_{oc} of 1.2 V[31] and is promising for the integrated devices, especially since ferri-ferrocyanide is a very fast redox couple commonly used in PEC cells. Improving the open circuit voltage and the conversion efficiency of regenerative solar cells would further increase the theoretical maximum energy storage density. The single junction crystalline silicon photoelectrodes could be replaced by photoelectrodes that have higher open circuit voltage and higher efficiency, such as GaAs,[32] triple junction amorphous Si,[33] and even potentially high-performance perovskite solar cell.[34,35] Especially if the formal potentials of the redox couples can be matched well with the band positions of the photocathode and photoanode to create tandem dual-photoelectrode devices similar to tandem dual-photoelectrode PEC water splitting devices,[9] those high voltage photoelectrodes can be even more effectively utilized to drive bias-free charging of the RFBs with higher working voltage, such as the 2,6-DHAQ-ferricyanide RFBs mentioned above, to significantly enhance the energy density. The initial integrated device we demonstrated herein has a promising energy storage density of 1.15 Wh/L at present, but potentially the energy density can reach up to 50 Wh/L[16,31] and the SOEE can also be significantly increased based on the various improvements discussed above.

2.4 Conclusions

In conclusion, we demonstrated a fully integrated photoelectrochemical solar energy conversion and electrochemical storage device by integrating regenerative Si solar cells and all organic AQDS-BQDS RFBs. The use of aqueous electrolytes and non-metal redox couples minimized the prototype device design and fabrication difficulties, thus making the device intrinsically safe, scalable, and cost-effective. The integrated device can be directly charged by solar light without external bias, and discharged like normal RFBs to generate electricity when needed. A promising solar-to-output electricity efficiency of 1.7% and energy storage density of 1.15 Wh/L have been achieved with the initially demonstrated device without significant optimization, which can be further improved by optimization of devices and operating parameters. Significant enhancement of SOEE and energy storage density can be realized when more suitable redox couples and semiconductors can be designed and paired. This work opens up a new and promising direction for integrating the efficient harvesting and conversion of renewable solar energy and the scalable electrochemical energy storage into a single device, especially for standalone integrated energy systems, allowing for more scalable, efficient, and cost-effective round trip solar energy utilization.

2.5 Methods

2.5.1 RFB and integrated PEC-RFB device

The RFB measurements were carried out in a custom-made device (Figure A1.1). Two flow channel blocks were machined out of solid polycarbonate each with a 17.4 mm × 20 mm × 17.4 mm flow channel and a 0.25 inch clearance hole on top for inserting graphite rod current collector. Graphitized carbon felt electrodes with an area of 2 cm^2 (AvCarb G100, 3.2 mm uncompressed) was used as received and connected with the graphite rod current collector on both side of the cell. Nafion NRE-212 (Sigma Aldrich) was used as the membrane between two channels. The membrane was pretreated by soaking in 1 M sulfuric acid solution for 30 minutes followed by soaking in hydrogen peroxide solution for 30 minutes and finally soaking in deionized water for 30 minutes at 80 ^{o}C. The flow channel blocks were held together in the final assembled device by bolts. A solution of 0.1 M of 9,10-anthraquinone-2,7-disulfonate (AQDS) disodium salt (TCI America) in 1 M H_2SO_4 was used as the catholyte. A solution of 0.1 M 1,2-dihydroxybenzene-3,5-disulfonic acid (BQDS) disodium salt monohydrate (Alfa Aesar) in 1 M H_2SO_4, which had been pre-activated by a constant potential oxidation at 1 V vs. saturated calomel electrode (SCE) followed by a constant potential reduction at 0 V vs. SCE, was used as the anolyte in the fully discharged state. The electrolytes were pumped via Viton tubing through the flow channels at a rate of 20 mL/min by a peristaltic pump (Cole-Parmer Masterflex L/S).

2.5.2 RFB measurements

The RFB cycling and polarization performance tests were performed using a Bio-Logic SP-200 potentiostat. The RFB cycling tests were performed by charging and discharging the battery at a constant current density of 10 mA/cm^2 with 0 V and 1.0 V as bottom and top potential limits, respectively. We note that, although $BQDSH_2$ shows a simple quasi-reversible electrochemical behavior during the short time scale of cyclic voltammetry scans (Figure 2.1b), the chemistry of $BQDSH_2$ is more complex during the RFB cycling test. We observed two plateaus in the RFB cycling curve (Figure 2.2a), which may be attributed to the slow structure change of $BQDSH_2$ during the RFB cycling test. In the cell polarization characterization, the battery was step charged to different state of charges (SOCs) and a linear sweep voltammetry (LSV) scan was performed at the end of each charging step at a scan rate of 10 mV/s.

2.5.3 Fabrication of p^+nn^+ (type A) and n^+np^+ (type B) silicon cells coated with different thin film passivation layers

The fabrication of type A and type B silicon photoelectrodes started with 300 µm n-type (100) Si as substrates (dopant concentration of 5×10^{15} cm^{-3}). 300 nm of p$^+$ emitter layer (dopant concentration of 9×10^{19} cm^{-3}) was formed by the thermal diffusion of BCl_3. 300 nm of n$^+$ back surface field layer (dopant concentration of 3×10^{20} cm^{-3}) was fabricated by the thermal diffusion of $POCl_4$. Surface texturing was performed on both sides of the substrates to minimize reflection for enhancing light scattering and light harvesting. From our design, the light-harvesting side was textured by random pyramids along the diffusion surfaces. The groove was textured along the diffusion faces on the solution contact side. In addition, 70 nm of SiN_x was deposited by PECVD as an antireflection (AR) layer on the surface of light-harvesting side. In addition, a 7 nm passivation layer of Al_2O_3 was grown by a thermal ALD process in an Oxford Instruments OpALTM reactor with $[Al(CH_3)_3]$ precursor at 200 °C on the light harvesting side of type A cell to improve the photocarrier recombination and top internal reflection. The cycle times were ~7 s and the growth-per-cycle was 1.0 Å. The cycles were repeated until the target film thickness was reached.

A thin (5 nm) layer of titanium was first sputter coated and followed by a 40 nm thick layer of TiO_2 thin film deposited by atomic layer deposition (ALD) using tetrakis(dimethylamino) titanium (TDMAT) and O_2-plasma precursors at 150 ºC in ~200 mTorr Ar environment on the surface of both type A and type B silicon photoelectrodes that will contact electrolytes. On top of that, another layer of 5 nm thick platinum thin film was sputter deposited to minimize the charge extraction barrier. Alternatively, a 40 nm thick layer of molybdenum or tungsten thin film was sputter coated on the electrolyte contact side of type A silicon photocathodes as comparison protection layer. All of the sputter coatings were carried out using dc magnetron sputtering method with a power of 400W.

2.5.4 Fabrication of silicon photoelectrodes

The ohmic contact to Si photoelectrodes was made by attaching a copper foil onto the back side of the Si photoelectrodes (p^+ side of the type A Si cell, n^+ side of the type B Si cell) with Ga/In eutectic mixture (Sigma Aldrich) and fixed with silver paint (Ted Pella, PELCO colloidal silver). The remaining area of the back side was covered by a thin cover glass (Fisher) and sealed by epoxy resin (Hysol 9460). After curing, the copper foil was carefully folded and encased in a 2 mm diameter glass tube for PEC characterization. The Si photoelectrodes for the integrated PEC-RFB device characterization were fabricated following similar procedures, except that the Si photoelectrodes were affixed onto a custom-made polycarbonate face plate by epoxy resin to integrate with the RFB flow channel blocks at both ends (see photo in Figure A1.1). The geometric area of the exposed Si electrodes was determined by calibrated digital images and Photoshop.

2.5.5 Photoelectrochemical characterization

The PEC characteristics were measured in a three-electrode configuration using a Bio-Logic SP-200 potentiostat under 1 Sun (100 mW/cm^2) of AM 1.5 G simulated sunlight illumination using a Newport Model 91191 solar simulator, as well as EKE-type tungsten-halogen lamps made by USHIO. EKE is the ANSI (American National Standards Institute) code for the halogen light bulb, which defines that the light bulb has a MR-16D shape and operates at 21V, 7.14 A with a color temperature of 3250 K. A Si photodiode (Thorlabs) was used to calibrate the illumination intensity of the AM 1.5G solar simulator to 100 mW/cm^2. Then to calibrate the EKE-type solar simulator, the short-circuit current of a solid-state type A silicon solar cell was first measured under 1 Sun of AM1.5 G simulated solar light, then the EKE-type solar simulator was calibrated to generate the same short-circuit current using the same solid-state type A Si solar cell. The PEC measurements were performed in 0.1 M AQDS solution for type A Si photoelectrodes and in 0.1 M pre-activated BQDSH$_2$ solution for type B Si photoelectrodes. 1 M H_2SO_4 was used as supporting electrolytes as well as a comparison for all PEC measurements. A Pt wire electrode (CHI instruments) and a SCE electrode (CHI instrument) were used as the counter and reference electrode, respectively. To determine the equilibrium potential (E_{eq}) of AQDS reduction reaction and BQDSH$_2$ oxidation reaction, LSV scans were carried out using a 2 cm^2 carbon felt as the working electrode before the PEC measurement. All LSV curves were measured at a scan rate of 10 mV/s without correcting for any uncompensated resistance losses.

2.5.6 Integrated PEC-RFB device characterization

To characterize the charging-discharging behaviors of the integrated PEC-RFB devices, two Bio-Logic SP-200 potentiostats were used: potentiostat 1 was connected between two photoelectrodes to monitor the photocurrent; potentiostat 2 was connected between two carbon felt electrodes to monitor the potential difference between the two electrodes. During the photocharging process, photoelectrodes were illuminated by EKE-type simulated solar illumination (provided by a Fiber-Lite MI-150 illuminator with 2 goose neck fiber-optics to split illumination into two beams, Figure A1.5) at 1 Sun without applying any external bias by the potentiostats. The illumination intensity of these two output beams was also calibrated using a Si photodiode (Thorlabs). During the discharging process, the simulated solar illumination was turned off and the integrated device was operated as a normal RFB with a -10 mA/cm^2 discharging current density applied by potentiostat 2 until the cell potential reached 0 V.

The PEC characteristics of the photoelectrodes used in the integrated devices were examined before and after integrated device cycling test in a two-electrode configuration under 1 Sun of EKE-type simulated sunlight illumination (Figure A1.4). The same electrolyte used in the integrated device test was used in the PEC characterization. LSV scans were carried out with a 2 cm^2 carbon felt as the counter electrode.

2.6 References

1. Green, M. A., Emery, K., Hishikawa, Y., Warta, W. & Dunlop, E. D. Solar cell efficiency tables (version 47). *Progress in Photovoltaics: Research and Applications* **24**, 3-11 (2015).

2. Lewis, N. S. Research opportunities to advance solar energy utilization. *Science* **351**, aad1920 (2016).

3. Weber, A. Z. *et al.* Redox flow batteries: a review. *J. Appl. Electrochem.* **41**, 1137-1164 (2011).

4. Soloveichik, G. L. Flow Batteries: Current Status and Trends. *Chem. Rev.* **115**, 11533-11558 (2015).

5. Walter, M. G. *et al.* Solar Water Splitting Cells. *Chem. Rev.* **110**, 6446-6473 (2010).

6. Lewis, N. S. & Nocera, D. G. Powering the planet: Chemical challenges in solar energy utilization. *Proc. Natl. Acad. Sci. U.S.A.* **103**, 15729-15735 (2006).

7. Nocera, D. G. The Artificial Leaf. *Acc. Chem. Res.* **45**, 767-776 (2012).

8. Honda, K. & Fujishima, A. Photolysis-decomposition of water at the surface of an irradiated semiconductor. *Nature* **238**, 37-38 (1972).

9. Cabán-Acevedo, M. *et al.* Efficient hydrogen evolution catalysis using ternary pyrite-type cobalt phosphosulphide. *Nat. Mater.* **14**, 1245-1251 (2015).

10. Zeng, M. & Li, Y. Recent advances in heterogeneous electrocatalysts for the hydrogen evolution reaction. *J. Mater. Chem. A* **3**, 14942-14962 (2015).

11. Faber, M. S. & Jin, S. Earth-abundant inorganic electrocatalysts and their nanostructures for energy conversion applications. *Energy Environ. Sci.* **7**, 3519-3542 (2014).

12. McCrory, C. C. L., Jung, S., Peters, J. C. & Jaramillo, T. F. Benchmarking Heterogeneous Electrocatalysts for the Oxygen Evolution Reaction. *J. Am. Chem. Soc.* **135**, 16977-16987 (2013).

13. Huynh, M., Bediako, D. K. & Nocera, D. G. A functionally stable manganese oxide oxygen evolution catalyst in acid. *J. Am. Chem. Soc.* **136**, 6002-6010 (2014).

14. Luttmer, J. D., Konrad, D. & Trachtenberg, I. Electrode Materials for Hydrobromic Acid Electrolysis in Texas-Instruments Solar Chemical Converter. *J. Electrochem. Soc.* **132**, 1054-1058 (1985).

15. Heller, A. 11.5% solar conversion efficiency in the photocathodically protected p-InP/V3+-V2+-HCI/C semiconductor liquid junction cell. *Appl. Phys. Lett.* **38**, 282-284 (1981).

16. Huskinson, B. *et al.* A metal-free organic–inorganic aqueous flow battery. *Nature* **505**, 195-198 (2014).

17. Yang, B., Hoober-Burkhardt, L., Wang, F., Surya Prakash, G. K. & Narayanan, S. R. An Inexpensive Aqueous Flow Battery for Large-Scale Electrical Energy Storage Based on Water-Soluble Organic Redox Couples. *J. Electrochem. Soc.* **161**, A1371-A1380 (2014).

18. Yu, M. *et al.* Solar-powered electrochemical energy storage: an alternative to solar fuels. *J. Mater. Chem. A* **4**, 2766-2782 (2016).

19. Wei, Z., Liu, D., Hsu, C. & Liu, F. All-vanadium redox photoelectrochemical cell: An approach to store solar energy. *Electrochem. Commun.* **45**, 79-82 (2014).

20. Yu, M. *et al.* Aqueous Lithium–Iodine Solar Flow Battery for the Simultaneous Conversion and Storage of Solar Energy. *J. Am. Chem. Soc.* **137**, 8332-8335 (2015).

21. Azevedo, J. *et al.* Unbiased solar energy storage: Photoelectrochemical redox flow battery. *Nano Energy* **22**, 396-405 (2016).

22. Yan, N. F., Li, G. R. & Gao, X. P. Solar rechargeable redox flow battery based on Li2WO4/LiI couples in dual-phase electrolytes. *J. Mater. Chem. A* **1**, 7012-7014 (2013).

23. Liao, S. *et al.* Integrating a dual-silicon photoelectrochemical cell into a redox flow battery for unassisted photocharging. *Nat. Commun.* **7**, 11474-11478 (2016).

24. Kamat, P. V., Tvrdy, K., Baker, D. R. & Radich, J. G. Beyond Photovoltaics: Semiconductor Nanoarchitectures for Liquid-Junction Solar Cells. *Chem. Rev.* **110**, 6664-6688 (2010).

25. Xu, Y., Wen, Y.-H., Cheng, J., Cao, G.-P. & Yang, Y.-S. A study of tiron in aqueous solutions for redox flow battery application. *Electrochim. Acta* **55**, 715-720 (2010).

26. Yang, B. *et al.* High-Performance Aqueous Organic Flow Battery with Quinone-Based Redox Couples at Both Electrodes. *J. Electrochem. Soc.* **163**, A1442-A1449 (2016).

27. Mei, B. *et al.* Crystalline TiO 2: A Generic and Effective Electron-Conducting Protection Layer for Photoanodes and -cathodes. *The Journal of Physical Chemistry C* **119**, 15019-15027 (2015).

28. Scheuermann, A. G. *et al.* Design principles for maximizing photovoltage in metal-oxide-protected water-splitting photoanodes. *Nat. Mater.* **15**, 99-105 (2016).

29. Bard, A. J., Bocarsly, A. B., Fan, F. R. F., Walton, E. G. & Wrighton, M. S. The concept of Fermi level pinning at semiconductor/liquid junctions. Consequences for energy conversion efficiency and selection of useful solution redox couples in solar devices. *J. Am. Chem. Soc.* **102**, 3671-3677 (1980).

30. Seger, B. *et al.* Using TiO2 as a conductive protective layer for photocathodic H2 evolution. *J. Am. Chem. Soc.* **135**, 1057-1064 (2013).

31. Lin, K. *et al.* Alkaline quinone flow battery. *Science* **349**, 1529-1532 (2015).

32. Kayes, B. M. *et al.* 27.6% Conversion efficiency, a new record for single-junction solar cells under 1 sun illumination. *2011 37th IEEE Photovoltaic Specialists Conference (PVSC)*, 4-8 (2011).

33. Reece, S. Y. *et al.* Wireless solar water splitting using silicon-based semiconductors and earth-abundant catalysts. *Science* **334**, 645-648 (2011).

34. Yang, W. S. *et al.* High-performance photovoltaic perovskite layers fabricated through intramolecular exchange. *Science* **348**, 1234-1237 (2015).

35. Hsu, H.-Y. *et al.* A Liquid Junction Photoelectrochemical Solar Cells Based on p-Type $MeNH_3PbI_3$ Perovskite with 1.05 V Open-Circuit Photovoltage. *J. Am. Chem. Soc.* **137**, 14758–14764 (2015).

CHAPTER 3

14.1%-Efficient Monolithically Integrated Solar Flow Battery[*]

3.1 Abstract

Challenges posed by the intermittency of solar energy source necessitate the integration of solar energy conversion with scalable energy storage systems. The monolithic integration of photoelectrochemical solar energy conversion and electrochemical energy storage offers an efficient and compact approach toward practical solar energy utilization. Here we present the design principles for and the demonstration of a highly efficient integrated solar flow battery (SFB) device with a record solar-to-output electricity efficiency (*SOEE*) of 14.1%. Such SFB devices can be configured to perform all the requisite functions from solar energy harvest to electricity redelivery without external bias. Capitalizing on high efficiency and high photovoltage tandem III-V photoelectrodes that are properly matched with high cell voltage redox flow batteries (RFBs), and carefully designed flow field architecture, we reveal the general design principles for efficient SFBs. These results will enable a highly efficient approach for practical off-gird solar utilization and electrification.

---

[*] This chapter was originally published in *Chem* **4**, 2644-2657 (2018), in collaboration with Fu, H.-C., Zhao, Y., He, J.-H. and Jin, S.

3.2 Introduction

The practical utilization of solar energy demands not only efficient energy conversion but also inexpensive large-scale energy storage to accommodate the intermittency of sunlight.[1] Natural photosynthesis shows a promising approach to efficiently utilize solar energy by converting and storing solar energy in chemical bonds. Studies since the 1970s[2] have shown that artificial photosynthesis can also be accomplished using semiconductors in direct contact with liquid electrolytes to perform photoelectrolysis.[3,4] While much research efforts have focused on storing solar energy in molecular fuels by irreversible photoelectrochemical (PEC) reactions, such as PEC water splitting[3,4] and carbon dioxide reduction reaction,[5] the great versatility of semiconductor-based photoelectrolysis also permits reversible redox couples to be used as solar energy storage medias.[6,7] Moreover, reversible electrochemical reactions are also exactly what happens during the energy storage process in rechargeable batteries.[8] In this way, the PEC solar energy conversion process can be seamlessly connected with rechargeable batteries by the common reversible redox reactions they share to realize an integrated device that can be directly charged by solar light, and discharged like normal batteries when needed.

The concept of "solar rechargeable battery" was perhaps first demonstrated in 1976 with polycrystalline CdSe photoelectrode and silver-silver sulfide solid battery electrode.[9] Since then, various approaches toward integrated solar energy conversion and storage have been developed.[10-12] For examples, common rechargeable batteries such as lithium ion batteries,[13] batteries based on other inorganic chemistry[14,15] as well as redox flow batteries (RFBs)[16-21] can be integrated with different types of solar cells. Among them, the integration of PEC cells with RFBs is particular attractive due to the wide selections of redox couples[22-25] and ease of scaling up the energy storage capacity in RFBs.[26-28] Recently, by integrating silicon solar cells and all organic quinone-based

RFBs, the proof-of-concept for a bias-free solar energy conversion and electrochemical storage was demonstrated in a solar flow battery (SFB).[29] However, despite the much higher solar conversion efficiency of the silicon solar cells employed, this prototype device could only achieve a modest solar-to-output electricity efficiency (*SOEE*) of 1.7%, which is not sufficient for practical applications.

This and other examples make it clear that simply integrating high performance solar cells and RFBs does not necessarily guarantee a SFB with a high *SOEE*. With comprehensive mechanism study and deeper understanding of the operation principles of SFBs, we now propose a set of design principles for highly efficient integrated SFB devices. Generally, the photoelectrode used for solar energy conversion devices can be categorized into two types, semiconductor-liquid junction cells[30-32] and photovoltaic (PV) cells.[33] For semiconductor-liquid junction cells, energy level matching between semiconductors and redox species is critical as it determines the photovoltage of such cells.[21] On the other hand, the photovoltage of PV cells is generated by their internal solid-state junctions, thus insensitive to the redox potential of the specific redox couple used. By utilizing PV cells, the difficulties in the overall device design and voltage matching can be greatly reduced, which makes it a good choice for the purpose of proof-of-principle demonstration. Here we present a novel, high efficiency, monolithically integrated SFB device with a record average *SOEE* of 14.1 %, and demonstrate that solar energy harvest, conversion, storage and redelivery can be completed by such a single integrated device without any external electrical energy input. This highly efficient SFB is enabled by high photovoltage and highly efficient III-V tandem solar cells, carefully matching them with high voltage RFBs, and dedicatedly designed zero-gap flow field architecture.

3.3 Results and Discussion

3.3.1 SFB device design and operations

Building a highly efficient integrated SFB device starts from designing the general structure of the device followed by developing and studying the individual components that fit well with the general structure. As illustrated in Figure 3.1a, we design a simple three-electrode device by incorporating a semiconductor photoelectrode into the conventional two-electrode device design that has been used for most RFBs.[26] Consequently, this device can be operated as normal RFBs by only using two carbon felt based inert electrodes to charge and discharge the redox active species in the liquid electrolytes (Figure 3.1c), which are constantly circulated between the device and external storage tanks by pumps. More importantly, the charging of this device can also be accomplished by illuminating the photoelectrode with solar light to allow the harvest of photogenerated carries by redox active species at the semiconductor-liquid electrolyte interface (Figure 3.1d). We can also operate this device just as a PV solar cell by cycling the redox couples between the photoelectrode and the counter electrode to directly extract the electricity (Figure 3.1e), which is how regenerative PEC liquid junction solar cells work.[7] To improve the flow dynamics of electrolyte as well as minimize ionic and contact resistance between each component, we configure the new integrated device to allow the membrane, electrode and current collector all in direct contact (Figure 3.1), resembling the zero-gap flow field cell architecture of RFBs.[34]

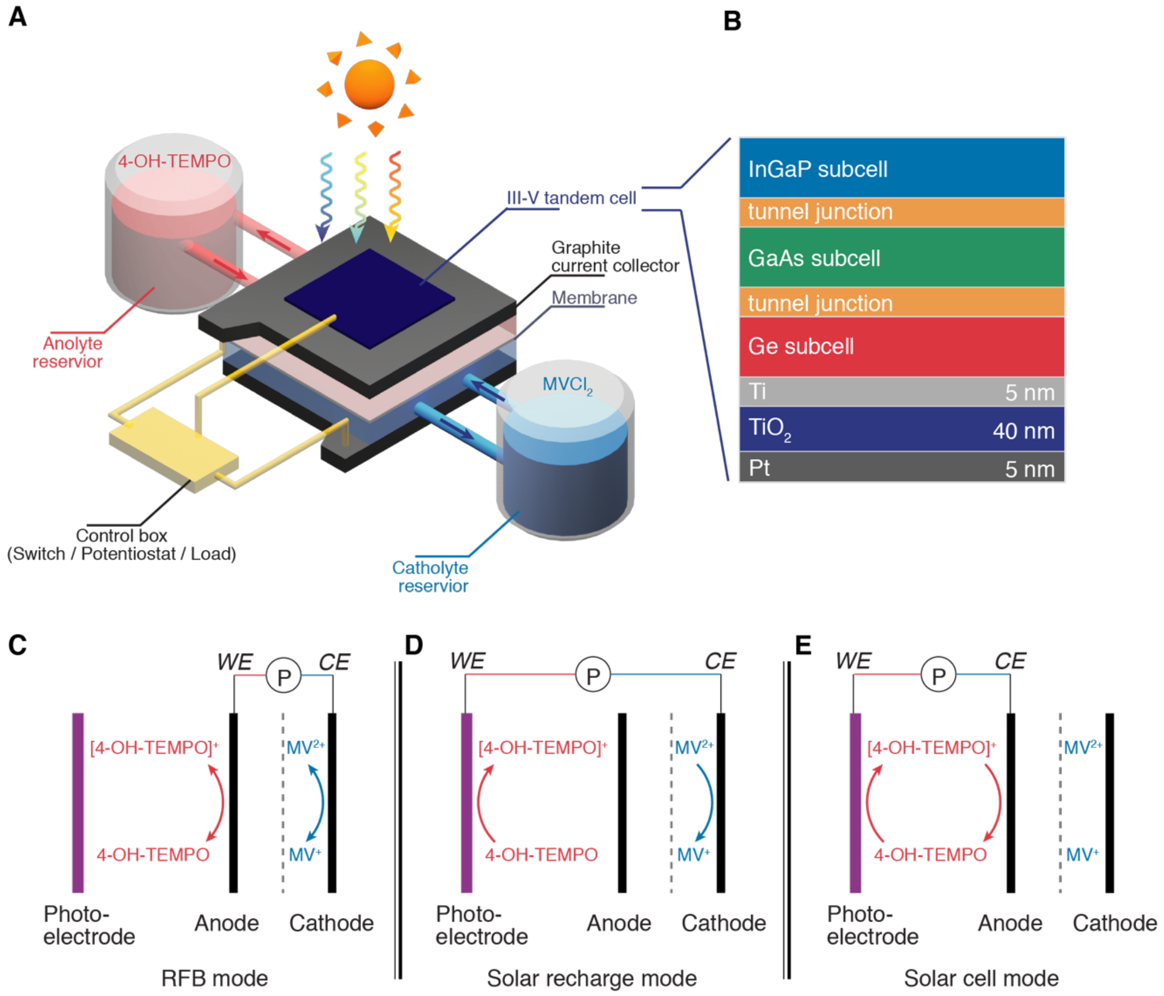

Figure 3.1. Schematic SFB Device Design and Operations. a, Integrated SFB device using III-V tandem cell photoelectrode and 4-OH-TEMPO/MVCl$_2$ redox couples. **b**, Architecture of the photoelectrode based on InGaP/GaAs/Ge tandem solar cell protected by Ti/TiO$_2$/Pt layers on the surface of the Ge bottom cell. **c-e**, The integrated device configuration under different operation modes: RFB mode (**c**); solar recharge mode (**d**); solar cell mode (**e**). The definition of anode and cathode follows the charging process.

3.3.2 Electrochemical characterization of redox couples

We choose low-cost organic redox couples 4-hydroxy-2,2,6,6-tetramethylpiperidin-1-oxyl (4-OH-TEMPO) and methyl viologen (MV) as the anolyte and the catholyte, respectively, for the integrated SFB device. Attributed to their proper formal potential (E^0) matching, the combination of 4-OH-TEMPO and MV enabled a recent demonstration of RFBs with an exceptional high cell voltage of 1.25 V (Figure 3.2a), which is a significant high value for aqueous organic RFBs.[35] Although the potential difference between the two redox couples already reach the limit of thermodynamic water splitting potential (1.23 V), the large overpotentials of water oxidation and reduction reactions on carbon based electrodes under neutral condition leave at least 400 mV on each side to practically operate the anodic and cathodic redox reactions without electrolysis of water. On account of the large E^0 difference between the two redox couples, we utilized a high photovoltage triple junction III-V tandem photoelectrode that consists of an InGaP top cell (E_g = 1.85 eV), a GaAs middle cell (E_g = 1.42 eV) and a Ge bottom cell (E_g = 0.67 eV) (Figure 3.1b, see more device details in Figure A2.2).[36] Such monolithic III-V tandem heterojunctions have been proven the best for high-efficiency solar cells and further have been shown to be an excellent candidate for PEC water splitting due to its near-ideal band gap energy and adsorption spectrum match with solar irradiation.[33,37] Moreover, the III-V tandem cell can provide a high photovoltage (2.4 V) out of a single cell. This high photovoltage, although not specifically critical for PV cells as the panel voltage can be easily increased by series tandem, is a key beneficial feature in integrated SFB device design to enable efficient photocharging of the device without external bias and a simpler 3-electrode SFB device design (as shown in Figure 3.1a). Compared with the 4-electrode SFBs previously demonstrated,[29] the 3-electrode SFBs are easier to fabricate and operate, because only one photoelectrode is needed and illumination comes from one side. Another advantage of these 4-OH-TEMPO and MV redox couples is that they both have relatively large solubility (> 0.5 M) in neutral solution, thus by using neutral rather than acidic or alkaline electrolyte, the corrosiveness of the electrolyte could be greatly reduced and more stable devices can be readily achieved.

We then studied the redox couples, which serve as the bridge connecting photocharging and electrical discharging processes. The E^0 for 4-OH-TEMPO and MV redox couples are 0.80 V and -0.45 V in 2 M NaCl solution, respectively (Figure 3.2a). Besides the proper E^0, the electrochemical kinetics and reversibility of the redox couples are also important for the power capability of RFB[27] and even more important for the efficient charge transfer from the semiconductors to electrolytes in PEC devices.[29] Detailed cyclic voltammetry studies at various scan rates (Figure A2.3) revealed that both redox couples have remarkable electrochemical reversibility and rapid diffusion rate, similar to that of other commonly used fast organic redox couples, such as quinones.[24] Building on the excellent electrochemical properties of the redox couples, we tested the RFB using 0.1 M 4-OH-TEMPO as anolyte and 0.1 M MV as catholyte, both with 2 M NaCl as supporting electrolyte. The RFB charging/discharging cycling test was carried out in the device shown in Figure A2.1 at desired constant current density with cut-off voltages of 0.5 V and 1.5 V. The representative cycling behavior at 20 mA cm^{-2} (Figure 3.2b) shows a stable voltage profile over at least 10 cycles with an average open-circuit voltage (*OCV*) around 1.2 V. The rate performance study of the RFB at various current densities (Figure 3.2c) shows that the current efficiency (*CE*) stays at 99% for all the rates while the energy efficiency (*EE*) drops from 91.9% to 73.0% as rate increases from 10 mA cm^{-2} to 50 mA cm^{-2}. The RFB cycling performance achieved by our SFB device is comparable to that of the previously demonstrated 4-OH-TEMPO/MV RFB,[35] indicating that, although not specifically optimized for RFB performance, the design of this integrated SFB device is competitive relative to the state-of-the-art RFB architecture.

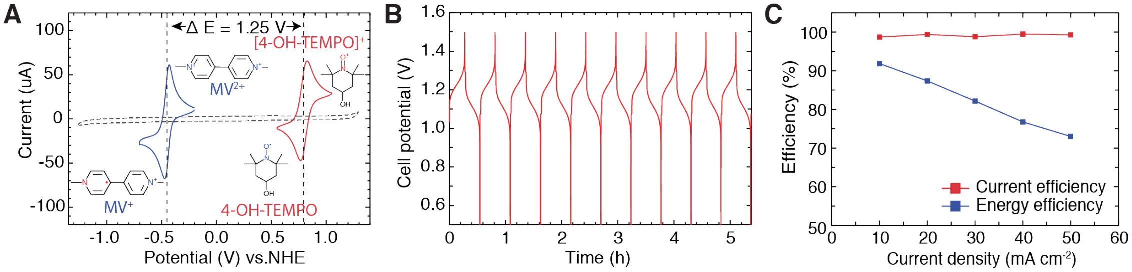

Figure 3.2. Cyclic Voltammogram and RFB Performance of the 4-OH-TEMPO/MV Redox Couples. a, Cyclic voltammogram of 5 mM 4-OH-TEMPO (red curve) and 5 mM $MVCl_2$ (blue curve) in 2 M NaCl scanned at 100 mV s^{-1} on a glassy carbon electrode showing a 1.25 V potential difference. Dotted line represents CV of 2 M NaCl background electrolyte scanned at 100 mV s^{-1}. **b**, Representative voltage profile during 10 charge-discharge cycles of the 0.1 M 4-OH-TEMPO/0.1 M $MVCl_2$ RFB. **c,** RFB current efficiency and energy efficiency at different current densities.

3.3.3 Performance of individual SFB components

We then characterized the performance of the solid-state III-V tandem solar cell under 1 sun (100 mW cm^{-2}) of AM 1.5 G simulated solar illumination. The linear sweep voltammetry curve in Figure 3A shows the solid-state tandem cell exhibits an open-circuit potential (V_{oc}) of 2.41 V, a short-circuit current density (J_{sc}) of 12.72 mA cm^{-2}, a fill factor (*FF*) of 85.0% and a power conversion efficiency (*PCE*) of 26.1%. Previous efforts to use III-V semiconductors in PEC cells showed that III-V semiconductors are very prone to photocorrosion in aqueous electrolytes, especially under extreme pH conditions that are conducive to PEC water electrolysis[36] Although the neutral electrolyte adopted in our SFB device partially alleviated the corrosive attack by H^+ or OH^- ions, a surface protection layer for the photoelectrode was still required to achieve a stable operation. TiO_2 has been widely used as the protection layer and shown good stability and low charge transfer resistance in aqueous electrolytes under various pH conditions.[38,39] Therefore, we deposited a Ti/TiO_2 (5 nm/40 nm) thin film on the back side of the III-V cell (Ge bottom cell side) using sputter coating and atomic layer deposition (ALD) to protect the photoelectrode. A 5 nm layer of Pt was then sputter-coated on top of the TiO_2 film to provide a stable ohmic contact between TiO_2 and electrolyte (see Figure 3.1B).

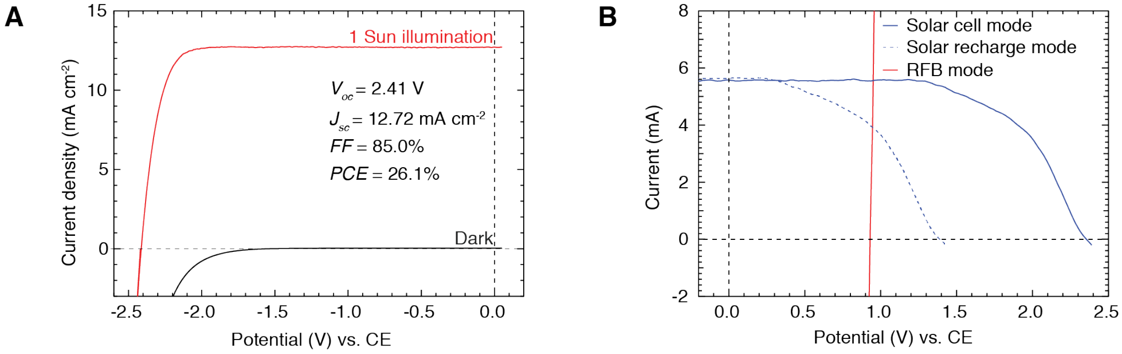

Figure 3.3. Performance of Individual SFB Components. a, *J-V* performance of solid state InGaP/GaAs/Ge tandem solar cell under 1 sun (AM 1.5 G) illumination (red) and in the dark (black). **b**, Overlaid *I-V* data for the individually measured photoelectrode and RFB components of the integrated device. Note that current instead of current density is shown here for a photoelectrode with an area of ~0.4 cm^2 and RFB electrodes with an area of 4 cm^2. *J-V* curve for the same photoelectrode is shown in Figure A2.6. The blue curves represent the PEC solar performance of the III-V tandem photoelectrode measured under solar cell mode (solid) and solar recharge mode (dashed) in 0.1 M 4-OH-TEMPO/0.1 M $MVCl_2$ electrolyte; the red line shows the polarization performance of the $MVCl_2$/4-OH-TEMPO RFB. The intersection of the solid blue curve and red line represents the operating point of the SFB device.

As illustrated in Figures 1D and 1E, we can configure the integrated SFB device to two different solar modes under illumination. Under solar cell mode (Figure 3.1e), the photoelectrode and anode are connected to allow photooxidation of 4-OH-TEMPO at the surface of photoelectrode and reduction of [4-OH-TEMPO]$^+$ at the surface of anode, just like regenerative PEC liquid junction solar cells.[7] Thus the solar energy input can be directly converted and delivered as electrical energy output to power external load. The PEC performance of the tandem photoelectrode in 0.1 M of 4-OH-TEMPO aqueous solution under 1 sun simulated illumination using an EKE-type lamp (solid blue curve in Figure 3B) was very close to the *J-V* performance of the solid-state PV cell (Figure 3A), especially for the V_{oc} and J_{sc}. Note that Figure 3B is displayed in current not current density, as the areas of photoelectrode (~0.4 cm^2) and the carbon felt RFB electrode (4 cm^2) are different. The lower *FF* of the photoelectrode (60.3%) in comparison with that of the solid-state cell may be attributed to the mass transport losses of the 4-OH-TEMPO redox couple and the electrolyte ohmic losses between the photoelectrode and anode, which is commonly observed in many PEC cells.[3] In contrast, under solar recharge mode (Figure 3.1d), the photoelectrode and cathode are connected to drive the photooxidation of 4-OH-TEMPO at photoelectrode and simultaneous reduction of MV^{2+} at carbon felt cathode. Solar energy can be harvested by the photoelectrode and stored as chemical energy by the redox reactions under solar recharge mode and released under RFB mode (Figure 3.1c) as electrical energy when needed. The dashed blue curve in Figure 3B shows the PEC performance of the photoelectrode under solar recharge mode, which can be well matched by cathodically offsetting the solid blue curve. The potential offset between the two PEC *I-V* curves (~1.0 V) comes from the equilibrium potential (E_{eq}) difference between 4-OH-TEMPO and MV redox couples at the specific states of charge (SOC) where the measurements were performed, which agrees well with the *OCV* of the RFB tested at the same SOC (red line in Figure 3B). By overlaying the polarization curve of the RFB and the *I-V* curve of the photoelectrode under solar cell mode, the operation point of the integrated SFB can be found as the intersection of the two curves. From the overlaid *I-V* curves shown in Figure 3B, we can estimate a bias-free solar recharging current of 5.56 mA for the integrated SFB device.

Moreover, we use a specific figure of merit, solar-to-output electricity efficiency (*SOEE*) to evaluate the overall efficiency of the SFB device, which is defined as:

$$SOEE\ (\%) = \frac{E_{disarging}}{E_{illumination}} = \frac{\int I_{out}V_{out}dt}{\int SAdt}, \tag{1}$$

where $E_{discharging}$ is the usable electrical energy delivered by the integrated SFB device and $E_{illumination}$ is the total solar energy input.[29] If the RFB polarization curve intersects with the plateau part of the photoelectrode *J-V* curve (see an example in Figure 3B), then the *SOEE* of the integrated device can be estimated using the following equation:

$$Estimated\ SOEE = \frac{J_{sc}(photo) \times V_{oc}(RFB) \times CE \times VE}{S}, \tag{2}$$

where $J_{sc}(photo)$ is the short circuit current density of the photoelectrode; $V_{oc}(RFB)$ is the open circuit voltage of the RFB; *CE* and *VE* are the estimated current efficiency and voltage efficiency of the SFB. From the data shown in Figure 3B, we can estimate a *SOEE* of 13.3 % for the SFB device (see calculation details in Experimental Procedures).

3.3.4 Study of integrated SFB device

In light of the excellent and reproducible performance of the RFB as well as the good performance from the tandem III-V photoelectrode, we built the integrated SFB devices using the same RFB and PEC components (Figure A2.1). The cycling behavior of the SFB was characterized using two potentiostats configured to solar recharge mode and RFB mode, to monitor the photocurrent delivered by the photoelectrode and the cell potential of the integrated SFB device, respectively. The blue curve in Figure 4A shows that the photocurrent density under 1 sun illumination during the unassisted photocharging process stays at 14.5 mA cm^{-2} over 10 photocharging cycles with a fluctuation of ± 1 mA cm^{-2} that is likely due to the instability of the light source. Following each photocharging cycle, the device was discharged by applying a discharging current of -10 mA until the cell potential reached 0.5 V. The current efficiency (*CE*) and voltage efficiency (*VE*) of the SFB can be calculated using the same methods used for normal RFBs. Figure A2.4 shows the integrated device features both high *CE* and *VE*, with average efficiencies of 96.2 % and 96.6 % over 10 cycles, respectively. Based on the cycling data, we can calculate the actual *SOEE* for the SFB to directly evaluate its overall efficiency. The integrated SFB device achieved a stable *SOEE* over 10 cycles with an average of 14.1 %, which is over 8 times higher than the prototype device demonstrated previously[29] and the highest published so far among all integrated solar rechargeable battery devices.[10,11] To compare more broadly, the *SOEE* and other key performance metrics of reported representative SFBs and other solar rechargeable batteries are summarized in Table A2.1.

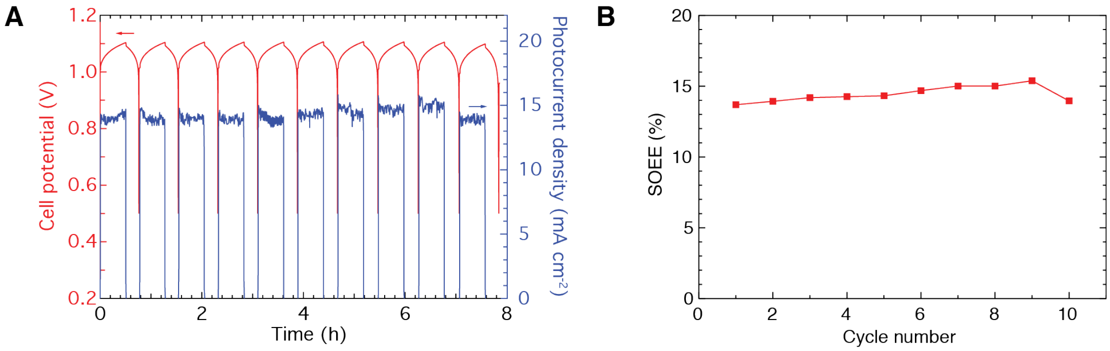

Figure 3.4. Integrated SFB Device Performance. a, A representative device cycling behavior showing cell potential between cathode and anode, as well as the photocurrent density delivered by the photoelectrode for 10 cycles. The cycling test was performed with no bias potential input during charging process and a current of -10 mA during discharging process.**b**, The SFB displayed a stable SOEE around 14 % for 10 cycles.

3.3.5 Design principles for highly efficient SFB device

The record *SOEE* achieved by the integrated SFB device demonstrated here is enabled by the following set of design principles. First, just like the RFBs,[27] for the integrated SFB devices, even with the same photelectrode and electrolyte, different flow cell structures could result in significantly different device performance and characteristics, especially for the liquid junction photoelectrodes that are more sensitive to the mass transfer rate of redox active species.[40] To accommodate all the components and functions yet maintain a high performance, the SFB device should be dedicatedly designed and optimized. The zero-gap structure of the SFB device employed here only allow a very thin liquid layer (~2 mm) contacting with the photelectrode, thus ensures effective diffusion and convection of redox couples at moderate flow rate. More importantly, comparison of the efficiency of the RFB component and solar component clearly shows that the

SOEE is mainly limited by the solar conversion efficiency of the photoelectrode here. The photoelectrode used here was fabricated with a triple junction III-V solar cell that can absorb most of the solar irradiation across the whole solar spectrum to provide a high *PCE* and more importantly, a high photovoltage. Last, the E^0 difference between the redox couples used in anolyte and catholyte determines the cell voltage of the SFB, which can significantly affect the *SOEE* (as suggested by equation 2) as well as the energy and power capacity of the device.

The highly efficient SFB device demonstrated here illustrates the general principles for designing a highly efficient SFB device with the available high performance solar cells and RFBs: the RFB cell voltage should be matched as close as possible to the maximum power point of the photoelectrode (Figure 5). In the specific case at hand, the 4-OH-TEMPO/MV redox couple combination boasts one of the highest cell voltage (1.25 V) among the aqueous organic RFBs demonstrated so far, which is a great boost for the *SOEE*. To drive the unassisted photocharging of SFBs with such a high cell voltage, the V_{oc} produced by photoelectrode needs to be at least 1.4 V to compensate for the inevitable voltage losses. Therefore, V_{oc} higher than 1.8 V is generally not useful for driving the 4-OH-TEMPO/MV redox reactions. This means that an excess photovoltage of around 0.6 V produced by the tandem III-V photoelectrode was not contributing to the *SOEE* herein. This voltage mismatch is the most significant reason for the efficiency loss from the *PCE* of the solar cells to the final *SOEE*. As illustrated in Figure 5, if a RFB with an even higher cell voltage can be employed to shift the solid red RFB polarization curve to the hypothetic dash red curve in Figure 5, it can not only improve the *SOEE* but also raise the energy density of the SFB. Therefore, there is still much untapped potential in the tandem III-V photoelectrode to further increase the SOEE of SFBs. With many new and emerging redox couples that are being developed for RFBs,[22-28] such as the one reported recently,[41] this strategy promises a clear pathway for future developments. Moreover, not only is high (photo)voltage highly desirable for both the RFBs and the photoelectrodes used in SFBs, but also properly matching their voltages is the critical factor for taking advantage of such high efficiency solar cells to enable the highest *SOEE* out of the integrated SFBs. An alternative strategy for improving voltage matching could be boosting the photocurrent density (J_{sc}) of the photoelectrode, which is usually accompanied by some sacrifice in the photovoltage (from solid blue to dash blue curve in Figure 5); but as long as the photovoltage is still higher than the RFB cell voltage, we can still achieve intersection at maximum power point. Such design would involve tuning the band structures of the tandem III-V photoelectrodes or integrating other materials into tandem double junctions,[42] therefore more complicated.

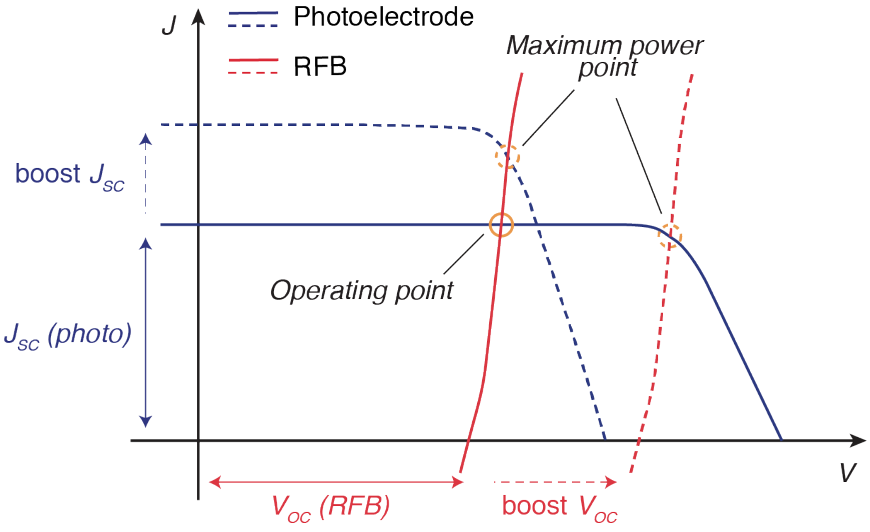

Figure 3.5. Estimation Method and Pathways to Boost the *SOEE* of SFB Device. Overlaid hypothetical current-potential behavior for photoelectrodes and RFBs, showing the scenarios of working voltage mismatch (solid curves) and ideal match (dash curves). The highest *SOEE* can be achieved by matching the RFB cell voltage with the maximum power point of the photoelectrode. This can be accomplished by either increasing the RFB cell voltage (V_{oc}) to match the given photoelectrode, or boosting the photocurrent density (J_{sc}) of the photoelectrode to match with the given RFB working voltage, allowing the polarization curve of RFB to intersect with the maximum power point of the photoelectrode.

Due to the expensive III-V substrates and heteroepitaxial growth, the manufacturing cost for tandem III-V photoelectrodes may be too high to be employed for practical applications. At this early stage of the development for SFBs, we are trying to demonstrate the design principles and push the boundaries to show what could be possibly achieved, with some sacrifice of the cost-effectiveness. However, the cost for III-V cells may be reduced in the future by designing simpler tandem cells with a sufficiently high photovoltage[42] or adopting new fabrication methods, such as epitaxial lift-off (ELO).[43] With further developments and proper device design following the design principles laid out herein, we believe that the capital cost for monolithically integrated SFB devices will not be higher than individually operated PV devices plus RFBs. Furthermore, developing new semiconductor materials[30] and incorporating them into more efficient liquid junction cells[7,31,32] could further simplify the SFB photoelectrode fabrication process and lower the cost.

3.4 Conclusions

In conclusion, building on novel device design and a set of rational design principles, we demonstrated a high performance monolithic solar energy conversion and storage device using highly efficient and high photovoltage tandem III-V solar cells and high voltage 4-OH-TEMPO/MV RFBs. The integrated SFB device can be easily configured to 3 different operation modes to fit specific application requirements. Enabled by high efficiency photoelectrode, properly matched redox couples, and carefully designed flow field design, a record *SOEE* of 14.1% has been achieved for the SFB. Following the design rules proposed herein, the efficiency of such SFB devices in general could be further boosted by better voltage matching of the RFBs and solar cells, either by enlarging the RFB cell potential with better redox couple choices or tuning the band structure of solar cells to improve its J_{sc}. This work paved the way for a practical new approach to harvesting, storing and utilizing the intermittent solar energy with unprecedented high energy conversion efficiency and energy storage density. These integrated SFBs will be especially suitable as distributed and stand-alone solar energy conversion and storage systems in remote locations and enable practical off-gird electrification.

3.5 Methods

3.5.1 Fabrication of RFB and Integrated SFB Device

The RFB and SFB measurements were carried out in a custom-made zero-gap device (Figure A2.1). Two end frames and two hose adaptor frames were machined out of solid stainless steel and solid PVDF blocks, respectively. Current collectors were 45 × 45 mm^2 graphite plates (1/8-inch thickness) with a 20 × 20 × 1.2 mm pocket to place carbon felt electrodes. Current collectors with additional 10 × 10 mm clearance window at the center of the square pocket were used for SFB devices (only on the anode side) to allow direct contact between photoelectrode and liquid electrolyte. 4 cm^2 carbon felt electrodes (GFD 3 EA, SIGRACELL®) were pre-treated at 400 ^{o}C in air for 6 hours before being used on both sides of the cell. FAA-3-50 membrane (Fumatech) was used as an anion-exchange membrane, which was soaked in 1 M NaCl for 24 hours before use. The cell was assembled with four pieces of PTFE (0.04-inch thickness) sheets as gaskets and tightened with eight #10-24 bolts torqued to 4.0 Nm. 20 mL solution of 0.1 M 4-hydroxy-2,2,6,6-tetramethylpiperidin-1-oxyl (4-OH-TEMPO, AK Scientific) in 2 M NaCl (Sigma Aldrich) and 10 mL solution of 0.1 M 1,1'-Dimethyl-4,4'-bipyridinium dichloride ($MVCl_2$, Fisher Scientific) in 2 M NaCl were used as anolyte and catholyte, respectively. (Note that, $MVCl_2$ is toxic and should be carefully handled to avoid releasing to environment.) The electrolytes were pumped via Viton tubing through the flow channels at a rate of 20 mL/min by a peristaltic pump (Cole-Parmer Masterflex L/S). All RFB and SFB measurements were carried out in a custom modified N_2 flush box (Terra Universal) with continues N_2 flushing.

3.5.2 Electrochemical Measurements

Cyclic voltammogram measurements (Figure 3.2a and Figure A2.3) were conducted using a Bio-Logic SP-200 potentiostat. A 3 mm diameter glassy carbon disk electrode (BASi) was used as the working electrode, which was polished using 0.3 μm and 0.05 μm alumina slurry to mirror shine and washed with deionized water (Milli-Q, 18.2 MΩ cm) and methanol before each test. A Pt wire electrode (CH Instruments) and a saturated calomel electrode (SCE, CH Instruments) were used as the counter and reference electrode, respectively. 4-OH-TEMPO and $MVCl_2$ were used as received to prepare a 5 mM solution of each redox couple with 2 M NaCl as supporting electrolyte. The peak current versus the square root of the scan rate (v) are plotted in Figures S3C, D and fitted with a straight line. Randles-Sevèik equation as $i_p = 2.69 \times 10^5 n^{3/2} D^{1/2} c v^{1/2} A$, where number of electrons involved in the electrochemical reaction $n = 1$, $MVCl_2$ and 4-OH-TEMPO concentration $c = 5 \times 10^{-6}$ mol cm^{-3}, electrode area $A = 0.0707$ cm^2, was used to calculated the diffusion coefficient (D) of the redox couples from the slope of the fitted line. This yields $D_R = 6.53 \times 10^{-6}$ cm^2 s^{-1} and $D_O = 3.31 \times 10^{-6}$ cm^2 s^{-1} for $MVCl_2$ redox couples and $D_R = 4.14 \times 10^{-6}$ cm^2 s^{-1} and $D_O = 4.12 \times 10^{-6}$ cm^2 s^{-1} for 4-OH-TEMPO redox couples.

3.5.3 RFB Measurements

The RFB cycling and polarization performance tests were carried out using a Bio-Logic SP-200 potentiostat. The RFB cycling tests were performed by charging and discharging the battery at a desired constant current density with 0.5 V and 1.5 V as bottom and top potential limits, respectively. In the cell polarization characterization, a linear sweep voltammetry (LSV) scan was performed at a scan rate of 100 mV/s. Potentiostatic electrochemical impedance spectroscopy (EIS) measurement of the RFB was performed at 0 SOC, 1.0 V bias with a voltage offset of 10 mV, and frequencies ranging from 200 kHz to 1 Hz (Figure A2.5).

3.5.4 Fabrication of III-V tandem cells with thin film protection layers

The GaInP/GaAs/Ge triple-junction solar cell consists of a n/p GaInP junction top cell (E_g = 1.80 eV), a n/p GaAs junction middle cell (E_g = 1.42 eV) and a n/p Ge junction bottom cell (E_g

= 0.66 eV). Prior to the growth process, a p-type [100]-oriented germanium substrate was chemically cleaned. After the cleaning process, III–V layer structures were deposited on Ge substrate by metalorganic chemical vapor deposition (MOCVD). Trimethyl gallium (TMGa), trimethyl aluminum (TMAl) and trimethyl indium (TMIn) were used as the sources for the Group-III elements; arsine (AsH_3) and phosphine (PH_3) were used as the source gases for the Group-V elements. Silane (SiH_4) was used as the source of donor impurity, while the sources of acceptor impurities were diethyl zinc (DEZn) and bis-cyclopentadiethyl magnesium (Cp_2Mg).

As illustrated in Figure A2.2a, the Ge bottom cell was formed by a 150 μm p-Ge base layer, a 300 nm n-Ge emitter and a 25 nm n-GaInP window layer. The GaAs middle cell was formed by a 30 nm p-AlGaAs back surface field (BSF) layer, a 25 μm p-GaAs base layer, a 100 nm n-GaAs emitter and a 100 nm n-AlInP window layer. The GaInP top cell was formed by a 50 nm p-AlGaAs BSF layer, a 6700 nm p-GaInP base layer, a 30 nm n-GaInP emitter and a 30 nm n-AlGaAs window layer. The tunnel junction consisting of a 10 nm n^{++}-AlGaAs layer and a 10 nm p^{++}-AlGaAs layer was used to connect each sub-cell. The thickness of the subcell was confirmed with cross-section scanning electron microscope (SEM) image (Figure A2.2b).

A dual-layered SiO_2/TiO_2 antireflection coating (7 nm) was evaporated on the top side of the triple-junction device followed by a top metal contact grid (10 nm Ti/ 90 nm Au) realized by photo-lithography and e-beam evaporation. A Ge/Au eutectic layer was deposited on the back side of Ge wafer to form ohmic contact. For making the photoelectrodes to be used in the integrated SFBs, a thin (5 nm) layer of titanium was first sputter coated and followed by a 40 nm thick layer of TiO_2 thin film deposited by atomic layer deposition (ALD) using tetrakis(dimethylamino) titanium (TDMAT) and O_2-plasma precursors at 150 ºC in ~200 mTorr Ar environment on the back side of the triple-junction device. On top of that, another layer of 5 nm thick platinum thin film was sputter deposited to minimize the charge extraction barrier. All of the sputter coatings were carried out using dc magnetron sputtering method with a power of 400W.

3.5.5 Fabrication of photoelectrode assembly for the integrated SFB device

The photoelectrode assembly for the integrated SFB device characterization was fabricated by affixing the III-V tandem cell photoelectrode described above onto a custom-made graphite current collector (described in the SFB device fabrication section) by epoxy resin (Hysol 9460) to cover the window of the current collector. The back side of the III-V cell (Ge side) was only physically attached to the current collector without forming an electrical contact. The 4-OH-TEMPO electrolyte can directly contact with the back side of the III-V cell through the window of the current collector and harvest photogenerated holes during SFB device operation in solar recharge mode and solar cell mode. The ohmic contact to III-V photoelectrode was made by attaching a copper foil onto the front side of the cell (InGaP side) with Ga/In eutectic mixture (Sigma Aldrich) and fixed with silver paint (Ted Pella, PELCO colloidal silver). The ohmic contact area was sealed by epoxy resin. The geometric area of the exposed III-V cell was determined using calibrated digital images and Photoshop, which was usually between 0.35 cm^2 and 0.5 cm^2.

3.5.6 Solid state and photoelectrochemical (PEC) characterization of the III-V tandem cells

Solid state *J-V* performance of the III-V cells were measured in a two-electrode configuration by making ohmic contact to the front and back side of the cell. The data was collected using a Bio-Logic SP-200 potentiostat under 1 Sun (100 mW cm^2) of AM 1.5 G simulated illumination by a Newport Model 91191 solar simulator. A Si photodiode (Thorlabs) was used to calibrate the illumination intensity of the AM 1.5G solar simulator to 100 mW/cm^2.

The PEC characteristics of the III-V tandem photoelectrode were measured in the assembled SFB device with a Bio-Logic SP-200 potentiostat under 1 Sun (100 mW/cm^2) of simulated solar illumination using an EKE-type tungsten-halogen lamps (USHIO) in a N_2 flush box. To calibrate the EKE-type solar simulator, the short-circuit current of a solid-state p^+nn^+ Si solar cell (~ 1.2 cm^2) was first measured under 1 Sun of AM1.5 G simulated solar light, then the EKE-type solar simulator was calibrated to generate the same short-circuit current using the same solid-state p^+nn^+ Si solar cell. The PEC measurements were performed in a two-electrode configuration under both solar cell mode and solar recharge mode (Figures 1D, E) with the same electrolytes used in the RFB test (0.1 M 4-OH-TEMPO as anolyte and 0.1 M $MVCl_2$ as catholyte, both with 2 M NaCl as supporting electrolyte). All LSV curves were measured at a scan rate of 100 mV/s without correcting for any uncompensated resistance losses.

3.5.7 Integrated SFB device characterization

To characterize the charging-discharging behaviors of the integrated SFB devices, two Bio-Logic SP-200 potentiostats were used: potentiostat 1 was configured as solar recharge mode (Figure 3.1d) to monitor the photocurrent; potentiostat 2 was configured as RFB mode (Figure 3.1c) to monitor the potential difference between the two electrodes. During the photocharging process, III-V photoelectrode was illuminated by the EKE-type simulated solar illumination at 1 Sun without applying any external bias by potentiostat 1. During the discharging process, the illumination was turned off and the integrated device was operated as a normal RFB with a discharging current of -10 mA applied by potentiostat 2 until the cell potential reached 0.5 V.

The PEC characteristics of the photoelectrodes used in the SFB devices were examined before and after integrated device cycling test based on the methods described in the previous section to check the stability of the III-V photoelectrodes (Figure A2.6).

3.5.8 Calculation of Solar-To-Output Electricity Efficiency (*SOEE*)

Because electricity is not directly extracted from the solar conversion device in integrated SFBs, the conventional power conversion efficiency (*PCE*) used to define solar PV cells is not the most suitable metrics. In order to quantitatively evaluate the solar conversion efficiency of the integrated device, a new figure of merit for this type of integrated SFB devices should be considered: solar-to-output electricity efficiency (SOEE), which is defined by the ratio of the usable electrical energy delivered by the integrated SFB device ($E_{discharging}$) over the total solar energy input ($E_{illumination}$). The SOEE can be calculated using equation 1:

$$SOEE\ (\%) = \frac{E_{disarging}}{E_{illumination}} = \frac{\int I_{out} V_{out} dt}{\int SAdt}$$

where I_{out} is the output (discharging) current, V_{out} is the output voltage, *S* is the total incident solar irradiance, which is provided by the EKE-type light source at 100 mW/cm^2, and A is the illumination area of photoelectrode. Note that this *SOEE* is the *round-trip efficiency* of the delivered electrical energy over the original solar energy input. If we compare with PEC water splitting, this *SOEE* is equivalent to the total efficiency after considering both the solar-to-hydrogen conversion efficiency of PEC water splitting device and the efficiency of the fuel cell that generates electricity from the hydrogen fuel.

If the RFB polarization curve intersects with the plateau part of the PEC *J-V* curve (Figure 5), then the *SOEE* of the integrated device can be estimated using equation 2:

$$Estimated\ SOEE = \frac{J_{sc}(photo) \times V_{oc}(RFB) \times CE \times VE}{S}$$

$$\approx \frac{J_{sc}(photo) \times V_{oc}(photo) \times FF \times V_{oc}(RFB)}{S \times V_{oc}(photo) \times FF} \times CE \times VE = \frac{\eta\ (photo)}{FF} \times \frac{V_{oc}(RFB)}{V_{oc}(photo)} \times CE \times VE$$

where $J_{sc}(photo)$ is the short circuit current density of the photoelectrode; $V_{oc}(RFB)$ is the open circuit voltage of the RFB; CE and VE are the current efficiency and voltage efficiency of the RFB operated under similar conditions (same charging current, charging time and potential limits, Figure A2.7); S is the total incident solar irradiance; $V_{oc}(photo)$ is the open circuit potential of the photoelectrode; FF is the fill factor of the photoelectrode; $\eta\ (photo)$ is the power conversion efficiency of the photoelectrode:

$$Estimated\ SOEE = \frac{\eta\ (photo)}{FF} \times \frac{V_{oc}(RFB)}{V_{oc}(photo)} \times CE \times VE$$

$$= \frac{20.6\ \%}{60.3\ \%} \times \frac{1.01\ V}{2.36\ V} \times 95.5\ \% \times 95.6\ \% = 13.3\ \%$$

3.6 References

1. Lewis, N. S. Research opportunities to advance solar energy utilization. *Science* **351**, aad1920 (2016).

2. Honda, K. & Fujishima, A. Photolysis-decomposition of water at the surface of an irradiated semiconductor. *Nature* **238**, 37-38 (1972).

3. Walter, M. G. *et al.* Solar water splitting cells. *Chem. Rev.* **110**, 6446-6473 (2010).

4. Nocera, D. G. The artificial leaf. *Acc. Chem. Res.* **45**, 767-776 (2012).

5. Montoya, J. H. *et al.* Materials for solar fuels and chemicals. *Nat. Mater.* **16**, 70-81 (2017).

6. Luttmer, J. D., Konrad, D. & Trachtenberg, I. Electrode materials for hydrobromic acid electrolysis in texas-instruments solar chemical converter. *J. Electrochem. Soc.* **132**, 1054-1058 (1985).

7. Heller, A., Miller, B. & Thiel, F. A. 11.5% solar conversion efficiency in the photocathodically protected *p*-InP/V^{3+}-V^{2+}-HCl/C semiconductor liquid junction cell. *Appl. Phys. Lett.* **38**, 282-284 (1981).

8. Yang, Z. *et al.* Electrochemical energy storage for green grid. *Chem. Rev.* **111**, 3577-3613 (2011).

9. Hodes, G., Manassen, J. & Cahen, D. Photoelectrochemical energy conversion and storage using polycrystalline chalcogenide electrodes. *Nature* **261**, 403-404 (1976).

10. Schmidt, D., Hager, M. D. & Schubert, U. S. Photo-rechargeable electric energy storage systems. *Adv. Energy Mater.* **6**, 1500369 (2015).

11. Yu, M. *et al.* Solar-powered electrochemical energy storage: An alternative to solar fuels. *J. Mater. Chem. A* **4**, 2766-2782 (2016).

12. Gurung, A. & Qiao, Q. Solar Charging Batteries: Advances, Challenges, and Opportunities. *Joule*, 1-14 (2018).

13. Paolella, A. *et al.* Light-assisted delithiation of lithium iron phosphate nanocrystals towards photo-rechargeable lithium ion batteries. *Nat. Commun.* **8**, 14643-14610 (2017).

14. Licht, S., Hodes, G., Tenne, R. & Manassen, J. A light-variation insensitive high efficiency solar cell. *Nature* **326**, 863-864 (1987).

15. Cheng, Q. *et al.* Photorechargeable high voltage redox battery enabled by Ta_3N_5 and GaN/Si dual-photoelectrode. *Adv. Mater.* **351**, 1700312-1700318 (2017).

16. Yu, M. *et al.* Aqueous lithium-iodine solar flow battery for the simultaneous conversion and storage of solar energy. *J. Am. Chem. Soc.* **137**, 8332-8335 (2015).

17. Liao, S. *et al.* Integrating a dual-silicon photoelectrochemical cell into a redox flow battery for unassisted photocharging. *Nat. Commun.* **7**, 11474-11478 (2016).

18. Wedege, K., Azevedo, J., Khataee, A., Bentien, A. & Mendes, A. Direct solar charging of an organic-inorganic, stable, and aqueous alkaline redox flow battery with a hematite photoanode. *Angew. Chem. Int. Ed.* **55**, 7142-7147 (2016).

19. Liu, P. *et al.* A Solar Rechargeable Flow Battery Based on Photoregeneration of Two Soluble Redox Couples. *ChemSusChem* **6**, 802-806 (2013).

20. Wedege, K. *et al.* Unbiased, complete solar charging of a neutral flow battery by a single Si photocathode. *RSC Advances* **8**, 6331-6340 (2018).

21. Zhou, Y. *et al.* Efficient Solar Energy Harvesting and Storage through a Robust Photocatalyst Driving Reversible Redox Reactions. *Adv. Mater.* **103**, 1802294-1802297 (2018).

22. Ding, Y., Li, Y. F. & Yu, G. H. Exploring Bio-inspired Quinone-Based Organic Redox Flow Batteries: A Combined Experimental and Computational Study. *Chem* **1**, 790-801 (2016).

23. Ding, Y. & Yu, G. A Bio-Inspired, Heavy-Metal-Free, Dual-Electrolyte Liquid Battery towards Sustainable Energy Storage. *Angew. Chem. Int. Ed.* **55**, 4772-4776 (2016).

24. Huskinson, B. *et al.* A metal-free organic-inorganic aqueous flow battery. *Nature* **505**, 195-198 (2014).

25. Kwabi, D. G. *et al.* Alkaline Quinone Flow Battery with Long Lifetime at pH 12. *Joule* (2018).

26. Park, M., Ryu, J., Wang, W. & Cho, J. Material design and engineering of next-generation flow-battery technologies. *Nature Reviews Materials* **2**, 16080-16018 (2016).

27. Weber, A. Z. *et al.* Redox flow batteries: A review. *J. Appl. Electrochem.* **41**, 1137-1164 (2011).

28. Ding, Y., Zhang, C., Zhang, L., Zhou, Y. & Yu, G. Molecular engineering of organic electroactive materials for redox flow batteries. *Chem. Soc. Rev.* **47**, 69-103 (2018).

29. Li, W. *et al.* Integrated photoelectrochemical solar energy conversion and organic redox flow battery devices. *Angew. Chem. Int. Ed.* **55**, 13104-13108 (2016).

30. Sivula, K. & van de Krol, R. Semiconducting materials for photoelectrochemical energy conversion. *Nature Reviews Materials* **1**, 15010 (2016).

31. Cha, H. G. & Choi, K. S. Combined biomass valorization and hydrogen production in a photoelectrochemical cell. *Nat Chem* **7**, 328-333 (2015).

32. Kamat, P. V., Tvrdy, K., Baker, D. R. & Radich, J. G. Beyond Photovoltaics: Semiconductor Nanoarchitectures for Liquid-Junction Solar Cells. *Chem. Rev.* **110**, 6664-6688 (2010).

33. Khaselev, O. & Turner, J. A. A monolithic photovoltaic-photoelectrochemical device for hydrogen production via water splitting. *Science* **280**, 425-427 (1998).

34. Aaron, D. S. *et al.* Dramatic performance gains in vanadium redox flow batteries through modified cell architecture. *J. Power Sources* **206**, 450-453 (2012).

35. Liu, T., Wei, X., Nie, Z., Sprenkle, V. & Wang, W. A total organic aqueous redox flow battery employing a low cost and sustainable methyl viologen anolyte and 4-HO-TEMPO catholyte. *Adv. Energy Mater.* **6**, 1501449 (2015).

36. Huang, C.-W., Liao, C.-H., Wu, C.-H. & Wu, J. C. S. Photocatalytic water splitting to produce hydrogen using multi-junction solar cell with different deposited thin films. *Sol. Energy Mater. Sol. Cells* **107**, 322-328 (2012).

37. Verlage, E. *et al.* A monolithically integrated, intrinsically safe, 10% efficient, solar-driven water-splitting system based on active, stable earth-abundant electrocatalysts in conjunction with tandem III-V light absorbers protected by amorphous TiO_2 films. *Energy Environ. Sci.* **8**, 3166-3172 (2015).

38. Mei, B. *et al.* Crystalline TiO_2: A generic and effective electron-conducting protection layer for photoanodes and -cathodes. *J. Phys. Chem. C* **119**, 15019-15027 (2015).

39. Hu, S. *et al.* Amorphous TiO_2 coatings stabilize Si, GaAs, and GaP photoanodes for efficient water oxidation. *Science* **344**, 1005-1009 (2014).

40. Gibbons, J. F., Cogan, G. W., Gronet, C. M. & Lewis, N. S. A 14% efficient nonaqueous semiconductor/liquid junction solar cell. *Appl. Phys. Lett.* **45**, 1095-1094 (1984).

41. DeBruler, C. *et al.* Designer Two-Electron Storage Viologen Anolyte Materials for Neutral Aqueous Organic Redox Flow Batteries. *Chem* **3**, 961-978 (2017).

42. Vaisman, M. *et al.* 15.3%-Efficient GaAsP Solar Cells on GaP/Si Templates. *ACS Energe Lett.* **2**, 1911-1918 (2017).

43. Ward, J. S. *et al.* Techno-economic analysis of three different substrate removal and reuse strategies for III-V solar cells. *Prog. Photovolt. Res. Appl.* **24**, 1284-1292 (2016).

CHAPTER 4

A Long Lifetime Aqueous Organic Solar Flow Battery[*]

4.1 Abstract

Monolithically integrated solar flow batteries (SFBs) hold promise as compact stand-alone energy systems for off-grid solar electrification. Although considerable research has been devoted to studying and improving the round-trip efficiency of SFBs, little attention has been paid to the device lifetime. Herein, we demonstrate a neutral pH aqueous electrolyte SFB with robust organic redox couples and inexpensive silicon-based photoelectrodes. Enabled by the excellent stability of both electrolytes and protected photoelectrodes, this SFB device exhibits not only unprecedented stable continuous cycling performance over 200 hours but also a capacity utilization rate higher than 80%. Moreover, through comprehensive study on the working mechanisms of SFBs, we developed a new theory based on instantaneous solar-to-output electricity efficiency ($SOEE_{ins}$) toward more optimized device design and realized a significantly improved solar-to-output electricity efficiency (*SOEE)* of 5.4% from single-junction silicon photoelectrodes. The design principles presented in this work for extending device lifetime and boosting round trip energy efficiency will make SFBs more competitive for off-grid applications.

---

[*] This chapter was originally published in *Adv. Energy. Mater.* **9**, 1900918 (2019), in collaboration with Kerr, E., Goulet, M.-A., Fu, H.-C., Zhao, Y., Yang, Y., Veyssal, A., He, J.-H., Gordon, R. G., Aziz, M. J. and Jin, S.

4.2 Introduction

The monolithic integration of solar energy conversion and electrochemical energy storage offers a practical solution to provide uninterruptable power supply on demand regardless of the ebb and flow of solar irradiation. Although connecting photovoltaics (PVs) with batteries, as adopted by some solar farms nowadays,[1] can provide the same uninterruptable power supply, the high capital cost and large footprint of two separate devices limit the market cases feasible for this option.[2,3] In contrast, integrated solar energy conversion and storage may represent a more compact, efficient, and cost-effective approach for off-grid electrification.[4,5]

Among the many different types of "solar rechargeable battery" devices that have been reported[4-7] since the first demonstration in 1976,[8] integrated solar flow batteries (SFBs) hold great promises for practical applications because the solar component shares the same liquid electrolyte as the energy storage component,[9] which is based on redox flow batteries (RFBs) and can be easily scale-up.[3] Despite the significant progress, most of such integrated devices suffer from some common scientific and technical issues.[6,10] The first question one typically asks about any "solar device" is the efficiency. Due to the intrinsic efficiency limits of the solar energy conversion components and the working voltage mismatch between the solar energy conversion component and electrochemical energy storage component, the round-trip efficiency (i.e., solar-to-output electricity efficiency, *SOEE*) of most previously reported solar rechargeable devices rarely exceeded 5%.[4,6,10-17] It was recently demonstrated that by monolithically integrating III-V tandem junction solar cells with properly voltage matched RFBs, the integrated SFB device can deliver a *SOEE* of *14.1 %*.[18] Importantly, this comprehensive study[18] also revealed a set of general design principles that can further boost the SFB's efficiency. Primary among them is that the formal potential difference of selected redox couples needs to be closely matched with the photovoltage of the photoelectrodes at the maximum power point. Although III-V tandem junction solar cells can enable unprecedented high *SOEE*, the manufacturing cost for them ($40/W to over $100/W)[19] is too high for practical applications. The most widely produced crystalline silicon-based solar cells have the cost of $0.15/W to $0.25/W after decades of research and commercial deployment,[19] thus are a good candidate for practical SFBs owing to its high abundance and decent PV efficiency.

On the other hand, another important aspect, device lifetime, has received much less attention than efficiency, which could be partially attributed to different types of challenges involved in achieving longer device lifetime. As summarized in Table A3.1, none of the existing integrated SFB devices has shown a stable continuous cycling performance longer than 50 hours.[6] Generally, there are two major challenges preventing those devices from reaching long device lifetime. Firstly, many redox active species, although undergo facile redox reactions, are chemically or electrochemically unstable for long term energy storage.[20-24] The 1, 2-benzoquinone-3, 5-disulfonic acid (BQDS) redox couple used in a previous prototype SFB device[12] and other RFB works[25,26] is an example of such unstable redox species. It has been shown that the BQDS molecule is particularly susceptible to decomposition by Michael addition.[26] Secondly, the photocorrosion of semiconductor photoelectrodes by aqueous electrolytes has long been one of the biggest obstacles to the practical application of photoelectrochemical (PEC) cells.[27-29] This has prompted strategies such as the deposition of inert protection layers and utilization of less corrosive electrolytes to balance the lifetime and efficiency of photoelectrode.[29-31]

As pointed out by varies recent reports, the chemical cost of redox active materials would eventually become a tiebreaker for future RFBs with rapid technology development.[32,33] Although a detailed cost analysis for SFBs has not been performed, the cost of active materials is likely to be a significant contributor to the cost of SFB systems as well. Consequently, redox couples that are based on earth abundant elements, which include many organic and organometallic species, are attractive for developing SFBs. In comparison to the more mature inorganic redox species that have been commercially deployed (such as vanadium),[2] organic and organometallic compounds tend to be more prone to chemical decomposition.[22] However, one of the most stable organic RFBs reported so far[23,34-36] is based on bis((3-trimethylammonio)propyl) (BTMAP) functionalized viologen and ferrocene redox couples, which exhibits an exceptionally low capacity fade rate of 11.3 %/year. Such excellent stability of these molecules has been attributed to the suppression of a bimolecular annihilation mechanism by the strong electrostatic repulsion induced by the positive charge on the BTMAP side chains.[36] Moreover, these molecules also exhibit very low permeabilities across anion exchange membranes, possibly through enhanced charge and size exclusion. The good stability, high solubility in neutral solutions and suitable formal potential of the BTMAP redox couples make them a perfect fit for the long lifetime SFB.

In this paper, we report a neutral pH solar flow battery with a stable continuous cycling performance over 200 hours (100 cycles). This long lifetime device is built by integrating well protected silicon photoelectrodes with robust BTMAP functionalized organic viologen and ferrocene redox couples in neutral aqueous solutions. Moreover, building on a comprehensive study on the working mechanisms of SFBs, we introduce a new concept, instantaneous *SOEE* *($SOEE_{ins}$)*, and show that understanding of instantaneous *SOEE* and more optimized SFB design can greatly boost the overall *SOEE* from 1.7%[12] to 5.4% even though the same silicon photoelectrode design is used.

4.3 Results and Discussion

We synthesized the bis((3-trimethylammonio)propyl)-ferrocene dichloride (BTMAP-Fc) and bis (3-trimethylammonio)propyl viologen tetrachloride (BTMAP-Vi) following the method reported by Beh et al.[36] and characterized their electrochemical properties using 3-electrode cyclic voltammetry, steady state linear scan voltammetry and 2-electrode RFB cycling. Cyclic voltammograms show a formal potential difference of 0.735 V between these two redox couples (Figure 4.1a), which can be used to estimate the cell potential (E_{cell}) of the RFBs and SFBs built with these redox couples. As discussed later, although this E_{cell} does not fully utilize the stability window constrained by water splitting, it can be well matched with the photovoltage produced by two silicon photoelectrodes. We also confirmed good redox kinetics of both redox couples by steady state linear sweep voltammetry with rotating disk electrode (Figure A3.1). Then RFB tests were performed in the SFB device[18] we developed without the photoelectrodes. 0.2 M of BTMAP-Fc and 0.2 M of BTMAP-Vi were used as anolyte and catholyte, respectively, both with 1 M of NaCl as supporting electrolyte. The galvanostatic cycling tests were performed at 6 different current densities from 5 mA/cm^2 to 50 mA/cm^2 (Figure 4.1b). The RFB showed excellent Coulombic efficiencies (*CE*) of >99.9% at all rates (Figure 4.1c). We noticed that the energy efficiency is rather limited at high cycling rates as a result of high area specific resistance (ASR) of the Selemion DSV anion exchange membrane used. The lack of a high conductivity and low permeability anion exchange membrane remains a common issue in the development of high performance RFBs.[37] However, due to the greater limitation on current density of the photoelectrode and the smaller area of the photoelectrode (~1.2 cm^2) than that of RFB electrode (4 cm^2), the SFB device usually does not need to be operated at a current density higher than 10 mA/cm^2 based on the area of RFB electrode. (In practical applications, the areal size of photoelectrodes should be close to that of RFB electrodes, which can be realized with further device engineering and optimization.) Therefore, a high energy efficiency (>90%) for the electrochemical energy storage and redelivery process is guaranteed based on Figure 4.1c.

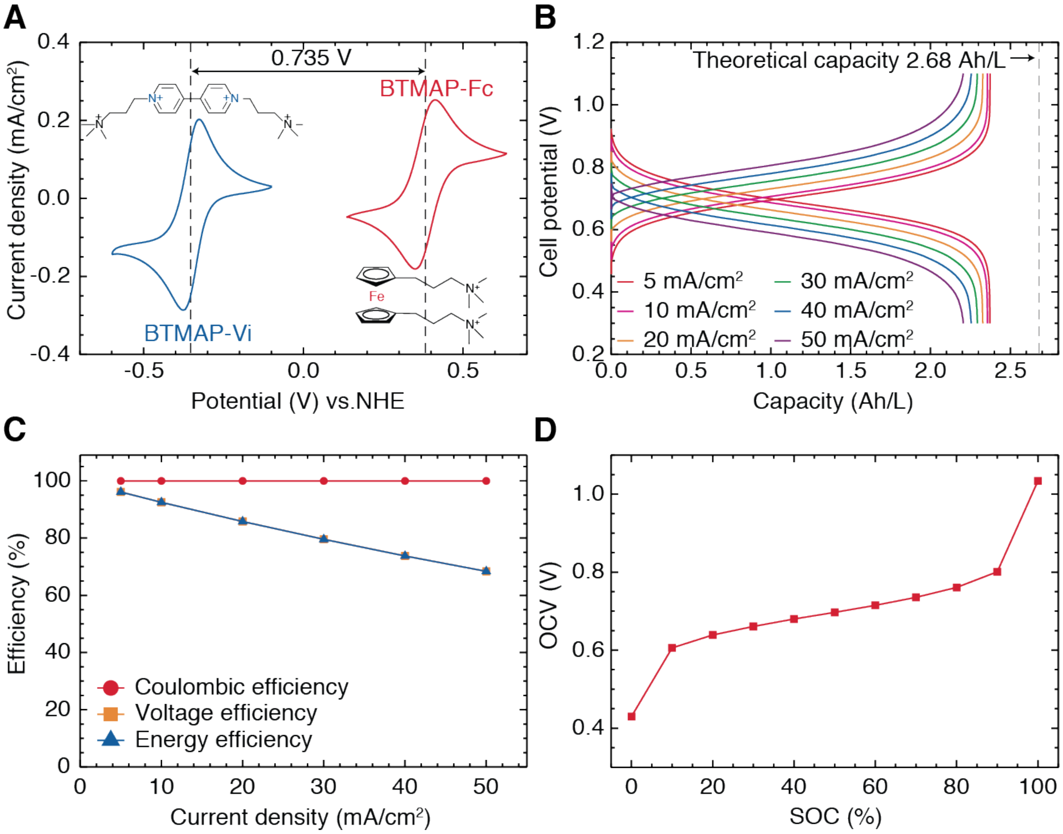

Figure 4.1. Cyclic voltammogram and RFB performance of the BTMAP-Vi and BTMAP-Fc redox couples. a, Cyclic voltammogram of 5.0 mM BTMAP-Fc (red curve) and 5.0 mM BTMAP-Vi (blue curve) in 1.0 M NaCl scanned at 10 mV/s on a glassy carbon electrode, showing a 0.735 V voltage difference. **b**, Representative galvanostatic cycling curves from 5 mA/cm^2 to 50 mA/cm^2 with cut-off voltages of 1.1 V and 0.3 V. **c**, RFB Coulombic efficiency, voltage efficiency and energy efficiency at different galvanostatic cycling current densities. **d**, Measured cell open circuit voltage (OCV) *vs.* state-of-charge (SOC).

To perform bias-free photocharging and on-demand electrochemical discharging of the BTMAP redox couples, we built the SFB device by integrating two carbon felt electrodes and two silicon photoelectrodes in close contact (Figure 4.2a), similar to the "zero-gap" device design commonly seen in RFBs.[38] Such design allows us to switch the function of the device between 3 different modes: RFB mode, solar cell mode and solar recharge mode, and thus fulfill all the requirements for a stand-alone solar electrification system. As illustrated in Figure 4.2b, the two photoelectrodes used in the SFB device were both fabricated by forming internal solid-state *p-n* junction on n-type silicon substrates, but with opposite polarity so that they can be implemented as photoanode (n^+np^+-Si) and photocathode (p^+nn^+-Si), respectively. Solar illumination comes from the n^+ side for photoanode and p^+ side for photocathode in a bifacial fashion. We further deposited a Ti/TiO_2/Pt (5 nm/40 nm/5 nm) layer on the back side the of the photoelectrodes, where solution would be in direct contact, to protect silicon from photocorrosion. Previous reports have shown that TiO_2 protected Si photoelectrodes can be continuously operated for photoelectrolysis of water under extreme pH conditions (such as 1 M $HClO_4$ and 1 M KOH) with good stability.[39,40] Thus this protection could potentially enable practical long term operation of Si based photoelectrodes in neutral electrolytes. Having established the excellent RFB performance with the 0.20 M BTMAP electrolytes, we feed the same electrolytes to SFB device for studying its performance under different operation modes with configurations listed at the bottom of Figure 4.2a. Briefly, in addition to using only the two inert carbon felt electrodes to perform the RFB tests as described above, we can either pair the photoelectrode with carbon felt electrode on the same cell chamber to turn over and regenerate one pair of redox couple and directly produce electricity (solar cell mode); or connect it with the other photoelectrode in series to store converted solar energy as chemical energy by creating an electrochemical bias between the two BTMAP redox couples (solar recharge mode). The detailed discussion on the operation and chemical reactions under different operation modes is presented in Scheme A3.1.

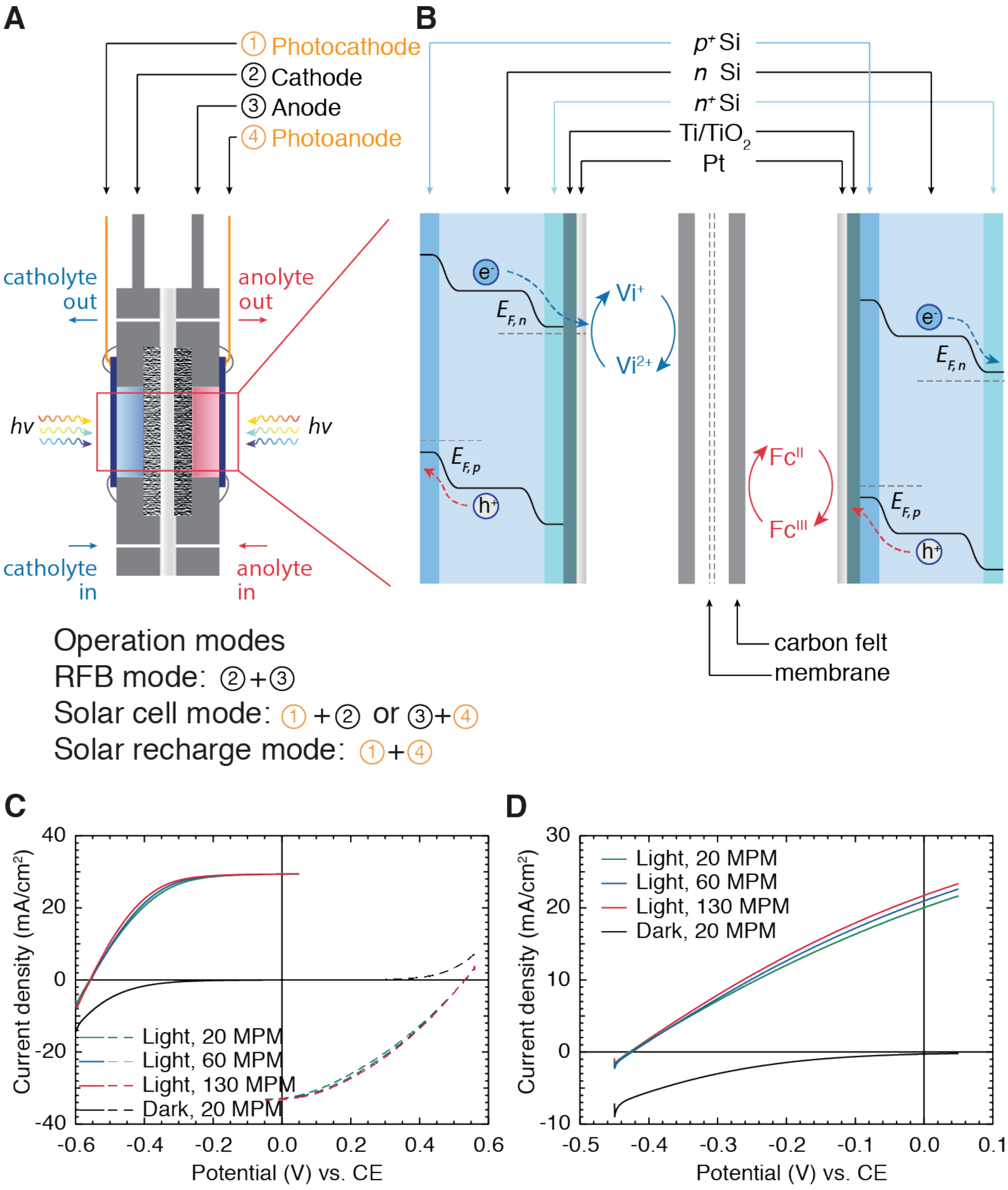

Figure 4.2. Scheme of key components in the SFB, their configurations, and solar performance under different operation modes. a, Schematic cross-section of the SFB, showing two single junction silicon photoeletrodes and two carbon felt inert electrodes, which could be

connected in 3 different modes. **b**, Zoom-in scheme of the center part in the SFB, illustrating the architectures and energy diagrams of the illuminated photoelectrodes in equilibrium with BTMAP-Vi and BTMAP-Fc redox couples. **c**, *J-V* performance of the photoanode (solid curves) and photocathode (dashed curves) in 0.2 M BTMAP electrolytes, measured individually under solar cell mode at different flow rates. **d**, *J-V* performance of photoanode and photocathode connected in series in 0.2 M BTMAP electrolytes, measured under solar recharge mode at different flow rates.

Figure 4.2c shows the current density-voltage (*J-V*) performance of independently characterized photoanode and photocathode configured to solar cell mode with 1-Sun (100 mW/cm^2) simulated solar illumination provided by a quartz tungsten halogen (QTH) lamp or in the dark. To find an optimal electrolyte flow rate for the SFB, we carried out the linear scan voltammetry with three electrolyte flow rates: 20 mL/min (MPM), 60 MPM and 130 MPM. Except for the very slight improvement in fill factor (*FF*) at high flow rates, the solar performance of both photoelectrodes appears to be rather insensitive to electrolyte flow rates within the range we studied. Such results indicate that the "zero-gap" device design can ensure sufficient electrochemical mass transport between photoelectrodes and carbon felt electrodes even at a flow rate as low as 20 MPM. At 20 MPM, the photoanode shows an open circuit voltage (V_{oc}) of 0.559 V and a short circuit current density (J_{sc}) of 29.4 mA/cm^2, and photocathode shows a well matched V_{oc} of 0.532 V and J_{sc} of 32.8 mA/cm^2. The combination of these two photoelectrodes can provide a total V_{oc} of 1.091 V for solar charging the BTMAP SFB device without external bias. We also noticed that, in comparison with the solid-state PV cells fabricated with same type of silicon cells (Figure A3.2), the photoelectrodes measured individually under solar cell mode (at 20 MPM) exhibit reasonably preserved V_{oc} and J_{sc} but noticeable decrease in *FF* (from 64.1% to 51.7% for photoanode and from 69.9% to 38.9% for photocathode), resulting in a lower overall power conversion efficiency for both photoelectrodes (8.49% for photoanode and 6.79% for photocathode). Potentiostatic electrochemical impedance spectroscopy (EIS) was employed to further study the mechanism behind such efficiency loss (Figure A3.3). By comparing and analyzing EIS data of the solid state silicon solar cells and photoelectrodes, we attribute the decrease in *FF* to the uncompensated solution resistance and non-ideal charge extraction process at the semiconductor-liquid interface.

In addition to the *J-V* characterization of individual photoelectrodes measured under solar cell mode, we also investigate the overall solar performance of the SFB device under solar recharge mode by measuring the *J-V* response between photoanode and photocathode (Figure 4.2d). As illustrated in Figure A3.4, the operating current density of SFB can be found at the intersection point of the overlaid *J-V* curves for independently characterized photoanode and photocathode under solar cell mode. J_{sc} under solar recharge mode equals to the operating current density of SFB. The slight increase of J_{sc} under solar recharge mode with increasing flow rates is the cumulative result of aforementioned *FF* dependence of individual photoelectrodes on flow rate, as the intersection point is on the high curvature region of these *J-V* curves. After confirming that high flow rates would not bring significant benefits for SFB devices, 20 MPM was selected to perform all studies described hereafter.

The main function of SFBs is capturing and storing solar energy when the sun is shining, and delivering electrical energy on demand. This calls for the cooperation between the solar recharge mode and the RFB mode. In order to demonstrate that the SFB device can be stably operated between these two modes, we performed a long term cycling test on this device using a synchronized dual channel potentiostat to continuously monitor solar recharge photocurrent and cell potential. Each cycle was started with 1 hour of bias-free solar charging by connecting the photoanode and photocathode in series, followed by a galvanostatic discharging step at -5 mA/cm^2 (a current of -20 mA, based on a carbon felt electrode area of 4 cm^2) until a cutoff potential of 0.3 V was reached. Representative device cycling behavior recorded during the first five cycles of the long term cycling test is shown in Figure 4.3a. The red curve is the cell potential profile measured between the two carbon felt electrodes. Although this curve resembles the typical voltage-time (V-t) profile of common RFBs, it has a subtle, yet conceptually important difference. Because no external current was provided by the potentiostat during the solar charging process, the rising cell potential recorded during this process represents only the open circuit potential (E_{oc}, this is the open circuit potential of the RFB component and should be distinguished from V_{oc} of the photoelectrode) of the SFB without any overpotential, while the descending potential recorded during galvanostatic discharging step can be interpreted as $E_{oc} - \eta$ (η is the overall overpotential), as the case for RFBs. The solar recharge current density (blue curve in Figure 4.3a) started at ~24 mA/cm^2 and gradually decreased to ~15 mA/cm^2 at the end of the 1-h charging cycle due to the increase of cell potential, resulting in an average photocurrent density of 18.5 mA/cm^2 (a current of 22.9 mA, based on an average photoelectrode area of 1.239 cm^2). With the relatively high total photovoltage (~1.1 V) generated by the photoelectrodes, the SFB can effectively utilize most of its storage capacity and reach a near unity state-of-charge (SOC) after being charged for 1 h. The following discharging cycle (cycle 1 in Figure 4.3b) can deliver a volumetric capacity of 2.27 Ah/L (energy density of 1.52 Wh/L, calculated based on the total volume of both electrolytes), corresponding to 91.5% of the total potentiostatically determined capacity. Based on the solubility of BTMAP redox couples and RFB study in the previous work, the theoretical capacity for the SFB device is 25 Ah/L when 1.9 M of BTMAP redox couples are used.[36]

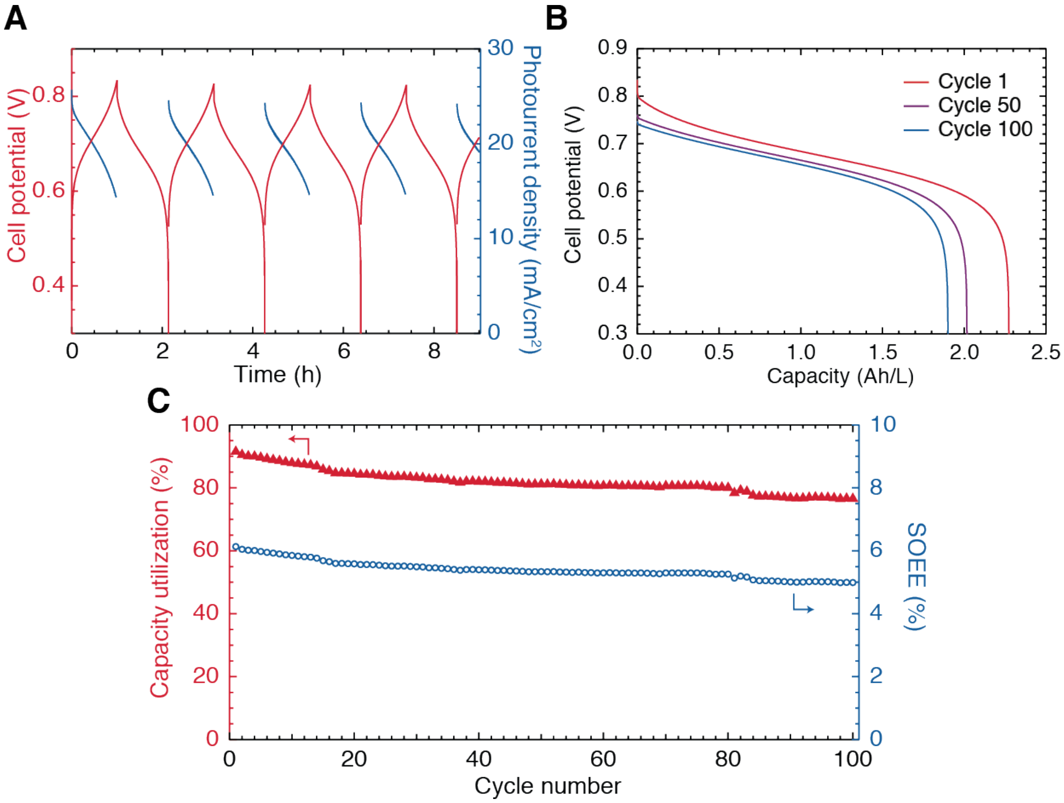

Figure 4.3. **Cycling performance of the integrated SFB device over 100 cycles. a**, Representative device cycling behavior showing cell potential between cathode and anode (red curves), as well as the photocurrent density delivered by the photoelectrodes connected in series (blue curves), recorded between the first and fifth cycles. **b**, Representative potential-capacity profiles during galvanostatic discharging process at cycle 1, 50 and 100. The capacity shown here represents the effectively utilized capacity at each cycle after solar charging. **c**, Charging and discharging capacity utilization (normalized on the basis of the potentiostatically determined capacity before cycling) and solar-to-output electricity efficiency (*SOEE*), showing a stable cycling performance over 200 hours (100 cycles). Each cycle was started with a 1 hour bias-free solar charging process followed by a galvanostatic discharging step at - 20 mA until reaching the cutoff potential (0.3 V).

Figure 4.3c shows the SFB can be stably cycled between solar recharge mode and RFB mode over 100 cycles (>200 hours) and maintain an average capacity utilization rate of 81.9%. In comparison, the continuous operation durations for all previous SFB demonstrations are less than 50 hours.[6] The round trip energy efficiency of the SFB was evaluated by the solar-to-output electricity efficiency (*SOEE*) as defined by the following equation,

$$SOEE = \frac{E_{electrical,out}}{E_{illumination}} = \frac{\int I_{out}V_{out}dt}{\int SAdt}, \tag{1}$$

where $E_{electrical,out}$ is the output electrical energy delivered on demand after storage and $E_{illumination}$ is the input solar energy (calculated based on the total area of both photoelectrodes). The SFB maintained a high *SOEE* during the long term cycling test with an average of 5.4%, which is an over 2-fold increase in comparison to that of the previously demonstrated SFB using the same silicon photoelectrode design (1.7%).[12] In addition, both Coulombic and voltage efficiency of the SFB were higher than 90% throughout the cycling test (Figure A3.5). Although Figure 4.3c shows slow decay in the capacity utilization rate and *SOEE* for the SFB, detailed device characterization after the cycling test (Figure A3.6) suggests that such decay could be avoided with a little additional engineering effort. This decay was mainly caused by the decrease of illumination intensity and accumulation of bubbles in the small electrolyte pocket between the photoelectrodes and carbon felt electrodes. These bubbles can block the flow chambers and result in a decrease of effective electrolyte-contacting surface areas for both photoelectrodes and carbon felt electrodes. For both photoanode and photocathode, their J_{sc} under solar cell mode can be significantly increased after replacing the light bulb and recalibrating the illumination intensity of the QTH solar simulator. The decay in photocurrent was also responsible for the decreased capacity utilization rate shown in Figure 4.3b and 4.3c because the solar charging process was set to a constant time (1 hour). Additionally, by temporarily increasing the flow rate to 130 MPM to flush out the bubbles accumulated in the flow chambers, we were able to improve the solar performance of the photoelectrodes and almost fully recover to the original level before the cycling test. Fortunately, bubble accumulation is a minor engineering issue that can be easily solved with some modifications in flow management and therefore will not affect the true stability of the SFB devices (Figure A3.7). In addition, the issue of bubble accumulation can also be addressed by using a well-designed flow channel structure to avoid the need for flushing. In fact, the stability of the photoelectrodes was so good that we actually disassembled and reassembled the SFB devices several times for various tests using the same pair of photoelectrodes. The total operation time of these photoelectrodes was well over 400 hours.

The long lifetime of the SFB device is enabled by the combination of robust photoelectrodes, stable redox flow battery chemistry, and the careful design of the SFB. From the 200 hours cycling test, we did not see an unrecoverable SOEE loss. Based on previous studies on TiO_2 protected Si photoelectrodes[41] and BTMAP RFBs,[36] we think the stability of the photoelectrodes could eventually limit the overall lifetime of the SFB device beyond the thousands of hours in typical lab test settings.

Furthermore, compared to most SFB devices previously demonstrated that could only access a small portion of the total capacity,[6] the SFB demonstrated here sets a new benchmark for capacity utilization rate, which is an essential quality for practical applications. Being able to solar charge the SFB device to a near unity SOC also brings out another unique aspect of the integrated solar energy conversion and electrochemical storage devices. Unlike conventional PEC devices dealing with redox reactions with fixed equilibrium potentials, such as solar water electrolysis[28,42] and liquid junction solar cells,[43,44] SFBs and other similar integrated devices store energy by building up its internal electrochemical potential (E_{oc} increase in Figure 4.3a).[4] As illustrated in

Figure 4.4a, an increase of E_{oc} would result in a shift of the operating point on the *I-V* curve of photoelectrodes and consequently cause a change in *SOEE*. To quantify the relationship between *SOEE* and E_{oc}, we derive and propose a modified figure of merit, instantaneous *SOEE* ($SOEE_{ins}$), from Equation (1):

$$SOEE_{ins} = \frac{P_{electrical,out}}{P_{illumination}} \approx \frac{I_{photo}E_{oc} \times CE \times VE}{SA}, \tag{2}$$

where $P_{electrical,out}$ is the discharging power, which is estimated by using charging power $I_{photo}E_{oc}$ times the internal power conversion efficiency of SFB; $P_{illumination}$ is the illumination power provided by the solar simulator. The detailed derivation and explanation can be found in the Supporting Information. $SOEE_{ins}$ can be simply interpreted as the external power conversion efficiency of the SFB device at certain E_{oc}. A representative $SOEE_{ins}$ curve with respect to E_{oc} is presented in Figure 4.4b, which is numerically calculated from the first solar charging cycle in Figure 4.3a with a constant time interval of 60s using cell potential and photocurrent data points that are nearest to the desired time. The $SOEE_{ins}$ increases at the beginning and then decreases with E_{oc} increasing, showing a maximum of 6.51% at 0.663 V and an average of 6.15% that is essentially the same as the *SOEE* value (6.13%) calculated using Equation 1. By plotting E_{oc} with respect to SOC, we can also find that the highest $SOEE_{ins}$ was reached at a SOC of 22.6%. The shaded area in Figure 4.4b shows the E_{oc} range between 10% SOC and 90% SOC (an example of E_{oc} *vs.* SOC for current BTMAP redox couples is plotted in Figure 4.1d), which represents the typical operation window for practical SFBs or RFBs. Since the overall *SOEE* of a SFB device is close to the average $SOEE_{ins}$ value within the shaded E_{oc} window, the highest *SOEE* with the same photoelectrodes should be achieved under the hypothetical blue area. With this method, we can derive the best matched E_{cell} for SFBs to extract the highest power conversion efficiency out of certain photoelectrodes.

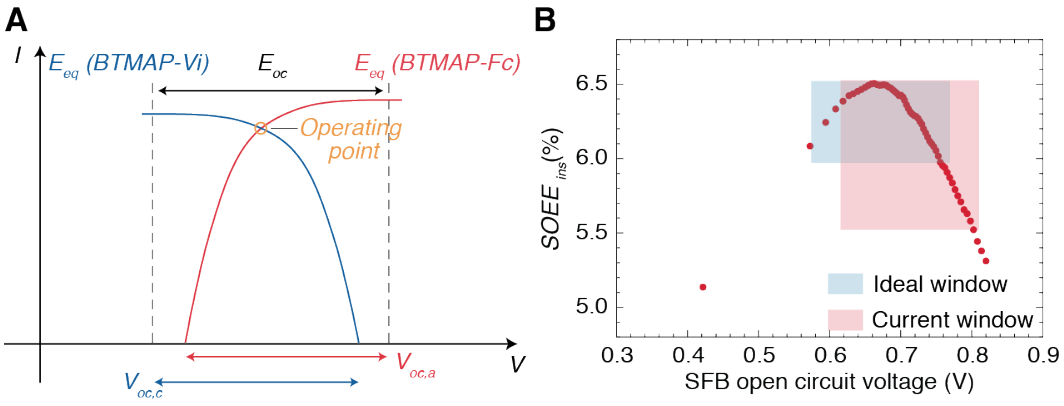

Figure 4.4. Using instantaneous *SOEE* and its relationship with E_{oc} to optimize SOEE. a, Overlaid hypothetical *J*-*V* curves of photoanode and photocathode. The intersection point of the red and blue curves is influenced by the RFB voltage. The instantaneous *SOEE* is determined by the power at the operating point. **b**, Representative instantaneous *SOEE* as a function of E_{oc} calculated from the first photocharging cycle of the long term SFB cycling test shown in Figure 4.3c. The maximum instantaneous *SOEE* (6.51%) was achieved at a E_{oc} of 0.663 V (22.6% SOC). The semi-transparent shaded areas represent the E_{oc} range between 10% SOC and 90% SOC for a SFB with the current BTMAP redox couples (pink) and hypothetical ideal redox couples that have a formal potential difference of 0.663V (blue).

Note that for given photoelectrodes, $SOEE_{ins}$ is only determined by E_{oc}, so the $SOEE_{ins}$-E_{oc} relationship for the same photoelectrodes should remain unchanged no matter which redox couples are used. Thus, the $SOEE_{ins}$-E_{oc} curve can serve as a better guide for tuning the operating $SOEE_{ins}$ window of the SFB with different redox couples in order to optimize the average *SOEE*. For example, for the *p/n* Si photoelectrodes used in this study, the best matched E_{cell} should be 0.663 V. As mentioned above, although the same *p/n* Si photoelectrode design was used, the SFB studied here can deliver a *SOEE* over 3 times that of a previous SFB demonstration.[12] Such enhancement can be readily explained with the knowledge of the $SOEE_{ins}$-E_{oc} relationship for these *p/n* Si photoelectrodes: E_{cell} for the present SFB (0.735 V) is much closer to the optimized E_{cell} (0.663 V) than that for the previous demonstration (0.461 V).

Although previous report suggested that the SOC dependency of *SOEE* can be studied by first charging the SFB to desired SOCs and then measuring solar response of the photoelectrode (a set of data using this method is presented in Figure A3.8),[15] the introduction of $SOEE_{ins}$ makes this analysis much easier and more reliable, since the $SOEE_{ins}$-SOC relationship can be directly derived from real time SFB cycling data without additional tests and undesired SOC disturbance. More importantly, harnessing the $SOEE_{ins}$-E_{oc} relationship (such as Figure 4.4b), the development of the solar energy conversion and electrochemical energy storage components in SFBs can be decoupled to allow independent optimization of these components. The in-depth study on the $SOEE_{ins}$ unveiled a more flexible design principle for SFBs that can be universally applied to other SFB devices to extract the most solar energy conversion efficiencies out of given solar cells. Such new understanding can stimulate the development of designer solar materials[27,28,45] and redox species[33,46-49] specifically for SFBs.

This work demonstrates that by taking advantage of stable redox couples in low corrosiveness neutral pH electrolytes and well protected Si photoelectrodes, the lifetime of SFBs can be greatly extended. The extensive studies on Si based photoelectrodes for PEC energy conversion applications over the last few decades[50,51] have led to development and demonstration of successful protection strategies for Si based photoelectrodes in contact with aqueous electrolytes.[39,40] Indeed, a recent report has shown that np^+-Si/TiO_2/$NiCrO_x$ can drive PEC water oxidation in 1.0 M KOH continuously over 3 months.[41] This bodes well for SFBs, because the simplified photoelectrode structure without catalysts in SFBs and the less harsh neutral pH condition are expected to further extend the lifetime of Si photoelectrodes. Moreover, as a small bandgap semiconductor (1.1 eV), silicon shows great promises as the bottom layer material for tandem junction solar cells, such as a-Si/μc-Si (amorphous Si/microcrystalline Si) tandem cell[52] and III-V/Si tandem cell,[53] which features not only higher efficiency but also larger photovoltage. The ongoing development of tandem junction PV cell technologies has led to the hope that fabricating additional junctions on single junction Si bottom substrate could be a more cost-effective strategy compared to single junction cells. The decoupled light absorption/solution contact photoelectrode design used in our SFBs (Figure 4.2b) ensures that these emerging tandem junction cells can be readily adopted into the current SFB design frame to boost its *SOEE*. In addition, these tandem junction solar cells demand specifically designed redox couples to realize a good voltage match, which can be rationalized under the guidance of $SOEE_{ins}$-E_{oc} relationship.

4.4 Conclusions

The SFB device studied in this work sets new records for both continuous operation time (>200 h) and capacity utilization rate (>80%). The successful application of the voltage matching principle yields a significantly boosted *SOEE* from 1.7% to 5.4% using the same silicon photoelectrode design. In addition, the high capacity utilization rate unveiled the unique SOC dependence of the *SOEE* for SFBs that differentiates SFBs from other conventional PEC regenerative or electrolysis devices. The newly introduced instantaneous solar-to-output electricity efficiency ($SOEE_{ins}$) and the $SOEE_{ins}$-E_{oc} curve can provide guidance toward more efficient SFB device design with better working voltage match between photoelectrodes and redox couples. Building on highly stable BTMAP redox couples and Si photoelectrodes, the long lifetime SFB demonstrated here sets an important milestone to move SFB research into a more practical arena.

4.5 Methods

4.5.1 Electrochemical measurements

Cyclic voltammetry (CV) (Figure 4.1a) and steady state linear sweep voltammetry (LSV) measurements (Figure a3.1) were conducted using a Bio-Logic SP-200 potentiostat. A 3 mm diameter glassy carbon disk electrode (MF-2012, BASi for CV and MF-2066 for LSV) was used as the working electrode, which was polished using 0.3 μm and 0.05 μm alumina slurry to mirror polish and washed with deionized water (Milli-Q, 18.2 MΩ cm) and methanol before each test. The glassy carbon electrode was further cleaned electrochemically in 1 M Na_2SO_4 solution (with 1 mM potassium ferrocyanide as internal reference) by swiping potential between -1.0 V and 1.5 V *vs.* reference electrode at 100 mV/s until the peak separation of ferrocyanide/ferricyanide redox couple reaches 60 mV. A custom-made Pt coil electrode (0.5 mm diameter) and a saturated calomel electrode (SCE, CH Instruments) were used as the counter and reference electrode, respectively. The electrolyte consisted of 5 mM of either BTMAP-Fc or BTMAP-Vi and 1.0 M NaCl and was purged with argon before measurements. CV was scanned at a scan rate of 10 mV/s and the formal potential of the redox couples (-0.353 V for BTMAP-Vi and 0.382 V for BTMAP-Fc) were estimated by calculating the average potential between anodic peak and cathodic peak in the CV curves. The uncompensated resistance was determined by measuring the high frequency impendence at 100 kHz, which was then used to compensate the CV curves at an 85% compensation level using EC-Lab software. Electrochemical kinetics of the two redox couples was studied using a rotating disk electrode (BASi, RDE-2) at different rotating speed (Figure A3.1a-b). LSV was scanned at a scan rate of 10 mV/s. The diffusion coefficient (D) of the oxidized BTMAP-Vi and reduced BTMAP-Fc was calculated using Levich equation, $i_l = 0.62nFAD^{2/3}\omega^{1/2}\upsilon^{-1/6}C$, where n = 1, F = 96,485 C/mol, A = 0.0707 cm^2, C = 5.0 mM, υ =

0.9380×10^{-2} cm^2/s (kinematic viscosity of 1.0 M NaCl at 298 K) and i_l determined at an absolute overpotential ($|\eta|$) of 200 mV (Figure A3.1c-d). Koutecký–Levich plots ($1/i$ *vs.* $\omega^{-1/2}$) were used to determine the kinetic currents (i_k) at different overpotentials by extrapolating the fitted $1/i$ *vs.* $\omega^{-1/2}$ lines to $\omega^{-1/2} = 0$. The standard rate constants (k_0) and transfer coefficient (α, reduction reaction) were calculated using the Butler-Volmer equation by linearly fitting a Tafel plot (log i_k *vs.* η) between an $|\eta|$ region of 40-80 mV (Figure A3.1e-f). The RDE experiments were performed 3 times for each redox couple to obtain the average value for D, k_0 and α.

4.5.2 Fabrication of RFB and integrated SFB device

The RFB and SFB measurements were carried out in a custom-made zero-gap device, similar to what was reported previously.[18] Graphite plates (1/8-inch thickness, Tokai Carbon or MWI) with a 20 × 20 × 1.2 mm pocket were used as current collector for RFB devices. Modified current collectors with additional 15 × 15 mm clearance window at the center of the square pocket were used for SFB devices to allow direct contact between photoelectrode and liquid electrolyte. 4 cm^2 graphite felt electrodes (GFD 3 EA, SIGRACELL®) were pre-treated at 400 ^{o}C in air for 6 h before being used on both sides of the cell. 25 × 25 mm Selemion DSV (Ashahi Glass Co., Ltd.,) was presoaked in 1.0 M NaCl for more than 24 h before it was used as an anion-exchange membrane. The cell was assembled with four pieces of die cut PTFE sheets (0.04-inch thickness) as gaskets and tightened with eight #10-24 bolts torqued to 4.0 Nm. The electrolytes were pumped through the flow channels by a peristaltic pump (Cole-Parmer Masterflex L/S) via PharMed BPT tubing. 10 mL custom made glass vial with two 4 mm OD electrolyte inlet/out arms were used as electrolyte reservoir. All RFB and SFB measurements were carried out in a custom modified N_2 flush box (Terra Universal) with continuous N_2 flushing.

4.5.3 General RFB measurements

5.0 mL solution of 0.2 M bis((3-trimethylammonio)propyl)ferrocene dichloride (BTMAP-Fc) in 1.0 M NaCl and 5.0 mL solution of 0.2 M bis(3-trimethylammonio)propyl viologen tetrachloride (BTMAP-Vi) in 1.0 M NaCl were used as anolyte and catholyte, respectively. Both BTMAP-Fc and BTMAP-Vi were synthesized following the method described in the previous report[36] or purchased from TCI America. The electrolyte flow rate was controlled at 20 mL/min for all RFB measurements.

The RFB cycling and polarization performance tests were carried out using a Bio-Logic BP-300 potentiostat. Galvanostatic cycling tests were performed by charging and discharging the device at a desired constant current density with 0.3 V and 1.1 V as the bottom and top potential limits, respectively. A 10s rest at open circuit voltage (*OCV*) was employed between each half cycles. The potentiostatic capacity of the RFB was determined by galvanostatic cycling of the RFB as described above followed by a potential hold at cut-off potentials until the current density reached 1 mA/cm^2. To measure *OCV* of the RFB at different states of charge (SOCs), the battery was galvanostatically charged or discharged with a 10% SOC step and then rested for 2 min to measure the OCV. The 0% SOC and 100% SOC were accessed by the galvnostatic-potentiostatic cycling method described above until the current density reached 1 mA/cm^2 at 0.3 V and 1.1 V, respectively. In the cell polarization characterization, a LSV scan was performed at a scan rate of 100 mV/s. To avoid the disturbance of SOC by LSV scans, the RFB was completely discharged to 0% SOC and then recharged to the specific SOC before each LSV was measured. All the SOCs mentioned in this study were calculated based on potentiostatic capacity. Potentiostatic electrochemical impedance spectroscopy (EIS) measurement of the RFB was performed at 0%

SOC, 0.3 V bias with a voltage offset of 10 mV, and frequencies ranging from 100 kHz to 1 Hz (Figure A3.6d).

4.5.4 Fabrication of photoelectrode assembly for the integrated SFB device

The fabrication of n^+np^+ and p^+nn^+ silicon solar cells with Ti/TiO$_2$/Pt (5 nm/40 nm/5 nm) protection layers followed the method previously reported.[12] The photoelectrode assembly for the integrated SFB device characterization was fabricated by affixing a n^+np^+ (for photoanode) or a p^+nn^+ (for photocathode) silicon cell onto a custom-made graphite current collector (described in the SFB device section) by epoxy resin (Hysol 9460) to cover the window of the current collector. The back side of the silicon cell (p^+ side for the n^+np^+ cell or n^+ side for the p^+nn^+ cell) was only physically attached to the current collector without forming an electrical contact. The electrolyte can directly contact the back side of the silicon cell through the window of the current collector and harvest photogenerated charges during SFB device operation in solar recharge mode and solar cell mode. The ohmic contact to photoelectrode was made by attaching a copper foil onto the front side of the cell (n^+ side for the n^+np^+ cell or p^+ side for the p^+nn^+ cell) with Ga/In eutectic mixture (Sigma Aldrich) and fixed with silver paint (Ted Pella, PELCO colloidal silver). The ohmic contact area was sealed by epoxy resin. The geometric area of the exposed silicon cell was determined using calibrated digital images and Adobe Photoshop, which was usually between 1.10 cm^2 and 1.30 cm^2.

4.5.5 Solid state and PEC characterization of silicon photoelectrodes

Solid state *J-V* performance of the n^+np^+ and p^+nn^+ silicon cells were measured in a two-electrode configuration by making ohmic contact to the front and back side of the cell. The LSV data was collected using a Bio-Logic SP-200 potentiostat under 1 Sun (100 mW/cm^2) of AM 1.5 G simulated illumination by a Newport Model 91191 Xenon arc lamp solar simulator with a scan rate of 100 mV/s. EIS measurements were performed at V_{oc} of the solid state cells under 1 Sun of simulated solar illumination with a voltage offset of 10 mV, and frequencies ranging from 1 MHz to 1 Hz. A Si photodiode (Thorlabs) was used to calibrate the illumination intensity of the AM 1.5G solar simulator to 100 mW/cm^2.

The PEC characteristics of the silicon photoelectrodes were measured in the assembled SFB device with a Bio-Logic BP-300 potentiostat under 1 Sun (100 mW/cm^2) of simulated solar illumination. The illumination was provided by a Newport Model 67011 quartz tungsten halogen (QTH) light source with a branched flexible silica light guild (Taiopto Mems International Co., LTD.) fed through a N_2 flush box and collimated by an OSL2COL convex lens collimation tube (Thorlabs). To calibrate the QTH solar simulator, short circuit current (I_{sc}) of a solid-state p^+nn^+ Si solar cell (~ 1.1 cm^2) was first measured under 1 Sun of AM1.5 G simulated solar light using the Newport 91191 solar simulator, then the QTH solar simulator was calibrated to generate the same I_{sc} using the same solid-state p^+nn^+ Si solar cell. The PEC measurements were performed in a two-electrode configuration under both solar cell mode and solar recharge mode (Figure 4.2c-d) with the same electrolytes used in the RFB test (0.2 M BTMAP-Fc as anolyte and 0.2 M BTMAP-Vi as catholyte, both with 1.0 M NaCl as supporting electrolyte). To study the influence of SOC on the performance of photoelectrodes, the PEC measurements were carried out at different SOCs by galvanostatically charging the SFB to the desired SOC from 0% SOC. The PEC measurements at 50% SOC were also repeated at different flow rates (Figure 4.2c-d) to investigate the relationship between mass transport and PEC performance of the photoelectrode. A relatively slow flow rate (20 mL/min) was used for all the other PEC measurements because the PEC performance is insensitive to the flow rate. All LSV curves were recorded at a scan rate of 10 mV/s without correcting for any uncompensated resistance losses. EIS measurements of the individual photoelectrodes were performed under solar cell mode at 50% SOC with a flow rate of 20 MPM. The measurements were performed at V_{oc} of the photoelectrodes under 1 Sun of simulated solar illumination (QTH lamp) with a voltage offset of 10 mV, and frequencies ranging from 100 kHz to 1 Hz.

4.5.6 Integrated SFB device characterization

The integrated SFB device was assembled with a photoanode assembly, a photocathode assembly, and all the other components the same as the RFB device described in the previous section. The electrolyte flow rate was controlled at 20 mL/min for all the SFB cycling tests.

To characterize the charging-discharging behaviors of the integrated SFB devices, a Bio-Logic BP-300 bi-potentiostat was used: channel 1 was configured as solar recharge mode to monitor the photocurrent; channel 2 was configured as RFB mode to monitor the potential difference between the two carbon felt electrodes (the connections for different modes are illustrated in Figure 4.2a). During the solar recharging process, silicon photoanodes and photocathodes were illuminated by the QTH light source/silica light guild at 1 Sun from both sides of the SFB without applying any external bias. Photocharging time was adjusted during the first cycle to make sure >90% of the total capacity can be accessed. During the discharging process, the illumination was blocked by an analog signal regulated beam shutter, and the integrated device was operated as a normal RFB with a discharging current of -20 mA applied by channel 2 until the cell potential reached 0.3 V. The discharging current was selected to match the average solar recharging current. The two potentiostat channels and a beam shutter controller (custom made Arduino based device) were synchronized and controlled by channel 2 with its trigger out/analog out function to enable fully automated SFB device cycling test and ensure stable long-term measurement. The total capacity of the SFB device was also measured by galvanostatic-potentiostatic method before and after SFB cycling test to confirm no significant amount of capacity was lost during cycling.

4.5.7 Calculation of SOEE and SOEE$_{ins}$

In order to quantitatively evaluate the solar conversion and energy storage efficiency of the integrated SFB device, a specific figure of merit should be considered: solar-to-output electricity efficiency (SOEE), which is defined by the ratio of the usable electrical energy delivered by the integrated SFB device ($E_{electrical,out}$) over the total solar energy input ($E_{illumination}$). The *SOEE* can be calculated using equation 1:[12]

$$SOEE = \frac{E_{electrical,out}}{E_{illumination}} = \frac{\int I_{out} V_{out} dt}{\int SAdt}, \tag{1}$$

where I_{out} is the output (discharging) current, V_{out} is the output voltage, S is the total incident solar irradiance, which is provided by the QTH light source at 100 mW/cm^2, and A is the total illumination area of photoanode and photocathode. Note that this *SOEE* is the *round-trip efficiency* of the delivered electrical energy at any time on demand over the original solar energy input.

Before going into details about instantaneous *SOEE*, we should firstly examine the break-down of the energy conversion processes of the SFB device. From solar energy input to electrical energy output, the SFB device need to perform 3 energy conversion steps: input solar energy to electrical energy, electrical energy to chemical energy, and chemical energy to output electrical energy, as summarized in the following equation:

$$SOEE = \frac{E_{electrical,out}}{E_{illumination}} = \frac{E_{electrical,in}}{E_{illumination}} \times \frac{E_{chemical}}{E_{electrical,in}} \times \frac{E_{electrical,out}}{E_{chemical}}. \tag{2}$$

Because the chemical energy of redox couples, $E_{chemical}$, is difficult to quantify, we can rewrite Equation 3 as follows:

$$SOEE = \frac{E_{electrical,out}}{E_{illumination}} = \frac{E_{electrical,in}}{E_{illumination}} \times \frac{E_{electrical,out}}{E_{electrical,in}}, \tag{3}$$

where $\frac{E_{electrical,in}}{E_{illumination}}$ is the efficiency for the PEC solar energy conversion component and $\frac{E_{electrical,out}}{E_{electrical,in}}$ is the efficiency for the electrochemical energy storage component. Because storing and releasing electrical energy electrochemically only involves turning over redox couples inside the SFB device, the isolated term, $\frac{E_{electrical,out}}{E_{electrical,in}}$, can be seen as the "internal efficiency" of SFB and accordingly *SOEE* is the external efficiency of SFB. Note that this internal efficiency of SFB is completely different from the internal quantum efficiency (IQE) commonly used to evaluate solar cells.

The hypothetical overlaid *J-V* curves of photoelectrodes shown in Figure 4.4a illustrates that the operating point for the integrated SFB device could be significantly influenced by the working voltage matching between the photoelectrode and the SFB cell potential. Even though the photovoltage generated by the internal solid-state *p-n* junction of the photoelectrode is constant, the SFB cell potential may vary greatly during its charging/discharging process, resulting in a considerable *SOEE* change at different SOCs. To quantitatively analyze such *SOEE* change at different charging/discharging state of the SFB, an instantaneous *SOEE* can be defined and estimated using the following equation:

$$SOEE_{ins} = \frac{P_{electrical,out}}{P_{illumination}} \approx \frac{P_{electrical,in} \times PE_{internal}}{P_{illumination}} = \frac{I_{photo}E_{oc} \times PE_{internal}}{SA} \approx \frac{I_{photo}E_{oc} \times CE \times VE}{SA},$$

where $P_{electrical,in}$, $P_{eletrical,out}$ and $P_{illumination}$ are the electrical charging power of the SFB, electrical discharging power of the SFB and illumination power provided by the solar simulator; $PE_{internal}$ is internal power conversion efficiency of the SFB, which can be estimated as the arithmetic product of Coulombic efficiency (*CE*) and voltage efficiency (*VE*) of the SFB; I_{photo} is photocurrent density provided by the photoelectrodes during solar recharging process and E_{oc} is the corresponding cell potential measured at the same time as I_{photo}. An example of $SOEE_{ins}$ *vs.* E_{oc} is plotted in Figure 4B.

4.6 References

1. Yang, Z. G. *et al.* Electrochemical Energy Storage for Green Grid. *Chem. Rev.* **111**, 3577-3613 (2011).

2. Alotto, P., Guarnieri, M. & Moro, F. Redox flow batteries for the storage of renewable energy: A review. *Renew. Sust. Energ. Rev.* **29**, 325-335 (2014).

3. Soloveichik, G. L. Flow Batteries: Current Status and Trends. *Chem. Rev.* **115**, 11533-11558 (2015).

4. Gurung, A. & Qiao, Q. Q. Solar Charging Batteries: Advances, Challenges, and Opportunities. *Joule* **2**, 1217-1230 (2018).

5. Luo, B., Ye, D. & Wang, L. Recent Progress on Integrated Energy Conversion and Storage Systems. *Adv. Sci.* **488**, 1700104-1700115 (2017).

6. Wedege, K., Bae, D., Smith, W. A., Mendes, A. & Bentien, A. Solar Redox Flow Batteries with Organic Redox Couples in Aqueous Electrolytes: A Minireview. *J. Phys. Chem. C* **122**, 25729-25740 (2018).

7. Gurung, A. *et al.* Highly Efficient Perovskite Solar Cell Photocharging of Lithium Ion Battery Using DC-DC Booster. *Adv. Energy. Mater.* **7**, 1602105 (2017).

8. Hodes, G., Manassen, J. & Cahen, D. Photoelectrochemical energy conversion and storage using polycrystalline chalcogenide electrodes. *Nature* **261**, 403-404 (1976).

9. Jin, S. What Else Can Photoelectrochemical Solar Energy Conversion Do Besides Water Splitting and CO2 Reduction? *ACS Energy Lett.* **3**, 2610-2612 (2018).

10. Yu, M. *et al.* Solar-powered electrochemical energy storage: An alternative to solar fuels. *J. Mater. Chem. A* **4**, 2766-2782 (2016).

11. Yu, M. *et al.* Aqueous lithium-iodine solar flow battery for the simultaneous conversion and storage of solar energy. *J. Am. Chem. Soc.* **137**, 8332-8335 (2015).

12. Li, W. *et al.* Integrated photoelectrochemical solar energy conversion and organic redox flow battery devices. *Angew. Chem. Int. Ed.* **55**, 13104-13108 (2016).

13. Liao, S. *et al.* Integrating a dual-silicon photoelectrochemical cell into a redox flow battery for unassisted photocharging. *Nat. Commun.* **7**, 11474-11478 (2016).

14. Wedege, K., Azevedo, J., Khataee, A., Bentien, A. & Mendes, A. Direct solar charging of an organic-inorganic, stable, and aqueous alkaline redox flow battery with a hematite photoanode. *Angew. Chem. Int. Ed.* **55**, 7142-7147 (2016).

15. Wedege, K. *et al.* Unbiased, complete solar charging of a neutral flow battery by a single Si photocathode. *RSC Adv.* **8**, 6331-6340 (2018).

16. Zhou, Y. *et al.* Efficient Solar Energy Harvesting and Storage through a Robust Photocatalyst Driving Reversible Redox Reactions. *Adv. Mater.* **103**, 1802294-1802297 (2018).

17. Cheng, Q. *et al.* Photorechargeable high voltage redox battery enabled by Ta_3N_5 and GaN/Si dual-photoelectrode. *Adv. Mater.* **351**, 1700312-1700318 (2017).

18. Li, W., Fu, H.-C., Zhao, Y., He, J.-H. & Jin, S. 14.1% Efficient Monolithically Integrated Solar Flow Battery. *Chem* **4**, 2644-2657 (2018).

19. Horowitz, K. A. W., Remo, T., Smith, B. & Ptak, A. A Techno-Economic Analysis and Cost Reduction Roadmap for III-V Solar Cells. *National Renewable Energy Laboratory* https://www.nrel.gov/docs/fy19osti/72103.pdf (2018).

20. Ding, Y., Zhang, C., Zhang, L., Zhou, Y. & Yu, G. Molecular engineering of organic electroactive materials for redox flow batteries. *Chem. Soc. Rev.* **111**, 3577-3535 (2017).

21. Wei, X. *et al.* Materials and Systems for Organic Redox Flow Batteries: Status and Challenges. *ACS Energy Lett.* **2**, 2187-2204 (2017).

22. Daniel, T. *et al.* Theoretical and Experimental Investigation of the Stability Limits of Quinones in Aqueous Media: Implications for Organic Aqueous Redox Flow Batteries. (2018).

23. Goulet, M. A. & Aziz, M. J. Flow Battery Molecular Reactant Stability Determined by Symmetric Cell Cycling Methods. *J. Electrochem. Soc.* **165**, A1466-A1477 (2018).

24. Tabor, D. P. *et al.* Mapping the frontiers of quinone stability in aqueous media: implications for organic aqueous redox flow batteries. *J. Mater. Chem. A* **7**, 12833-12841 (2019).

25. Yang, B., Hoober-Burkhardt, L., Wang, F., Surya Prakash, G. K. & Narayanan, S. R. An Inexpensive Aqueous Flow Battery for Large-Scale Electrical Energy Storage Based on Water-Soluble Organic Redox Couples. *J. Electrochem. Soc.* **161**, A1371-A1380 (2014).

26. Hoober-Burkhardt, L. *et al.* A New Michael-Reaction-Resistant Benzoquinone for Aqueous Organic Redox Flow Batteries. *J. Electrochem. Soc.* **164**, A600-A607 (2017).

27. Sivula, K. & van de Krol, R. Semiconducting materials for photoelectrochemical energy conversion. *Nat. Rev. Mater.* **1**, 15010 (2016).

28. Walter, M. G. *et al.* Solar water splitting cells. *Chem. Rev.* **110**, 6446-6473 (2010).

29. Bae, D., Seger, B., Vesborg, P. C. K., Hansen, O. & Chorkendorff, I. Strategies for stable water splitting via protected photoelectrodes. *Chem. Soc. Rev.* **46**, 1933-1954 (2017).

30. Hamann, T. W. & Lewis, N. S. Control of the stability, electron-transfer kinetics, and pH-dependent energetics of Si/H_2O interfaces through methyl termination of Si(111) surfaces. *J. Phys. Chem. B* **110**, 22291-22294 (2006).

31. Scheuermann, A. G. & McIntyre, P. C. Atomic Layer Deposited Corrosion Protection: A Path to Stable and Efficient Photoelectrochemical Cells. *J. Phys. Chem. Lett.* **7**, 2867-2878 (2016).

32. Darling, R. M., Gallagher, K. G., Kowalski, J. A., Ha, S. & Brushett, F. R. Pathways to low-cost electrochemical energy storage: a comparison of aqueous and nonaqueous flow batteries. *Energy Environ. Sci.* **7**, 3459-3477 (2014).

33. Winsberg, J., Hagemann, T., Janoschka, T., Hager, M. D. & Schubert, U. S. Redox-Flow Batteries: From Metals to Organic Redox-Active Materials. *Angew. Chem. Int. Ed.* **56**, 686-711 (2017).

34. Kwabi, D. G. *et al.* Alkaline Quinone Flow Battery with Long Lifetime at pH 12. *Joule* **2**, 1894-1906 (2018).

35. Luo, J. *et al.* Unprecedented Capacity and Stability of Ammonium Ferrocyanide Catholyte in pH Neutral Aqueous Redox Flow Batteries. *Joule* (2018).

36. Beh, E. S. *et al.* A Neutral pH Aqueous Organic-Organometallic Redox Flow Battery with Extremely High Capacity Retention. *ACS Energy Lett.* **2**, 639-644 (2017).

37. Hu, B., Seefeldt, C., DeBruler, C. & Liu, T. L. Boosting the energy efficiency and power performance of neutral aqueous organic redox flow batteries. *J. Mater. Chem. A* **5**, 22137-22145 (2017).

38. Aaron, D. S. *et al.* Dramatic performance gains in vanadium redox flow batteries through modified cell architecture. *J. Power Sources* **206**, 450-453 (2012).

39. Seger, B. *et al.* Using TiO_2 as a conductive protective layer for photocathodic H_2 evolution. *J. Am. Chem. Soc.* **135**, 1057-1064 (2013).

40. Hu, S. *et al.* Amorphous TiO_2 coatings stabilize Si, GaAs, and GaP photoanodes for efficient water oxidation. *Science* **344**, 1005-1009 (2014).

41. Shaner, M. R., Hu, S., Sun, K. & Lewis, N. S. Stabilization of Si microwire arrays for solar-driven H_2O oxidation to $O_2(g)$ in 1.0 M KOH(aq) using conformal coatings of amorphous TiO_2. *Energy Environ. Sci.* **8**, 203-207 (2015).

42. Nocera, D. G. The artificial leaf. *Accounts of Chemical Research* **45**, 767-776 (2012).

43. Kamat, P. V., Tvrdy, K., Baker, D. R. & Radich, J. G. Beyond Photovoltaics: Semiconductor Nanoarchitectures for Liquid-Junction Solar Cells. *Chem. Rev.* **110**, 6664-6688 (2010).

44. Gratzel, M. Photoelectrochemical cells. *Nature* **414**, 338-344 (2001).

45. Green, M. A. *et al.* Solar cell efficiency tables (version 52). *Progress in Photovoltaics: Research and Applications* **26**, 427-436 (2018).

46. Park, M., Ryu, J., Wang, W. & Cho, J. Material design and engineering of next-generation flow-battery technologies. *Nat. Rev. Mater.* **2**, 16080-16018 (2016).

47. Ding, Y., Zhang, C., Zhang, L., Zhou, Y. & Yu, G. Molecular engineering of organic electroactive materials for redox flow batteries. *Chem Soc Rev* **47**, 69-103 (2018).

48. Hu, B., DeBruler, C., Rhodes, Z. & Liu, T. L. Long-Cycling Aqueous Organic Redox Flow Battery (AORFB) toward Sustainable and Safe Energy Storage. *J. Am. Chem. Soc.* **139**, 1207-1214 (2017).

49. DeBruler, C. *et al.* Designer Two-Electron Storage Viologen Anolyte Materials for Neutral Aqueous Organic Redox Flow Batteries. *Chem* **3**, 961-978 (2017).

50. Candea, R. M., Kastner, M., Goodman, R. & Hickok, N. Photoelectrolysis of Water: Si in Salt Water. *J. Appl. Phys.* **47**, 2724-2726 (1976).

51. Sun, K. *et al.* Enabling Silicon for Solar-Fuel Production. *Chem. Rev.* **114**, 8662-8719 (2014).

52. Sai, H. *et al.* Triple-junction thin-film silicon solar cell fabricated on periodically textured substrate with a stabilized efficiency of 13.6%. *Appl. Phys. Lett.* **106**, 213902 (2015).

53. Essig, S. *et al.* Raising the one-sun conversion efficiency of III-V/Si solar cells to 32.8% for two junctions and 35.9% for three junctions. *Nat. Energy* **2**, 17144 (2017).

CHAPTER 5

Perovskite/Silicon Tandem Solar Cell Powered High Performance Solar Flow Battery [*]

5.1 Abstract

The fast penetration of electrification to the rural areas calls for the development of competitive decentralized approaches. Integrated solar flow batteries (SFBs) represent a promising solution with compact footprint and low capital; however, the decoupled merits of efficiency and lifetime in the existing demonstrations impede their practical application. Here, we take advantage of the emerging high efficiency perovskite/Si tandem junction solar cells and the robust BTMAP-Vi/N^{Me}-TEMPO redox couples that are rationally designed to realize a high performance and stable SFB device. We develop new design principles and numerical analysis method to enable the optimal voltage match. These efforts have not only led to a new record solar-to-output electricity efficiency (*SOEE*) of 14.9% for SFBs, but also expanded the performance dimensions that can be well-covered by a single SFB device, including device lifetime, capacity utilization rate, power conversion efficiency utilization rate, and low cost. The conceptual breakthrough realized in this work also sheds light on the general future development strategies for SFBs.

---

[*] This chapter is a manuscript to be submitted, in collaboration with Zheng, J., Hu, B., Fu, H.-C., Zhao, Y., He, J.-H., Liu, T. L., Ho-Baillie, A. and Jin, S.

5.2 Introudction

The increasing demand for bringing electricity to rural areas poses many challenges but also presents a great opportunity for developing decentralized electrification systems[1,2]. Compared with conventional electrical grids based on large centralized power generation stations that are commonly seen in developed countries, decentralized electrification approach features smaller footprint, lower capital cost and shorter deployment time, and thus may penetrate much faster in rural locations. Due to the great abundance of solar resources, solar home systems (SHS) that cam transform sunlight into electricity and deliver the energy on-demand are believed to be one of the most feasible decentralized approaches in developing countries[3,4]. The most commonly seen SHS convert solar energy using photovoltaic (PV) panels and then store electricity in separate energy storage units, such as lead-acid batteries and Li-ion batteries[5]. Integrated devices that combine the functions of solar energy conversion with energy storage[6,7] could be quite suitable for SHS. Towards this end, the emerging solar flow batteries (SFBs) that monolithically integrate photoelectrochemical (PEC) solar cells and redox flow batteries (RFBs) in a single device[6,7] are very promising for SHS. The unique integrated design of SFB not only fulfills all the requisite functions for stand-alone SHS, but also may further reduce the overall size and capital cost of SHS[8,9].

Despite the short history of SFBs, considerable progress has been made recently in both mechanistic understandings[10-12] and device demonstrations of SFBs[13-24]. Among the various crucial metrics to make SFBs competitive for SHS applications, solar-to-output electricity efficiency (*SOEE*) and device lifetime have received most attention so far. The highest *SOEE* of 14.1% for SFBs to date was reached by an integration of III-V tandem solar cells and methyl viologen (MV)/4-hydroxy-2,2,6,6-tetramethylpiperidin-1-oxyl (4-OH-TEMPO) redox couples[11].

Nevertheless, the PEC corrosion-prone III-V materials[25,26] and the fast decomposition of 4-OH-TEMPO redox couples[27,28] greatly limit the lifetime of such SFB devices. Taking advantage of the recent progresses on photoelectrode protection[29-31] and stable organic redox couples[32], a very recent study using well-protected silicon photoelectrodes and robust bis-(trimethylammonio) propyl (BTMAP) functionalized redox couples demonstrated a SFB with significantly improved continuous operation lifetime of more than 200 hours but a lower *SOEE* of 5.4%[12] (an itemized comparison between the two aforementioned SFBs is shown in Figure A4.1) . With these advancements, the urgency lies in the pressing need for designing a monolithically integrated SFB that can deliver both high *SOEE* and long lifetime. Bearing such goals in mind, we turn our attention to silicon-based tandem solar cells that possess both stable silicon bottom cells, which, with proper protection layers, can prevent corrosion from aqueous electrolytes[33,34], and wider solar spectrum absorption range than single junction silicon solar cells to provide a high power conversion efficiency (PCE)[35]. To achieve the optimal voltage match between solar cells and redox couples which was previously shown to be critical for high *SOEE* in SFBs[11], the tandem junction solar cells need to be carefully designed to not only ensure high PCE but also yield suitable photovoltage. The emerging high efficiency perovskite/silicon tandem cells[36-38] thus stand out because of the exceptional tunability of the perovskite top layer in terms of band gaps and properties[39] compared to conventional inorganic top layer materials such as III-V and II-VI[40].

Therefore, we set out to design perovskite/silicon tandem junction solar cells for high performance SFBs. Here, we present a $(FAPbI_3)_{0.83}(MAPbBr_3)_{0.17}$ (MA= methylammonium, FA= formamidinium) perovskite/homo-junction silicon tandem junction solar cell with a carefully tuned photovoltage and a robust gold protection layer on the silicon bottom cell. We introduce a new theoretical modeling method, which, together with electrochemical study of state-of-the-art aqueous organic redox flow battery (AORFB) redox couples[41-49], predict that the bis-(trimethylammonio) propyl viologen (BTMAP-Vi) and 4-trimethylammoinium-TEMPO (N^{Me}-TEMPO) redox couples can be well matched with the perovskite/Si tandem junction solar cells. Enabled by such rational design, we demonstrate a new record *SOEE* for SFBs of 14.9%, which represents for an 82.8% PCE unitization rate. In addition, because only the protected silicon cell is exposed in aqueous electrolytes, the perovskite/silicon tandem cell and SFB presented here also exhibit long operation lifetime of more than 90 hours, near-unity capacity utilization rate, and relatively low cost.

5.3 Results and Discussion

5.3.1 Design of the perovskite/silicon tandem junction solar cells

There are three major considerations for designing perovskite/silicon tandem junction solar cells for high performance SFBs: suitable photovoltage, high PCE, good corrosion resistance when in contact with aqueous electrolytes. Our previous mechanistic study reveals that, in order to realize the highest possible *SOEE* for SFBs with certain solar cells, the maximum power point voltage (V_{MPP}) of the solar cell needs to be matched with the formal cell potential (E^0_{cell}, i.e. cell potential of SFB or RFB at 50% state-of –charge, SOC) determined by the redox couples chosen. Other than voltage matching, a higher E^0_{cell} is generally desired for SFBs since it is beneficial for improving the internal energy conversion efficiency, boosting discharging power density, and increasing energy density[50,51]. Considering the stable operation voltage window of aqueous electrolytes and the stability limitation of redox couples, E^0_{cell} for aqueous RFBs rarely exceeds 1.4 V[52], especially for AORFBs. Based on these considerations, we designed and fabricated $(FAPbI_3)_{0.83}(MAPbBr_3)_{0.17}$ perovskite/silicon tandem junction solar cells following a previous report[37] (Figure 5.1a and Figure A4.1). The current density-voltage (*J-V*) of this perovskite/Si solar cell was measured under the configuration shown in Figure 5.1b. The solid-state cell exhibited an open circuit voltage (V_{oc}) of 1.79 V, a short circuit current density (J_{sc}) of 12.9 mA/cm^2, a fill factor (FF) of 77.6% and a PCE of 18.0 % (Figure 5.1c). Importantly, the ratio between $FAPbI_3$ ($E_g \sim 1.5$ eV) and $MAPbBr_3$ ($E_g \sim 2.3$ eV) can be adjusted to tune the bandgap of the perovskite top layer and thus the photovoltage of the tandem cell, and thus we were able to achieve a V_{MPP} of 1.48 V, which is in the optimum range for aqueous organic SFBs as discussed above.

To protect the silicon bottom cell from aqueous electrolyte corrosion, a well-established method is to deposit Ti/TiO_2/Pt layers on Si[12,17]. However, the high temperature (>150 ^{o}C) required to deposit TiO_2 via commonly used atomic layer deposition (ALD) method makes this process not compatible with the heat sensitive perovskite top layer. Fortunately, because the kinetics of the RFB redox couples is usually very fast and no catalyst is needed for SFBs, a wide range of stable and conductive materials can be used to fabricate protection layers for various corrosion prone semiconductor materials[29,30]. For the ease of fabrication, we deposited a thin (100 nm) layer of gold on the Si bottom cell using thermal evaporation (Figure 5.1a), which proved to be a very robust protection material for Si in neutral aqueous electrolytes. We then fabricated the photoelectrode using the perovskite/Si cell protected with a bottom Au layer and characterized its solar performance under liquid junction cell configuration, in which photogenerated electrons are collected by BTMAP$^{4+/3+}$ redox couple at the Au-electrolyte interface and regenerated on the carbon felt counter electrode (Figure 5.1b). As shown in Figure 5.1c, the solar performance of liquid junction cell closely resembled that of the solid-state cell, indicating the fast charge transfer at the solid-liquid interface.

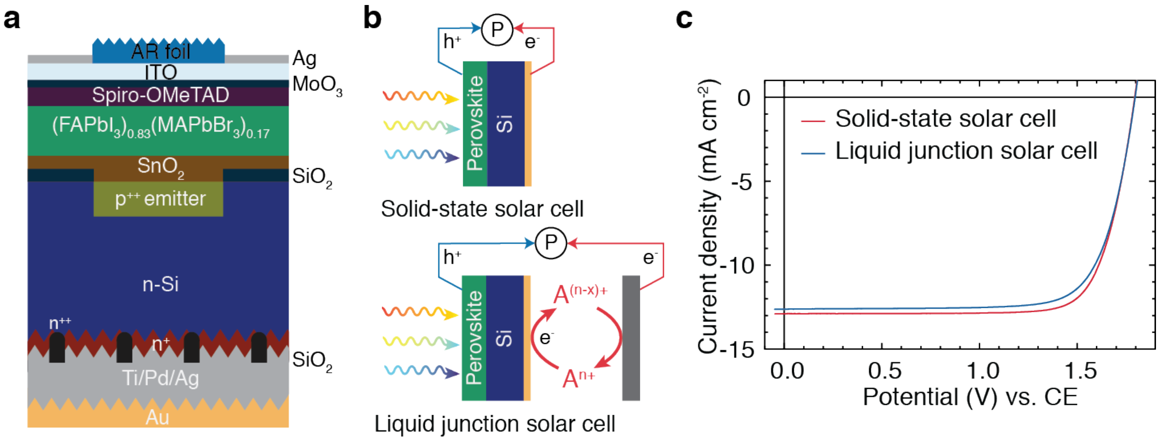

Figure 5.1. The schematic design and solar performance of perovskite/Si tandem solar cell. a, Architecture of the perovskite/Si tandem solar cell that consists of a (FAPBI$_3$)$_{0.83}$(MAPbBr$_3$)$_{0.17}$ top cell, a Si bottom cell and a 100 nm Au bottom protection layer. **b**, The configuration of solid-state solar cell and liquid junction solar cell. In the liquid junction solar cell configuration, only the Au bottom protection layer is exposed the electrolyte. **c**, J-V performance of solid-state perovskite/Si solar cell (red curve) and liquid junction solar cell fabricated from the same cell (blue curve). 0.1 M of BTMAP-Vi in 1 M NaCl (pre-reduced to 50% BTMAP-Vi^{4+}/50 % BTMAP-Vi^{3+}) was used as the electrolyte for the liquid junction solar cell measurement.

5.3.2 SFB performance estimation with theoretical modeling

Although previous studies suggest that to maximize the *SOEE* of SFB, E^0_{cell} of the SFB need to be properly matched with the V_{MPP} of solar cell, the idea of "voltage matching" is rather qualitative and does not necessary mean that E^0_{cell} should be equal to V_{MPP}. To gain a deeper understanding of the principles behind "voltage matching" and determine the exact E^0_{cell} that can enable the highest *SOEE* with the perovskite/Si tandem junction solar cells, we performed a qualitative calculation of *SOEE* with different hypothetical E^0_{cell}. E^0_{cell} generally remains constant with given anolyte/catholyte combination ($E^0_{cell} = E^0_{anolyte} - E^0_{catholyte}$, where

$E_{anolyte}^{0}\ and\ E\ _{catholyte}^{0}$ are the formal potentials for anolyte and catholyte, respectively). However, the actual cell potential (E_{cell}) of SFBs changes with SOC and can be calculated using the following equation derived from the Nernst equation:

$$E_{cell} = E_{cell}^{0} - \frac{RT}{nF} \ln \left[\frac{1-SOC}{SOC}\right]^{2} + IR_{DC}, \tag{1}$$

where R is the universal gas constant, T is temperature, n is the number of electrons transferred in redox reaction, F is Faraday constant, I is the applied current and R_{DC} is the DC resistance of SFB under RFB mode[50]. Figure 5.2a presents a series of representative E_{cell} -I lines (calculated with an arbitrary E_{cell}^{0} of 1.45 V) at different SOCs overlaid with the I-V curve of the liquid junction perovskite/Si photoelectrode (the blue curve in Figure 5.1c), from which we can find the operating points as indicated by the green circles. Taking advantage of the concept of instantaneous solar-to-output electricity efficiency ($SOEE_{ins}$)[12], which is defined as the power conversion efficiency of SFB at a specific SOC, we calculated the $SOEE_{ins}$ at different SOCs (Figure 5.2b) using the following equation:

$$SOEE_{ins} = \frac{P_{electrical,\ in}}{P_{illumination}} \times PE_{internal} = \frac{I_{operating}V_{operating}}{SA} \times CE \times EE, \tag{2}$$

where $P_{electrical,\ in}$ is the input electrical power provided by the photoelectrode, $P_{illumination}$ is the illumination power that can be calculated with input light irradiance (S) and the active area of photoelectrode (A), $PE_{internal}$ is the internal power conversion efficiency of SFB that consists of both Columbic efficiency (CE) and voltage efficiency (VE), $I_{operating}$ and $V_{operating}$ are the current and voltage at specific operating point of SFB, respectively.

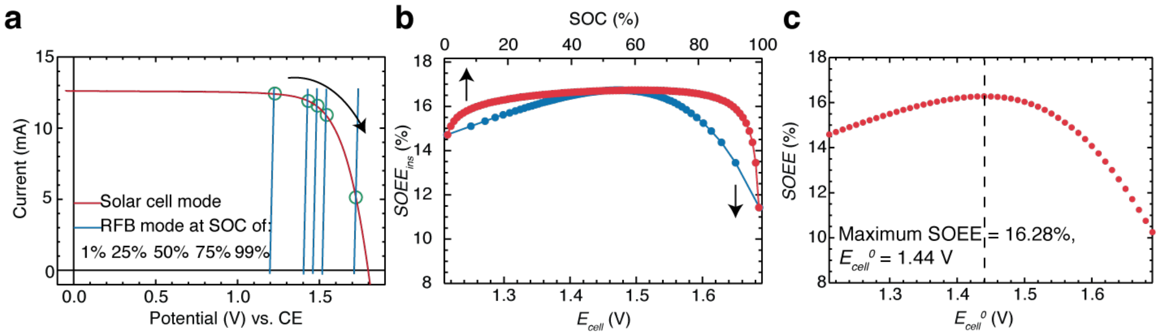

Figure 5.2. Calculation of *SOEE* as a function of E_{cell}^0. a, Representative overlaid I-V curves for photoelectrode measured under solar cell mode (red curve) and RFB calculated at different SOCs with a E_{cell}^0 of 1.45 V (blue lines). The green circles show the operating points at specific SOCs, which move alone the photoelectrode I-V curve as SOC increases. **b**, Representative SOEE$_{ins}$ with respect to SOC (red curve) and E_{cell} (blue curve) calculated with a E_{cell}^0 of 1.45 V. **c**, Calculated *SOEE* as a function of Ecell^0 between 1.2 to 1.7 V, showing a maximum of 16.28% when E_{cell}^0 is 1.44 V.

The overall *SOEE* of a SFB operated between 1% SOC and 99% SOC (98% capacity utilization rate) can be calculated as the integrated average of *SOEE$_{ins}$* with respect to SOC (Figure 5.2b). By repeating the calculation described above with different E_{cell}^0s from 1.20 to 1.70 V with a 10 mV interval, we reveal the qualitative relationship between *SOEE* and E_{cell}^0 (Figure 5.2c). A maximum *SOEE* of 16.28% is found at a E_{cell}^0 of 1.44 V. Despite the similar appearance between the *SOEE*-E_{cell}^0 and *SOEE$_{ins}$*-E_{cell} curves, they convey completely different information and should be carefully differentiated (see Figure A4.3 for a comparison between these two curves). Although the best matched E_{cell}^0 obtained from the *SOEE*-E_{cell}^0 relationship is very close to the V_{mpp} of perovskite/Si solar cell herein, we do not anticipate this is always the case for other SFBs, especially when the FF of the liquid junction cells is far from ideal (e.g., < 60%).

5.3.3 The design and electrochemical study of electrolytes

To design the electrolytes for high performance SFBs, we mainly focused on three aspects that echo the design principles for solar cells discussed above: low corrosiveness, good voltage matching, long lifetime. We specifically targeted those redox couples soluble and stable in neutral pH to minimize the corrosiveness of electrolytes to the solar cells. As revealed in the $SOEE$-E^0_{cell} relationship discussed above, E^0_{cell} need to be at least 1.25 V to enable a *SOEE* higher than 15% (Figure 5.2c), which led us to the three redox couple pairs shown in Figure 5.3a: $MV^{2+/+}$ and $[4\text{-}OH\text{-}TEMPO]^{+/\cdot}$ (E^0_{cell} = 1.26 V)[27], $[BTMAP\text{-}Vi]^{4+/3+}$ and $[N^{Me}\text{-}TEMPO]^{+/\cdot}$ (E^0_{cell} = 1.29 V)[43], $[BTMAP\text{-}Vi]^{3+/2+}$ and $[FcN]^{2+/+}$ (FcN = (ferrocenylmethyl)trimethylammonium)) (E^0_{cell} = 1.31 V) [43,53].

The stability of these redox couples was assessed by RFB galvanostatic cycling tests conducted in a nitrogen purge box using electrolytes consisted of 0.10 M redox couples and 1.0 M NaCl as supporting salt. Selemion AMV anion-exchange membrane was used to separate the anolyte and catholyte in the RFB tests. To accurately measure the capacity, a low current density of 2.5 mA/cm^2 was used during the galvanostatic cycling tests without a potentiostatic step at cutoff potentials. Figure 5.3b shows the normalized capacity-time profile for the RFBs during cycling tests, from which the temporal capacity fade rate of each RFB can be calculated using the following equation: $\text{capacity fade rate} = \frac{capacity\ (t_0) - capacity\ (t_1)}{(t_1 - t_0)}$. The capacity fade rate for these full cell RFB tests is a measure of the overall RFB stability that can be affected by many factors, including both the degradation and membrane crossover of the anolyte/catholyte redox couples[54]. The high capacity fade rates for RFBs built with $MV^{2+/+}$ and $[4\text{-}OH\text{-}TEMPO]^{+/\cdot}$(9.13% per day), and $[BTMAP\text{-}Vi]^{3+/2+}$ and $[FcN]^{2+/+}$ (4.78% per day) can be mainly attributed to the fast chemical degradation of $[\text{4-OH-TEMPO}]^{+/\cdot}$ and $[\text{BTMAP-Vi}]^{3+/2+}$ redox couples[27,43]. Despite the fact that BTMAP-Vi is considered to be one of the most stable redox couples for AORFBs[32], we found that it is only stable when the reduction reaction is limited to the first redox state at -0.353 V. The access of the second redox state at -0.703 V would significantly accelerate the degradation of BTMAP-Vi, possibly through the reaction with residual oxygen in the N_2 purge box (Figure A4.4)[28]. In addition, the lower hydrogen evolution reaction (HER) overpotential on the surface of Au than carbon would also prevent us from reaching the second redox state of BTMAP-Vi using Au protected perovskite-Si photoelectrode (Figure A4.5). In contrast, RFB built with $[\text{BTMAP-Vi}]^{4+/3+}$ and $[\text{N}^{\text{Me}}\text{-TEMPO}]^{+/\cdot}$ exhibited a particularly low temporal capacity fade rate of 0.598% per day (Figure A4.6a), which is among the most stable AORFBs reported so far[28,43-45]. Detailed characterization of the $[\text{BTMAP-Vi}]^{4+/3+}/[\text{N}^{\text{Me}}\text{-TEMPO}]^{+/\cdot}$ RFB revealed an actual E_{cell}^{0} of 1.26 V (Figure A4.7a), which is very close to the E_{cell}^{0} of 1.29 V estimated from cyclic voltammetry (CV) shown in Figure 5.3a. Furthermore, the use of Selemion AMV anion exchange membrane ensured a very low redox specious crossover as confirmed by ^{1}H-nuclear magnetic resonance spectroscopy (^{1}H-NMR) and CV (Figure A4.8, 9), although at the cost of a relatively high cell resistance (Figure A4.7b, c) and lower energy efficiency at high current densities (Figure A4.6b)[55].

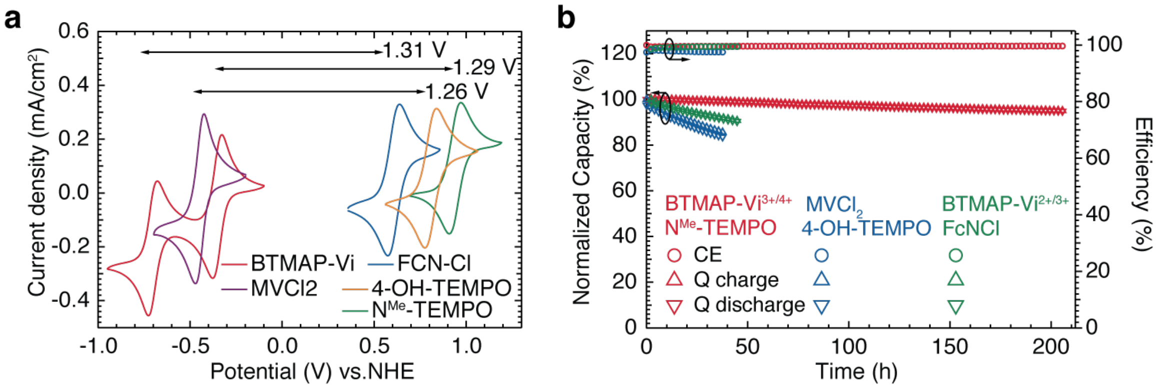

Figure 5.3. Electrochemical characterization of redox couples and RFBs. a, Cyclic voltammograms of 3 different AORFB redox couple pairs that can enable a $E_{cell}{}^{0}$ higher than 1.25 V. All voltammograms are scanned at 10 mV s^{-1} on a glassy carbon electrode using electrolytes containing 5.0 mM active redox species and 1.0 M NaCl. **b**, RFB normalized capacity (triangles) and Coulombic efficiency (circles) during galvanostatic cycling at 2.5 mA cm^{-2} with different redox couple pairs, showing the outstanding stability of BTMAP-Vi/N^{Me}-TEMPO RFB.

5.3.4 Characterization and analysis of integrated SFB device

After careful validating the individual components, we built the SFB device using the same perovskite/Si photoelectrode and BTMAP-Vi/N^{Me}-TEMPO redox couples. The SFB can be switched among three main modes: solar cell mode, solar recharge mode, and RFB mode (the details for each configuration are presented in Figure A4.10). The cycling test of the SFB was performed by first charging the device under solar recharge mode with simulated solar irradiation at 100 mW cm^{-2} (1 Sun) until reaching the upper cutoff potential of 1.5 V, and then discharging the device galvanostatically until reaching the lower cutoff potential of 0.8 V. By using an upper voltage cutoff rather than a time cutoff that was commonly used for other SFBs[11,12] during the solar charging process, we can ensure a near-unity capacity utilization rate (based on the OCV-SOC relationship presented in Figure A4.7a) regardless of the photocurrent fluctuation or capacity decay. The photocurrent and cell potential (blue and red curve in Figure 5.4a, respectively) were monitored during the solar charging process with two synchronized potentiostat channels. Due to movement of operating points (Figure 5.2a), the photocurrent gradually decreases as the cell voltage increases, with an average of 11.9 mA/cm^2. During the galvanostatic discharging process, the simulated solar irradiation was blocked by a programmed beam block and the connection between photoelectrode and anode was switched to open circuit, leaving only the cell potential to be recorded. To match the average photocurrent during the solar charging process, a discharging current of 12 mA was applied. Despite the relatively large membrane resistance of Selemion AMV membrane used here, the low discharging current only entailed a very small overpotential to drive the discharging reaction, as indicated by the near mirror-image cell voltage curves during solar charging/discharging process.

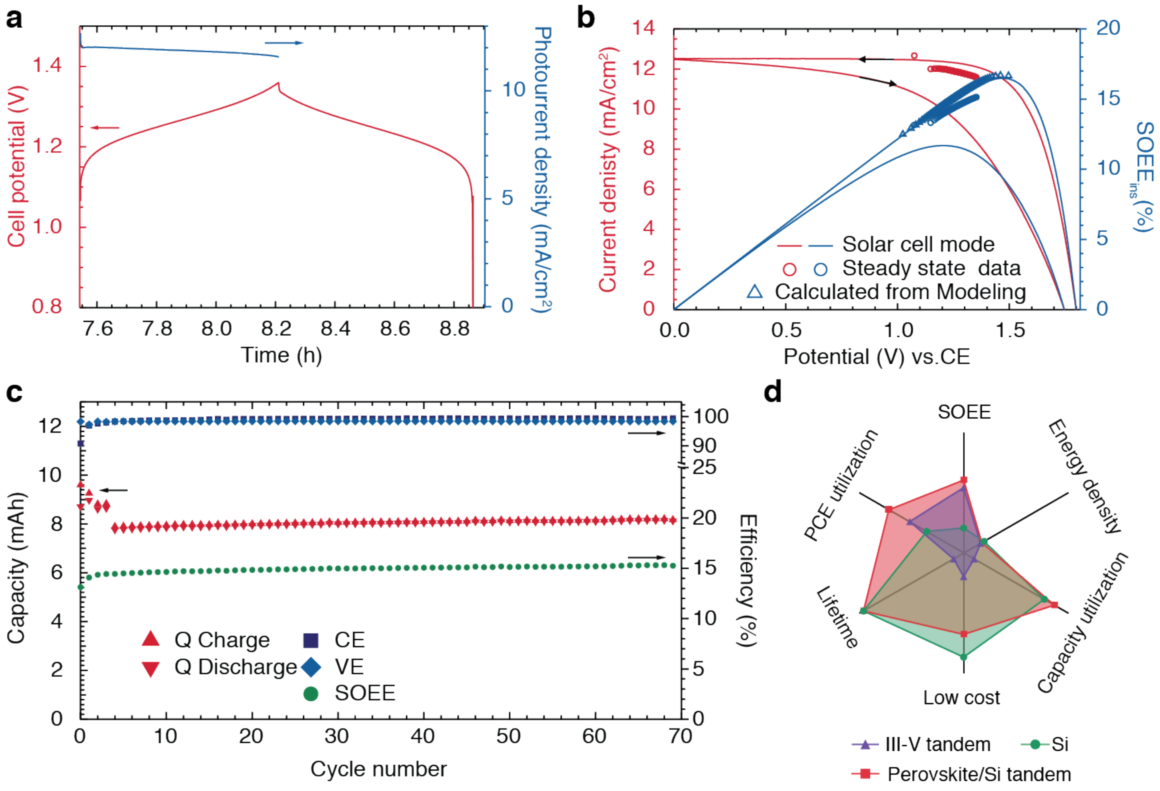

Figure 5.4. Performance of integrated SFB built with perovskite/Si solar cell and BTMAP-Vi/N^{Me}-TEMPO redox couples. a, Representative device the cycling behavior of SFB at the 5th cycle. The cell potential (red curve) was measured under RFB mode and the photocurrent density (blue curve) was measured under SFB solar recharge mode. **b,** *J-V* curve (red curve) of photoelectrode measured with forward (-0.05 to 1.80 V) and backward (1.80 to -0.05 V) linear scan voltammetry under solar cell mode and the corresponding solar cell power conversion efficiency (blue curve). The $SOEE_{ins}$ was calculated with the modeling method shown in Figure 5.2 using backward linear scan voltammetry data with a $E_{cell}{}^0$ of 1.26 V. The steady state photocurrent density (red circles) and $SOEE_{ins}$ (blue circles) were calculated from data in **a.**, which exhibited a slight decrease from the backward scanned J-V data. **c**, Charge and discharge capacity (red triangles), Coulombic efficiency (purple squares), voltage efficiency (blue rhombs), and *SOEE* (green circles) of SFB over 70 cycles, showing a stable cycling performance. **d**, Comparison

of the SFB reported in this work with the other two previously demonstrated SFBs in a multivariate radar chart.

From the data shown in Figure 5.4a, we calculated a *SOEE* of 14.9%, which is only slightly different from the calculated *SOEE* of 15.1 % with a E_{cell}^{0} of 1.26 V (as shown in Figure 5.2c). We sought to analyze such subtle mismatch to get a better understanding of the device behavior. One commonly seen phenomenon for perovskite-based solar cells is the large hysteresis between forward and backward linear scan voltammetries (LSVs), which is also observed for the liquid junction perovskite/Si solar cells, possibly due to charge accumulation at the solid-liquid interface (Figure 5.4b). During the solar charging process, because the voltage change was very slow (usually < 0.1 mV/s), we were able to find the steady state operating current and voltage, and further calculate the steady state $SOEE_{ins}$ using equation 2. As can be seen in Figure 5.4b, the steady state performance of the liquid junction perovskite/Si solar cell is very close, albeit different, to that recorded in the backward LSV scan. Such subtle difference is the main reason for the minor mismatch between the calculated *SOEE* and the actual *SOEE* of the SFB (Figure 5.4c).

The SFB was continuously cycled for 70 cycles (94 hours) and maintained a very stable performance during the whole time of operation. Figure 5.4c shows that the SFB can deliver an average discharge capacity of 0.79 Ah L^{-1} (calculated based on the total volume of anolyte and catholyte) with a near-unity CE and VE of 99.0% and 98.4%, respectively. The average *SOEE* of 14.9% achieved by the SFB sets a new record for the integrated solar rechargeable battery devices[11]. Importantly, thanks to the good voltage match between the perovskite/Si tandem junction solar cell and the BTMAP-Vi/N^{Me}-TEMPO redox couples, we were able to achieve the new record *SOEE* with a solar cell that only exhibited a solid-state PCE of 18%, which is much lower that of the III-V tandem solar cell (26.1%) used in the previous record-holding device[11]. Naturally, the ratio between *SOEE* and PCE can be used as a quantitative measure of the voltage match and we propose to name it PCE utilization rate. In addition to the *SOEE* and PCE utilization, capacity utilization, lifetime and cost are also important. By qualitatively plotting the six most important metrics for SFBs in a radar plot, we can clearly see that, unlike the other two previously reported SFBs that can only cover a few performance dimensions well, the SFB based perovskite/silicon solar cells demonstrated here can deliver good performance in five out six dimensions (Figure 5.4d).

5.4 Conclusions

This work presents a monolithically integrated SFB device based on perovskite/silicon tandem solar cells that features significant breakthroughs in many dimensions, including *SOEE*, PCE utilization rate, and capacity utilization rate, without compromises in device lifetime and low cost. We have rationally designed the $(FAPbI_3)_{0.83}(MAPbBr_3)_{0.17}$ perovskite/silicon tandem junction solar cells specifically for aqueous organic SFBs that takes advantage of not only highly efficient tandem junction design for achieving high efficiency but also the robust silicon semiconductor electrolyte contact for high stability. We have also developed a new numerical analysis method to not only successfully guide us to the selection of BTMAP-Vi/N^{Me}-TEMPO redox couples to match with the perovskite/silicon cells but also shed light on the deeper quantitative understanding of the voltage matching principles. These results constitute a significant advance toward a practical approach of using integrated SFBs for SHS and other remote electrification applications.

5.5 Methods

5.5.1 Electrochemical measurements

Cyclic voltammetry (CV) and steady state linear sweep voltammetry (LSV) measurements were conducted using Bio-Logic SP-200/BP-300/VMP3 potentiostat. A 3 mm diameter glassy carbon disk electrode (BASi or CH Instruments) were used as the working electrode, which was polished using 0.3 μm and 0.05 μm alumina slurry to mirror polish and washed with deionized water (Milli-Q, 18.2 MΩ cm) and methanol before each test. The glassy carbon electrode was further cleaned electrochemically in 1 M Na_2SO_4 solution (with 1 mM potassium ferrocyanide as internal reference) by swiping potential between -1.0 V and 1.5 V *vs.* reference electrode at 100 mV/s until the peak separation of ferrocyanide/ferricyanide redox couple reaches ca. 60 mV. A Pt wire electrode (0.5 mm diameter) and a saturated calomel electrode (SCE, CH Instruments) were used as the counter and reference electrodes, respectively. The electrolyte consisted of 5 mM of active redox material and 1.0 M NaCl and was purged with inert gas (argon or nitrogen) before measurements. CV was scanned at a scan rate of 10 mV/s and the formal potential of the redox couples were estimated by calculating the average potential between anodic peak and cathodic peak in the CV curves. Electrochemical kinetics of the two redox couples was studied using a rotating disk electrode (BASi, RDE-2) at different rotating speed. LSV was scanned at a scan rate of 10 mV/s. The diffusion coefficient (D) of the N^{Me}-TEMPO was calculated using Levich equation, $i_l = 0.62nFAD^{2/3}\omega^{1/2}\upsilon^{-1/6}C$, where n = 1, F = 96,485 C/mol, A = 0.0707 cm^2, C = 5.0 mM, $\upsilon = 0.9380 \times 10^{-2}$ cm^2/s (kinematic viscosity of 1.0 M NaCl at 298 K) and i_l determined at an absolute overpotential ($|\eta|$) of 200 mV. Koutecký–Levich plots ($1/i$ *vs.* $\omega^{-1/2}$) were used to determine the kinetic currents (i_k) at different overpotentials by extrapolating the fitted $1/i$ *vs.* $\omega^{-1/2}$ lines to $\omega^{-1/2} = 0$. The standard rate constants (k_0) and transfer coefficient (α, reduction reaction) were calculated using the Butler-Volmer equation by linearly fitting a Tafel plot (log i_k *vs.* η) between an $|\eta|$ region of 40-80 mV. The RDE experiments were performed 3 times for each redox couple to obtain the average value for D, k_0 and α.

5.5.2 Fabrication of RFB and integrated SFB device

The RFB and SFB measurements were carried out in a custom-made zero-gap device, similar to what was reported previously.[11] In brief, Graphite plates (1/8-inch thickness, MWI) were used as current collector for RFB devices. Modified current collectors with additional 15 × 15 mm clearance window at the center of the square pocket were used for SFB devices to allow direct contact between photoelectrode and liquid electrolyte. 20×20 mm graphite felts (GFD 3 EA, SIGRACELL$^{\circledR}$) were pre-treated at 400 ^{o}C in air for 6 h before being used as electrodes on both sides of the cell. 25 × 25 mm Selemion AMV (Ashahi Glass Co., Ltd.,) was used as an anion-exchange membrane. All RFB and SFB measurements were carried out in a custom modified N_2 flush box (Terra Universal) with continuous N_2 flushing.

5.5.3 General RFB measurements

5.0 mL solutions of 0.1 M redox active specious in 1.0 M NaCl were used as electrolytes for RFB tests. N^{Me}-TEMPO and FcNCl were synthesized following the method described in the previous report[43]. The electrolytes were purged with nitrogen for at least 1 hour before tests. The electrolyte flow rate was controlled at 20 mL/min for all RFB measurements. The RFB was kept in a nitrogen purge box (Terra Universal) during the whole RFB test.

The RFB cycling and polarization performance tests were carried out using a Bio-Logic BP-300 or SP-200 potentiostat. Galvanostatic cycling tests were performed by charging and discharging the device at a desired constant current density with the following potential windows: 0.7 - 1.5 V for MV$^{2+/+}$ and [4-OH-TEMPO]$^{+/\cdot}$, 0.8-1.6 V for [BTMAP-Vi]$^{4+/3+}$ and [N^{Me}-TEMPO]$^{+/\cdot}$, 1.1-1.6 V for $[\mathrm{BTMAP\text{-}Vi}]^{3+/2+}$ and $[\mathrm{FcN}]^{2+/+}$, 0.5-1.1 V for $[\mathrm{BTMAP\text{-}Vi}]^{4+/3+}$ and $[\mathrm{FcN}]^{2+/+}$. To measure open circuit voltage (OCV) of the RFB at different states of charge (SOCs), the battery was galvanostatically charged or discharged with a 10% SOC step and then rested for 2 min to measure the OCV. The 0% SOC and 100% SOC were accessed by the galvnostatic-potentiostatic cycling method until the current density reached 1 $\mathrm{mA/cm^2}$ at cutoff potentials[12]. The RFB was kept at open circuit for 20 mins to get a stable measurement of OCV for 0% and 100% SOC. In the cell polarization characterization, a LSV scan was performed at a scan rate of 100 mV/s. Forward scan (0-1.6 V) was used at 0%SOC and backward scan (1.6-0 V) was used for all the other SOCs to minimize SOC swing during LSV test. To further avoid the disturbance of SOC by LSV scans, the RFB was completely discharged to 0% SOC and then recharged to the specific SOC before each LSV was measured. All the SOCs mentioned in this study were calculated based on potentiostatic capacity determined using the galvnostatic-potentiostatic cycling method. Potentiostatic electrochemical impedance spectroscopy (EIS) measurement of the RFB was performed at 0% SOC, with a voltage offset of 10 mV, a bias potential equals to its open circuit voltage, and frequencies ranging from 100 kHz to 1 Hz.

5.5.4 Fabrication of photoelectrode assembly for the integrated SFB device

The fabrication of $(\mathrm{FAPbI_3})_{0.83}(\mathrm{MAPbBr_3})_{0.17}$ perovskite/homo-junction silicon tandem solar cell solar cells followed the method previously reported[37]. In brief, n-type <100>Si wafer with a thickness of 300 μm was used to prepare the bottom silicon cell with n^{++} (from $\mathrm{POCl_3}$) rear contacts, n^{+} high-low junction, p^{++} (from $\mathrm{BBr_3}$) front emitter and Ti/Pd/Ag back metal contacts. The p^{++} area was controlled to 1 $\mathrm{cm^2}$ to defined the active area with thermally grown $\mathrm{SiO_2}$ covering the non-contacted area. On top of the cleaned p^{++} area, $\mathrm{SnO_2}$ was deposited as the electron transport layer using spin coating and backing followed by the deposition of perovskite layer by spin coating and annealing at 100 ℃ for 20 min. The perovskite precursor solution was prepared by dissolving formamidinium iodide (FAI, 1 M), lead iodide (1.1 M), methylammonium bromide (MABr, 0.2 M), and lead bromide (0.2 M) in a mixed solvent of N,Ndimethylformamide (DMF) and dimethyl sulfoxide (DMSO) (4:1 v/v). 2,2',7,7'-tetrakis(N,N-di-pmethoxyphenylamine)-9,9-spirobifluorene (spiro-OMeTAD) hole transport layer, MoO_x transparent electrode and ITO transparent contact were the deposited sequentially using spin coating, thermal evaporation and RF sputtering on top of the perovskite layer. A metal frame of silver was deposited by thermal evaporation defining the area of 1 cm^2 alighing well with the bottom p^{++} Si emitter area.

The photoelectrode assembly for the integrated SFB device characterization was fabricated using the method similar to that described in a previous report[12]. In brief, the perovskite/Si tandem cell was affixed onto a custom-made graphite current collector by epoxy resin (Hysol 9460) to cover the window of the current collector. The electrolyte can directly contact the back side of the silicon cell through the window of the current collector and harvest photogenerated charges during SFB device operation in solar recharge mode and solar cell mode. The ohmic contact to photoelectrode was made by attaching a copper foil onto the front Ag metal contact area of the cell with Ga/In eutectic mixture (Sigma Aldrich) and fixed with silver paint (Ted Pella, PELCO colloidal silver). The ohmic contact area was then sealed by epoxy resin.

5.5.5 Solid state and liquid junction cell characterization of perovskite/silicon solar cell

Solid state *J-V* performance of the perovskite/silicon cells were measured in a two-electrode configuration by making ohmic contact to the front and back side of the cell with tungsten probe and copper plate. The LSV data was collected using a Bio-Logic SP-200 potentiostat under 1 Sun (100 mW cm^2) of AM 1.5 G simulated illumination by a Newport Model 91191 Xenon arc lamp solar simulator with a scan rate of 100 mV/s. A certified reference Si cell (Abet Technologies) was used to calibrate the illumination intensity of the AM 1.5G solar simulator to 100 mW/cm^2.

The liquid junction solar cell characteristics of the perovskite/silicon photoelectrodes were measured in the assembled SFB device with a Bio-Logic BP-300 potentiostat under 1 Sun (100 mW/cm^2) of simulated solar illumination provided by the same Xenon arc lamp mentioned above with a branched flexible silica light guild (Edmund) fed through a N_2 flush box and collimated by an OSL2COL convex lens collimation tube (Thorlabs). To calibrate illumination intensity inside the N_2 purge box, short circuit current (I_{sc}) of a solid state single junction Si solar cell (1.0 cm^2) was first measured under 1 Sun of AM1.5 G simulated solar light outside the box, then the solar simulator was tuned to generate the same I_{sc} using the same solid state Si solar cell measured inside the box with light guide and collimator. The liquid junction cell measurements were performed in a two-electrode configuration under both solar cell mode and solar recharge mode (Figure A4.10) with the same electrolytes used in the RFB test (0.1 M N^{Me}-TEMPO as anolyte and 0.1M BTMAP-Vi as catholyte, both with 1.0 M NaCl as supporting electrolyte). To study the influence of SOC on the performance of photoelectrodes, the liquid junction cell measurements were carried out at different SOCs by galvanostatically charging the SFB to the desired SOC from 0% SOC. The liquid junction cell measurements at 50% SOC were also repeated at different flow to investigate the relationship between mass transport and liquid junction cell performance of the photoelectrode. A relatively slow flow rate (20 mL/min) was used for all the other liquid junction cell measurements because the the performance is insensitive to the flow rate. All LSV curves were recorded at a scan rate of 100 mV/s without correcting for any uncompensated resistance losses. CV curves (forward and backward LSVs) were recorded at a scan rate of 30 mV/s.

5.5.6 Integrated SFB device characterization

The integrated SFB device was assembled with a photoanode assembly, a photocathode assembly, and all the other components the same as the RFB device described in the previous section. The electrolyte flow rate was controlled at 20 mL/min for all the SFB cycling tests, if not specified otherwise.

To characterize the charging-discharging behaviors of the integrated SFB devices, a Bio-Logic BP-300 bi-potentiostat was used: channel 1 was configured as solar recharge mode to monitor the photocurrent; channel 2 was configured as RFB mode to monitor the potential difference between the two carbon felt electrodes (the connections for different modes are illustrated in Figure A4.10). During the solar recharging process, perovskite/silicon photocathode and was illuminated at 1 Sun without applying any external bias until the cell potential measured by channel 2 reaching the upper cutoff potential of 1.5 V. During the discharging process, the illumination was blocked by an analog signal regulated beam shutter, and the integrated device was operated as a normal RFB with a discharging current of -10 mA applied by channel 2 until the cell potential reached 0.8 V. The discharging current was selected to match the average solar recharging current. The light intensity was monitored using a solid state Si single junction solar cell illuminated by the other branch of the light guide to ensure no significant light intensity change during the SFB cycling test.

The total capacity of the SFB device was measured by galvanostatic-potentiostatic method before and after SFB cycling test to confirm no significant amount of capacity was lost during cycling.

5.5.7 SFB performance estimation with theoretical modeling

In order to quantitatively evaluate the solar conversion and energy storage efficiency of the integrated SFB device, a specific Figure of merit should be considered: solar-to-output electricity efficiency (SOEE), which is defined by the ratio of the usable electrical energy delivered by the integrated SFB device ($E_{electrical,out}$) over the total solar energy input ($E_{illumination}$). The *SOEE* can be calculated using equation 1[17]:

$$SOEE = \frac{E_{electrical,out}}{E_{illumination}} = \frac{\int I_{out} V_{out} dt}{\int SA dt} \tag{1}$$

where I_{out} is the output (discharging) current, V_{out} is the output voltage, S is the total incident solar irradiance calibrated to 100 mW/cm^2, and A is the total illumination area of the perovskite/Si photoelectrode (1.0 cm^2). Note that this *SOEE* is the *round-trip efficiency* of the delivered electrical energy at any time on demand over the original solar energy input.

The hypothetical overlaid *J-V* curves of photoelectrodes shown in Figure 5.2a illustrates that the operating point for the integrated SFB device could be significantly influenced by the working voltage matching between the photoelectrode and the SFB cell potential. Even though the *I-V* characteristic of the photoelectrode generally remains unchanged at different SOCs, the SFB cell potential may vary greatly during its charging/discharging process, resulting in a considerable *SOEE* change at different SOCs. To quantitatively analyze such *SOEE* change at different charging/discharging state of the SFB, an instantaneous *SOEE* can be defined and estimated using the following equation[12]:

$$SOEE_{ins} = \frac{P_{electrical,out}}{P_{illumination}} \approx \frac{P_{electrical,in} \times PE_{internal}}{P_{illumination}} = \frac{I_{operating} V_{operating}}{SA} \times CE \times EE$$

where $P_{electrical,in}$, $P_{eletrical,out}$ and $P_{illumination}$ are the electrical charging power of the SFB, electrical discharging power of the SFB and illumination power provided by the solar simulator; $PE_{internal}$ is internal power conversion efficiency of the SFB, which can be estimated as the arithmetic product of Coulombic efficiency (*CE*) and voltage efficiency (*VE*) of the SFB; $I_{operating}$ is operating photocurrent provided by the photoelectrode during solar recharging process and $V_{operating}$ is the corresponding cell potential measured at the same time as $I_{operating}$.

To find the cell voltage profile of SFB, we used a simple battery model assuming ideal Nernstian behavior and constant DC resistance[50]. Thus, the cell potential can be calculated using the following equation.

$$E_{cell} = E^0_{cell} - \frac{RT}{nF} \ln \left[\frac{1 - SOC}{SOC}\right]^2 + IR_{DC}$$

where R is the universal gas constant, T is temperature, n is number of electrons in redox reaction, F is Faraday constant, I is the applied current and R_{DC} is the DC resistance of SFB under RFB mode. Because the operating current won't be higher than J_{sc} (12.9 mA) of the perovskite/Si solar cell (Figure 5.1c) and R_{DC} is around 1.2 Ω (Figure A4.6c), IR_{DC} (<15 mV) doesn't contribute significantly to E_{cell} and is neglected in the calculation for simplicity. E_{cell} is calculated from 1% SOC to 99% SOC with an increment of 1% using an arbitrary E^0_{cell} to find $V_{operating}$ ($V_{operating} = E_{cell}$) at different SOCs. Because IR_{DC} is neglected, $I_{operating}$can be easily found from the *I-V* curve of the liquid junction perovskite/Si solar cell and thus $SOEE_{ins}$ can be calculated as discurbed above. The average *SOEE* for SFB operated from 1% SOC to 99% SOC is then given by:

$$SOEE = \frac{\sum_n SOEE_{ins}(n\%\ SOC)}{\sum n}.$$

Note that summation rather than integration is used here because the numerical calculation is already based on uniformly spaced SOCs. For experimental data with non-uniformly spaced SOCs, integration should be used to calculate $SOEE$ as the integral average of $SOEE_{ins}$. By repeating the calculation described above with different E_{cell}^{0} inputs, we can finally obtain the $SOEE$-E_{cell}^{0} relationship with interested E_{cell}^{0} range.

The modeling method used in this study only considers the cell voltage profile of SFB. So the I-V curve of the liquid junction perovskite/Si solar cells need to be experimentally measured and used as an input information before conducting the calculation. This method can be further revised with additional modeling for the liquid junction solar cells with the input of much simplified parameters (such as Voc, Jsc, FF) so that it can be generally used to estimate $SOEE$-E_{cell}^{0} relationship for other solar cells even without having their I-V curve.

5.6 References

1. Eke, K. P. Emerging Considerations of Rural Electrification Infrastructure Development in Africa. *2017 Ieee Pes Powerafrica Conference*, 138-142 (2017).

2. Cook, P. Infrastructure, rural electrification and development. *Energy Sustain Dev* **15**, 304-313 (2011).

3. Wamukonya, N. Solar home system electrification as a viable technology option for Africa's development. *Energ Policy* **35**, 6-14 (2007).

4. Halder, P. K. Potential and economic feasibility of solar home systems implementation in Bangladesh. *Renew. Sust. Energ. Rev.* **65**, 568-576 (2016).

5. Charles, R. G., Davies, M. L., Douglas, P., Hallin, I. L. & Mabbett, I. Sustainable energy storage for solar home systems in rural Sub-Saharan Africa - A comparative examination of lifecycle aspects of battery technologies for circular economy, with emphasis on the South African context. *Energy* **166**, 1207-1215 (2019).

6. Gurung, A. & Qiao, Q. Q. Solar Charging Batteries: Advances, Challenges, and Opportunities. *Joule* **2**, 1217-1230 (2018).

7. Schmidt, D., Hager, M. D. & Schubert, U. S. Photo-rechargeable electric energy storage systems. *Adv. Energy. Mater.* **6**, 1500369 (2015).

8. Yu, M., McCulloch, W. D., Huang, Z., Trang, B. B., Lu, J., Amine, K. & Wu, Y. Solar-powered electrochemical energy storage: An alternative to solar fuels. *J. Mater. Chem. A* **4**, 2766-2782 (2016).

9. Jin, S. What Else Can Photoelectrochemical Solar Energy Conversion Do Besides Water Splitting and CO2 Reduction? *ACS Energy Lett.* **3**, 2610-2612 (2018).

10. Wedege, K., Bae, D., Dražević, E., Mendes, A., Vesborg, P. C. K. & Bentien, A. Unbiased, complete solar charging of a neutral flow battery by a single Si photocathode. *RSC Adv.* **8**, 6331-6340 (2018).

11. Li, W., Fu, H.-C., Zhao, Y., He, J.-H. & Jin, S. 14.1% Efficient Monolithically Integrated Solar Flow Battery. *Chem* **4**, 2644-2657 (2018).

12. Li, W., Kerr, E., Goulet, M.-A., Fu, H.-C., Zhao, Y., Yang, Y., Veyssal, A., He, J.-H., Gordon, R. G., Aziz, M. J. & Jin, S. A Long Lifetime Aqueous Organic Solar Flow Battery. *Adv. Energy. Mater.* **9**, 1900918 (2019).

13. Liu, P., Cao, Y. l., Li, G. R., Gao, X. P., Ai, X. P. & Yang, H. X. A Solar Rechargeable Flow Battery Based on Photoregeneration of Two Soluble Redox Couples. *Chemsuschem* **6**, 802-806 (2013).

14. Wedege, K., Bae, D., Smith, W. A., Mendes, A. & Bentien, A. Solar Redox Flow Batteries with Organic Redox Couples in Aqueous Electrolytes: A Minireview. *J. Phys. Chem. C* **122**, 25729-25740 (2018).

15. Yu, M. Z., McCulloch, W. D., Beauchamp, D. R., Huang, Z. J., Ren, X. D. & Wu, Y. Y. Aqueous Lithium-Iodine Solar Flow Battery for the Simultaneous Conversion and Storage of Solar Energy. *J. Am. Chem. Soc.* **137**, 8332-8335 (2015).

16. Liao, S., Zong, X., Seger, B., Pedersen, T., Yao, T., Ding, C., Shi, J., Chen, J. & Li, C. Integrating a dual-silicon photoelectrochemical cell into a redox flow battery for unassisted photocharging. *Nat. Commun.* **7**, 11474-11478 (2016).

17. Li, W., Fu, H.-C., Li, L., Caban-Acevedo, M., He, J.-H. & Jin, S. Integrated photoelectrochemical solar energy conversion and organic redox flow battery devices. *Angew. Chem. Int. Ed.* **55**, 13104-13108 (2016).

18. Ding, Y. & Yu, G. A Bio-Inspired, Heavy-Metal-Free, Dual-Electrolyte Liquid Battery towards Sustainable Energy Storage. *Angew. Chem. Int. Ed.* **55**, 4772-4776 (2016).

19. Wedege, K., Azevedo, J., Khataee, A., Bentien, A. & Mendes, A. Direct solar charging of an organic-inorganic, stable, and aqueous alkaline redox flow battery with a hematite photoanode. *Angew. Chem. Int. Ed.* **55**, 7142-7147 (2016).

20. McCulloch, W. D., Yu, M. Z. & Wu, Y. Y. pH-Tuning a Solar Redox Flow Battery for Integrated Energy Conversion and Storage. *ACS Energy Lett.* **1**, 578-582 (2016).

21. Cheng, Q., Fan, W., He, Y., Ma, P., Vanka, S., Fan, S., Mi, Z. & Wang, D. Photorechargeable high voltage redox battery enabled by Ta_3N_5 and GaN/Si dual-photoelectrode. *Adv. Mater.* **351**, 1700312-1700318 (2017).

22. McKone, J. R., DiSalvo, F. J. & Abruna, H. D. Solar energy conversion, storage, and release using an integrated solar-driven redox flow battery. *J. Mater. Chem. A* **5**, 5362-5372 (2017).

23. Khataee, A., Azevedo, J., Dias, P., Ivanou, D., Drazevic, E., Bentien, A. & Mendes, A. Integrated design of hematite and dye-sensitized solar cell for unbiased solar charging of an organic-inorganic redox flow battery. *Nano Energy* **62**, 832-843 (2019).

24. Urbain, F., Murcia-Lopez, S., Nembhard, N., Vazquez-Galvan, J., Flox, C., Smirnov, V., Welter, K., Andreu, T., Finger, F. & Morante, J. R. Solar vanadium redox-flow battery powered by thin-film silicon photovoltaics for efficient photoelectrochemical energy storage. *J Phys D Appl Phys* **52** (2019).

25. Hu, S., Shaner, M. R., Beardslee, J. A., Lichterman, M., Brunschwig, B. S. & Lewis, N. S. Amorphous TiO_2 coatings stabilize Si, GaAs, and GaP photoanodes for efficient water oxidation. *Science* **344**, 1005-1009 (2014).

26. Verlage, E., Hu, S., Liu, R., Jones, R. J. R., Sun, K., Xiang, C., Lewis, N. S. & Atwater, H. A. A monolithically integrated, intrinsically safe, 10% efficient, solar-driven water-splitting system based on active, stable earth-abundant electrocatalysts in conjunction with tandem III-V light absorbers protected by amorphous TiO_2 films. *Energy Environ. Sci.* **8**, 3166-3172 (2015).

27. Liu, T., Wei, X., Nie, Z., Sprenkle, V. & Wang, W. A total organic aqueous redox flow battery employing a low cost and sustainable methyl viologen anolyte and 4-HO-TEMPO catholyte. *Adv. Energy. Mater.* **6**, 1501449 (2015).

28. Liu, Y., Goulet, M.-A., Tong, L., Liu, Y., Ji, Y., Wu, L., Gordon, R. G., Aziz, M. J., Yang, Z. & Xu, T. A Long Lifetime All-Organic Aqueous Flow Battery Utilizing TMAP-TEMPO Radical. *Chem* **5**, 1861-1870 (2019).

29. Hu, S., Lewis, N. S., Ager, J. W., Yang, J. H., McKone, J. R. & Strandwitz, N. C. Thin-Film Materials for the Protection of Semiconducting Photoelectrodes in Solar-Fuel Generators. *J. Phys. Chem. C* **119**, 24201-24228 (2015).

30. Bae, D., Seger, B., Vesborg, P. C. K., Hansen, O. & Chorkendorff, I. Strategies for stable water splitting via protected photoelectrodes. *Chem. Soc. Rev.* **46**, 1933-1954 (2017).

31. Yu, Y., Zhang, Z., Yin, X., Kvit, A., Liao, Q., Kang, Z., Yan, X., Zhang, Y. & Wang, X. Enhanced photoelectrochemical efficiency and stability using a conformal TiO 2 film on a black silicon photoanode. *Nat. Energy* **2**, 17045 (2017).

32. Beh, E. S., De Porcellinis, D., Gracia, R. L., Xia, K. T., Gordon, R. G. & Aziz, M. J. A Neutral pH Aqueous Organic-Organometallic Redox Flow Battery with Extremely High Capacity Retention. *ACS Energy Lett.* **2**, 639-644 (2017).

33. Seger, B., Pedersen, T., Laursen, A. B., Vesborg, P. C. K., Hansen, O. & Chorkendorff, I. Using TiO_2 as a conductive protective layer for photocathodic H_2 evolution. *J. Am. Chem. Soc.* **135**, 1057-1064 (2013).

34. Shaner, M. R., Hu, S., Sun, K. & Lewis, N. S. Stabilization of Si microwire arrays for solar-driven H_2O oxidation to O_2(g) in 1.0 M KOH(aq) using conformal coatings of amorphous TiO_2. *Energy Environ. Sci.* **8**, 203-207 (2015).

35. Green, M. A., Dunlop, E. D., Levi, D. H., Hohl-Ebinger, J., Yoshita, M. & Ho-Baillie, A. W. Y. Solar cell efficiency tables (version 54). *Prog Photovoltaics* **27**, 565-575 (2019).

36. Zheng, J. H., Lau, C. F. J., Mehrvarz, H., Ma, F. J., Jiang, Y. J., Deng, X. F., Soeriyadi, A., Kim, J., Zhang, M., Hu, L., Cui, X., Lee, D. S., Bing, J. M., Cho, Y., Chen, C., Green, M. A., Huang, S. J. & Ho-Baillie, A. W. Y. Large area efficient interface layer free monolithic perovskite/homo-junction-silicon tandem solar cell with over 20% efficiency. *Energ Environ Sci* **11**, 2432-2443 (2018).

37. Zheng, J. H., Mehrvarz, H., Ma, F. J., Lau, C. F. J., Green, M. A., Huang, S. J. & Ho-Baillie, A. W. Y. 21.8% Efficient Monolithic Perovskite/Homo-Junction-Silicon Tandem Solar Cell on 16 cm(2). *ACS Energy Lett.* **3**, 2299-2300 (2018).

38. Bush, K. A. *et al.* 23.6%-efficient monolithic perovskite/silicon tandem solar cells with improved stability. *Nat. Energy* **2**, 17009 (2017).

39. Correa-Baena, J. P., Saliba, M., Buonassisi, T., Gratzel, M., Abate, A., Tress, W. & Hagfeldt, A. Promises and challenges of perovskite solar cells. *Science* **358**, 739-744 (2017).

40. Yu, Z. S., Leilaeioun, M. & Holman, Z. Selecting tandem partners for silicon solar cells. *Nat. Energy* **1**, 16137 (2016).

41. Ji, Y., Goulet, M. A., Pollack, D. A., Kwabi, D. G., Jin, S., Porcellinis, D., Kerr, E. F., Gordon, R. G. & Aziz, M. J. A Phosphonate‐Functionalized Quinone Redox Flow Battery at Near‐Neutral pH with Record Capacity Retention Rate. *Adv. Energy. Mater.* **9**, 1900039 (2019).

42. Kwabi, D. G., Lin, K., Ji, Y., Kerr, E. F., Goulet, M.-A., De Porcellinis, D., Tabor, D. P., Pollack, D. A., Aspuru-Guzik, A., Gordon, R. G. & Aziz, M. J. Alkaline Quinone Flow Battery with Long Lifetime at pH 12. *Joule* **2**, 1894-1906 (2018).

43. DeBruler, C., Hu, B., Moss, J., Liu, X., Luo, J., Sun, Y. & Liu, T. L. Designer Two-Electron Storage Viologen Anolyte Materials for Neutral Aqueous Organic Redox Flow Batteries. *Chem* **3**, 961-978 (2017).

44. Luo, J., Hu, B., Debruler, C. & Liu, T. L. A π-Conjugation Extended Viologen as a Two-Electron Storage Anolyte for Total Organic Aqueous Redox Flow Batteries. *Angew. Chem. Int. Ed.* **57**, 231-235 (2018).

45. Hu, B., Tang, Y. J., Luo, J., Grove, G., Guo, Y. S. & Liu, T. L. Improved radical stability of viologen anolytes in aqueous organic redox flow batteries. *Chem Commun* **54**, 6871-6874 (2018).

46. DeBruler, C., Hu, B., Moss, J., Luo, J. & Liu, T. L. A Sulfonate-Functionalized Viologen Enabling Neutral Cation Exchange, Aqueous Organic Redox Flow Batteries toward Renewable Energy Storage. *ACS Energy Lett.* **3**, 663-668 (2018).

47. Park, M., Ryu, J., Wang, W. & Cho, J. Material design and engineering of next-generation flow-battery technologies. *Nat. Rev. Mater.* **2**, 16080-16018 (2016).

48. Ding, Y., Zhang, C., Zhang, L., Zhou, Y. & Yu, G. Molecular engineering of organic electroactive materials for redox flow batteries. *Chem. Soc. Rev.* (2017).

49. Wei, X., Pan, W., Duan, W., Hollas, A., Yang, Z., Li, B., Nie, Z., Liu, J., Reed, D., Wang, W. & Sprenkle, V. Materials and Systems for Organic Redox Flow Batteries: Status and Challenges. *ACS Energy Lett.* **2**, 2187-2204 (2017).

50. Weber, A. Z., Mench, M. M., Meyers, J. P., Ross, P. N., Gostick, J. T. & Liu, Q. Redox flow batteries: A review. *Journal of Applied Electrochemistry* **41**, 1137-1164 (2011).

51. Soloveichik, G. L. Flow Batteries: Current Status and Trends. *Chem. Rev.* **115**, 11533-11558 (2015).

52. Darling, R. M., Gallagher, K. G., Kowalski, J. A., Ha, S. & Brushett, F. R. Pathways to low-cost electrochemical energy storage: a comparison of aqueous and nonaqueous flow batteries. *Energ Environ Sci* **7**, 3459-3477 (2014).

53. Hu, B., DeBruler, C., Rhodes, Z. & Liu, T. L. Long-Cycling Aqueous Organic Redox Flow Battery (AORFB) toward Sustainable and Safe Energy Storage. *J. Am. Chem. Soc.* **139**, 1207-1214 (2017).

54. Goulet, M. A. & Aziz, M. J. Flow Battery Molecular Reactant Stability Determined by Symmetric Cell Cycling Methods. *J. Electrochem. Soc.* **165**, A1466-A1477 (2018).

55. Hu, B., Seefeldt, C., DeBruler, C. & Liu, T. L. Boosting the energy efficiency and power performance of neutral aqueous organic redox flow batteries. *J. Mater. Chem. A* **5**, 22137-22145 (2017).

APPENDIX 1

Supplementary Information for CHAPTER 2: Integrated Photoelectrochemical Solar Energy Conversion and Organic Redox Flow Battery Devices[*]

---

[*] This appendix was originally made available online as supporting information for *Angew. Chem. Int. Ed.* **55**, 13104-13108 (2016), in collaboration with Fu, H.-C., Zhao, Y., He, J.-H. and Jin, S.

A1.1 Supplementary Figures

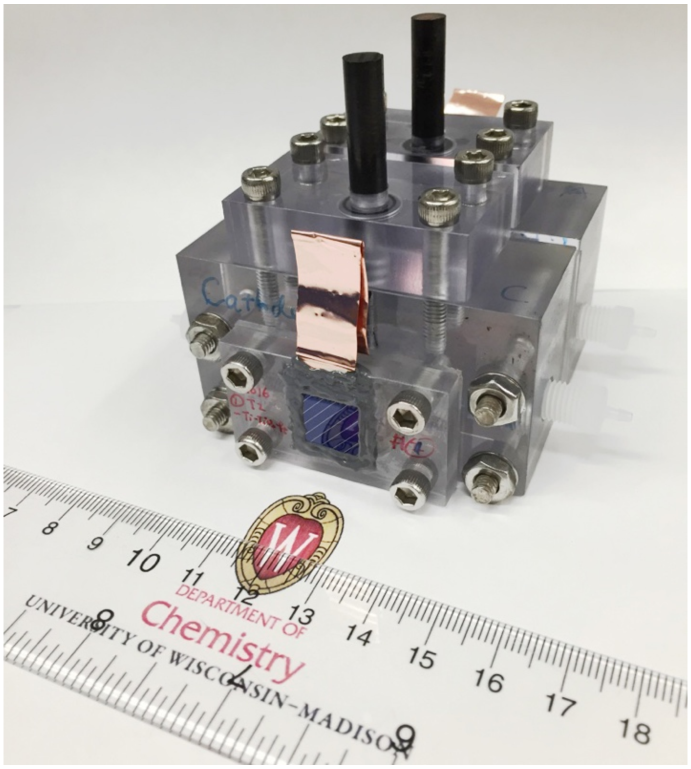

Figure A1.1. A photograph of custom-made integrated PEC-RFB device, which can also be used as a RFB device when the solar cells at both ends are replaced by sealing face plates.

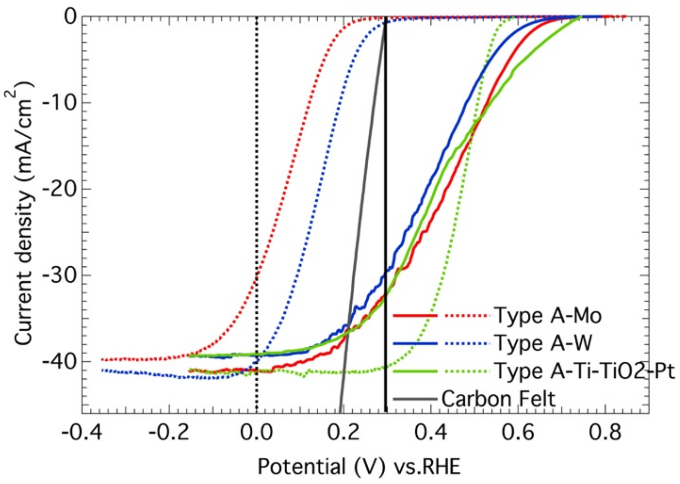

Figure A1.2. J-V data for type A Si photocathode coated by different passivation layers of Pt, W and Mo: solid curve, in 0.1 M AQDS solution; dashed curve, in 1 M H_2SO_4 solution.

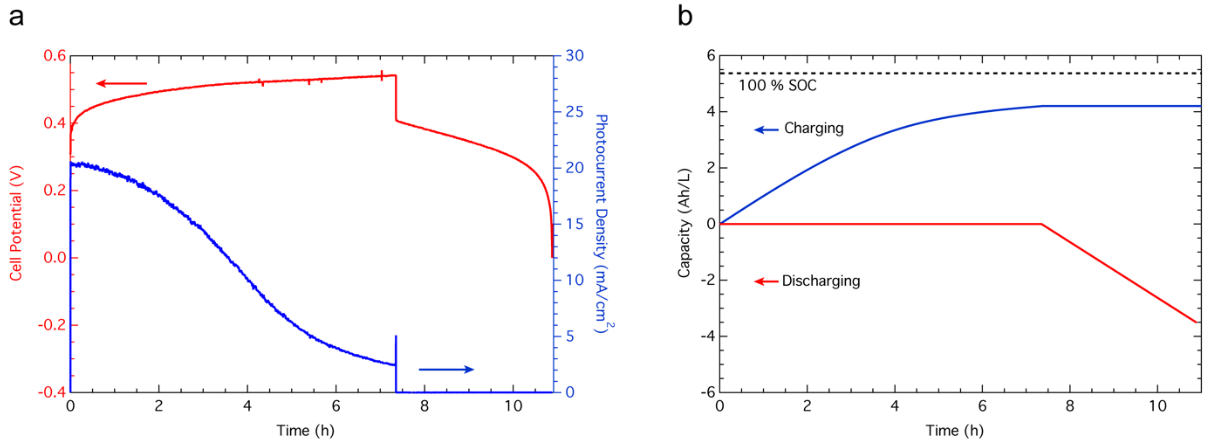

Figure A1.3. Long term unbiased photocharging and constant current discharging test of the integrated PEC-RFB device: (a) cell potential and photocurrent density; (b) charging and discharging capacity.

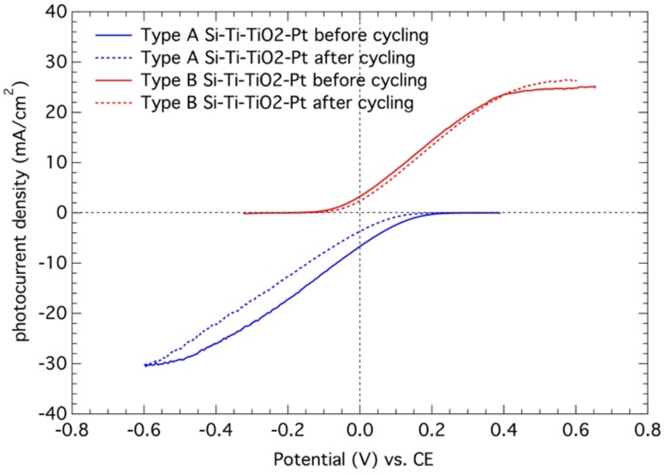

Figure A1.4. J-V data for type A and type B photoelectrodes before and after 10 cycles of integrated device cycling test.

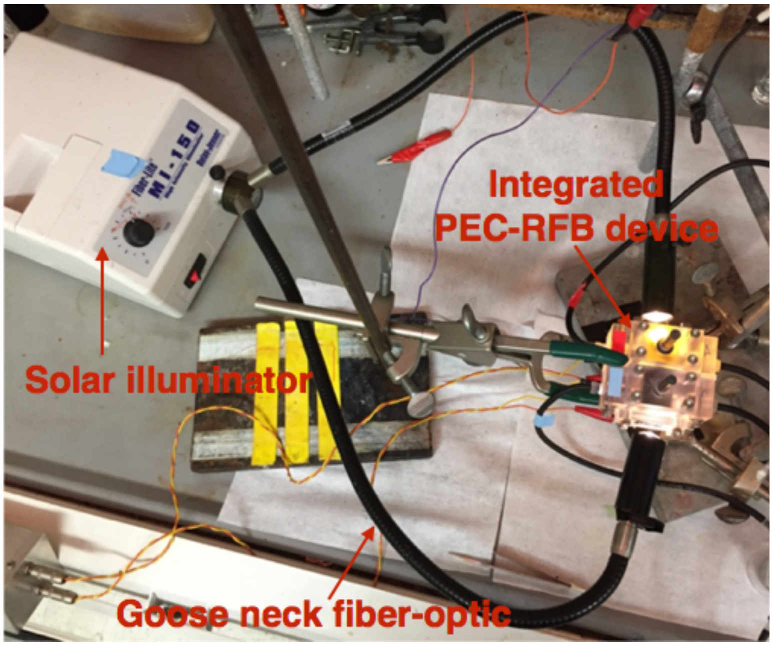

Figure A1.5. A photograph of the dual-side illumination setup using a Fiber-Lite MI-150 illuminator. Two goose neck fiber-optics connected to the light source can split the light from a single EKE-type light source into two beams for dual-side illumination. The illumination intensity of the output beams were calibrated using a silicon photodiode.

APPENDIX 2

Supplementary Information for CHAPTER 3: 14.1%-Efficient Monolithically Integrated Solar Flow Battery [*]

---

[*] This appendix was originally made available online as supporting information for *Chem* **4**, 2644-2657 (2018), in collaboration with Fu, H.-C., Zhao, Y., He, J.-H. and Jin, S.

A2.1 Supplementary Figures

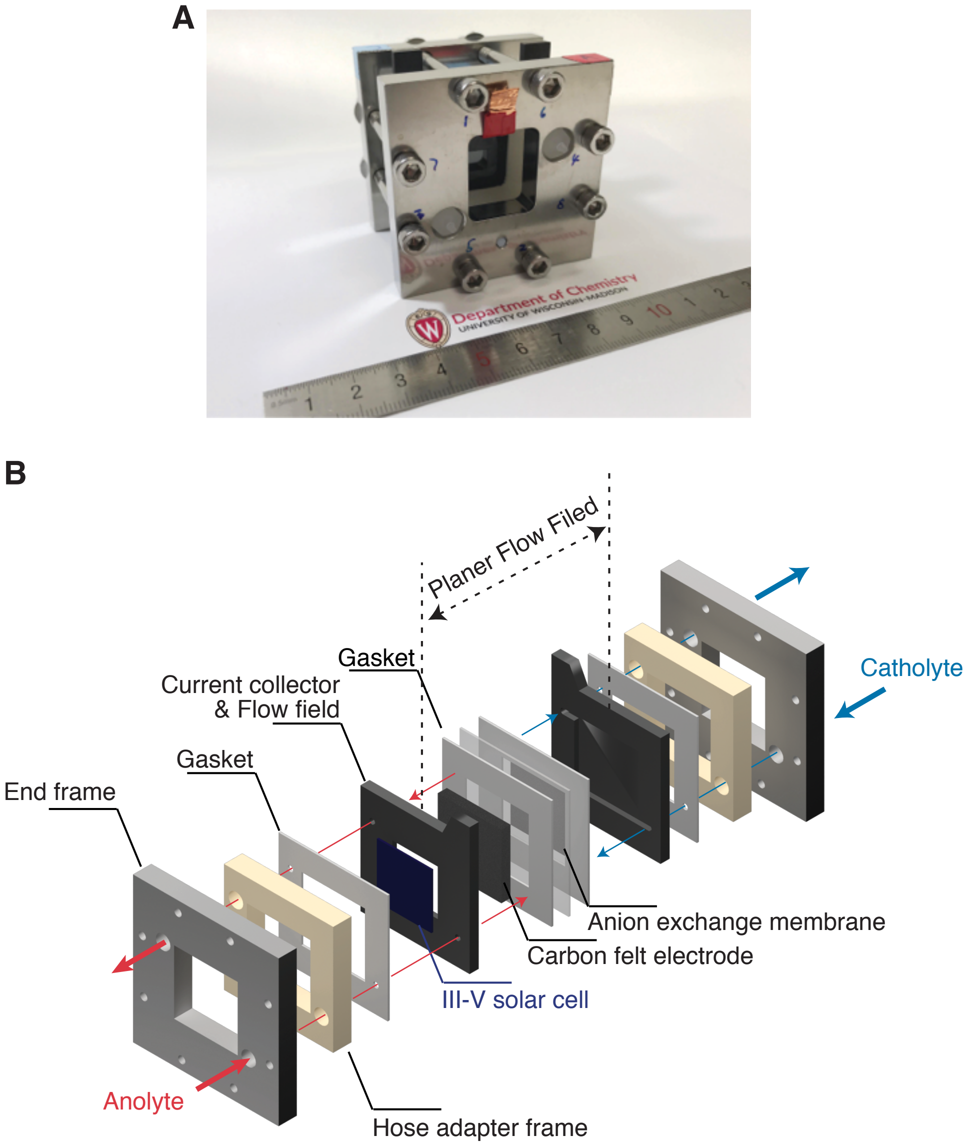

Figure A2.1. Photograph and schematic design of the custom-made integrated SFB device.

a, Cell photo; **b**, exploded-view scheme.

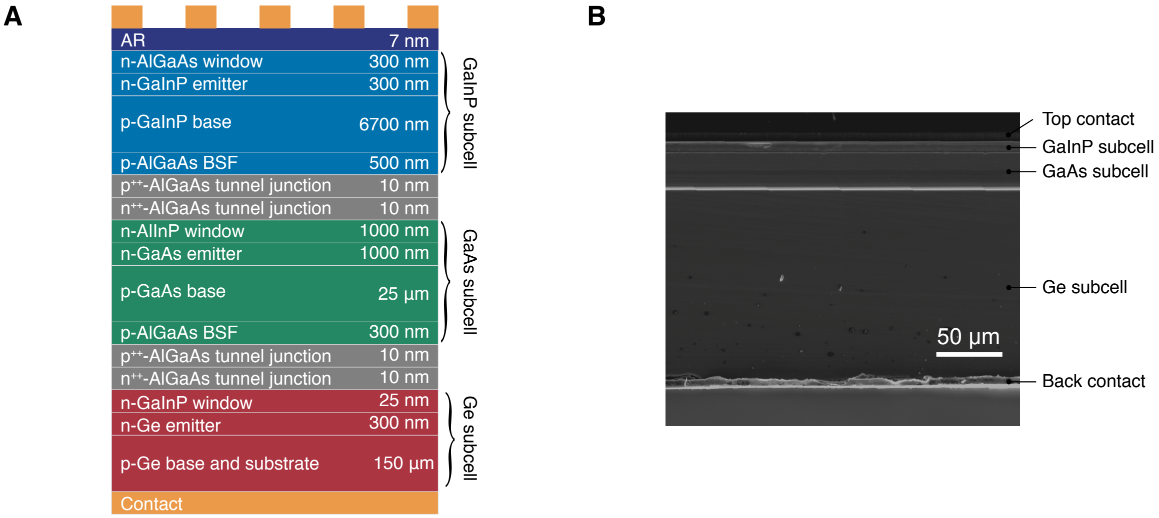

Figure A2.2. Architecture of GaInP/GaAs/Ge tandem junction solar cell. **a**, Schematic illustration; **b**, cross-section SEM image.

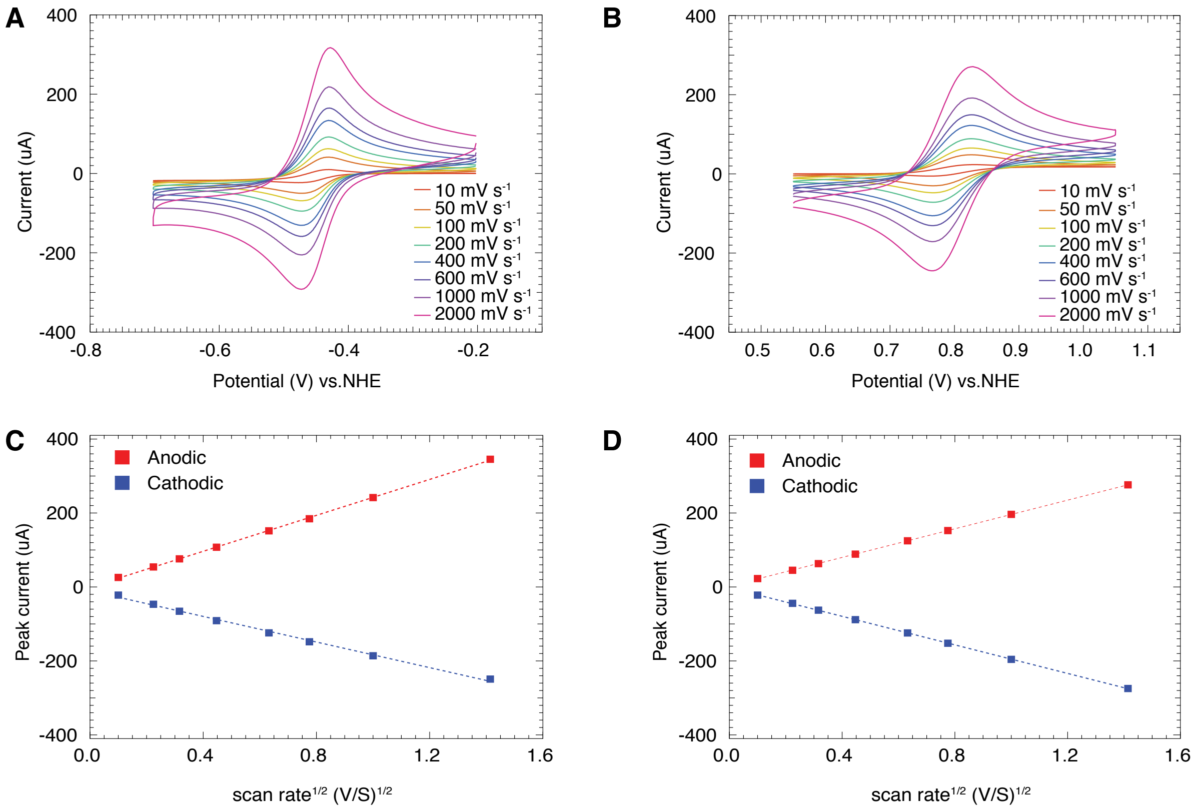

Figure A2.3. Cyclic voltammogram and fit of Randles-Sevèik equation for the two redox couples. **a-b**, Cyclic voltammograms of (**a**) 5 mM $MVCl_2$ and (**b**) 5 mM 4-OH-TEMPO in 2 M NaCl scanned at various scan rates on a glassy carbon electrode. **c-d**, Plots of peak current over the square root of scan rates for (**c**) 5 mM $MVCl_2$ and (D) 5 mM 4-OH-TEMPO to extract the diffusion coefficients (*D*).

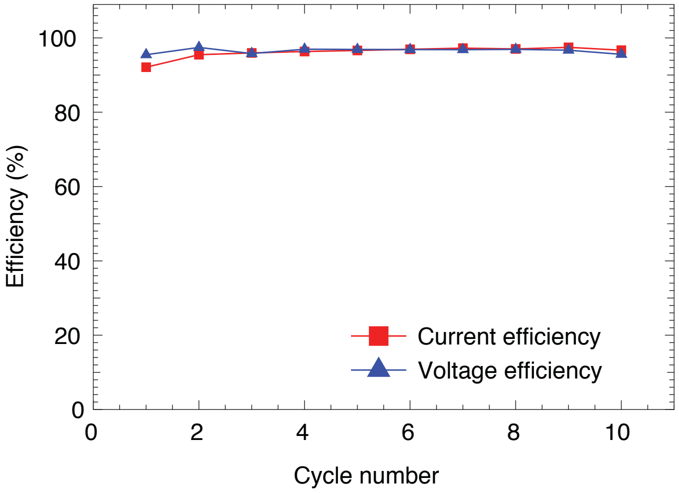

Figure A2.4. Current and voltage efficiency of SFB device. Representative cycling efficiency plots of the integrated SFB device: current efficiency (red) and voltage efficiency (blue).

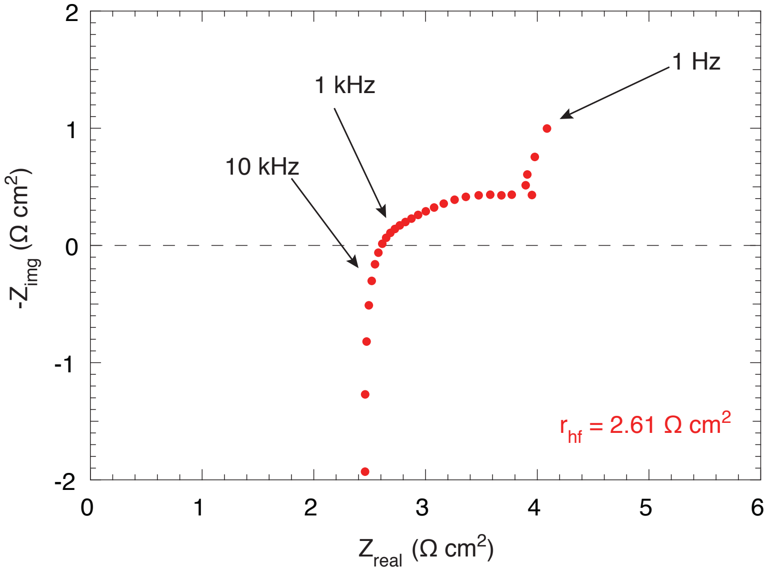

Figure A2.5. Electrochemical Impedance Spectroscopy (EIS). EIS of the RFB device was measured to study the overall resistance of the device. The high frequency area-specific resistance (r_{hf}) was estimated by finding the horizontal intercept of the impedance curve in Nyquist plot.

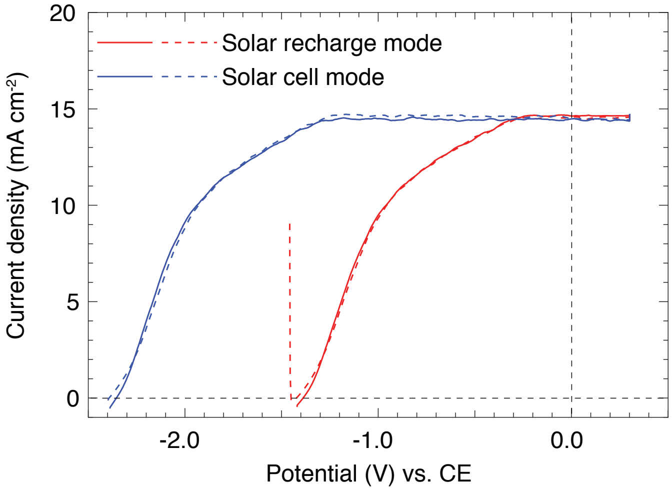

Figure A2.6. Stability of the photoelectrodes. J-V curves of the InGaP/GaAs/Ge photoelectrode used for integrated SFB device cycling test before (solid line) and after (dashed line) 10 charging-discharging cycles.

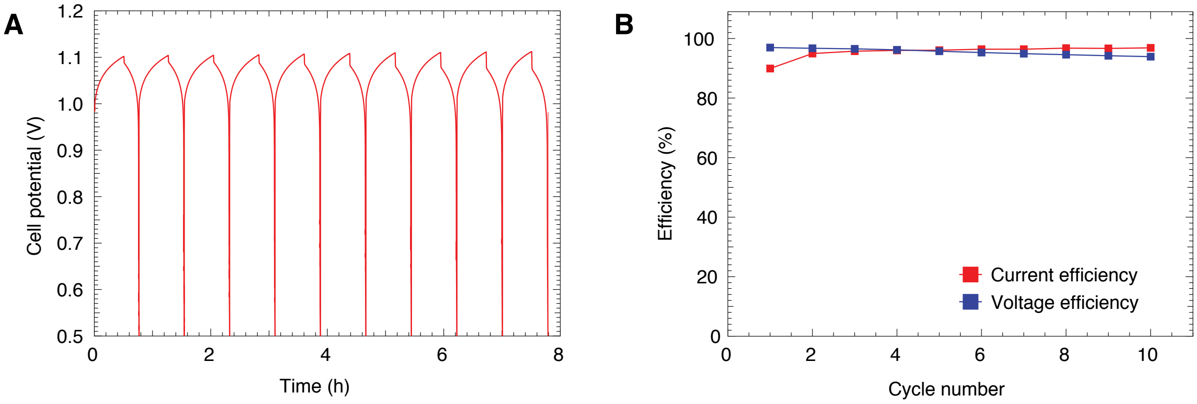

Figure A2.7. RFB cycling performance under similar operation conditions to SFB cycling tests. a-b, Voltage profile (**a**) and device efficiency (**b**) of 0.1 M 4-OH-TEMPO/0.1 M $MVCl_2$ RFB during 10 charge-discharge cycles. Charging current, 5.6 mA; charging time, 30 min; potential limits, 0.5-1.5 V.

A2.2 Supplementary Table

Table A2.1. SOEE of representative early demonstrations of integrated solar rechargeable battery and recent demonstrations of solar flow batteries (SFBs)

Year	Photoelectrode	Redox species	Photovoltage at open circuit (V)	Cell voltage (V)[a]	*SOEE* (%)[b]
Early demonstrations of integrated solar rechargeable battery					
1976[1]	CdSe	Ag/Ag_2S, S^{2-}/S	0.45-0.56	0.24	<1.2[c]
1987[2]	Cd(Se,Te)	Sn/SnS, polysulfide	~0.65	0. 48	11.3[d]
Recent demonstrations of SFBs					
2013[3]	TiO_2-dye (DSSC)	$DMFc^{0/+}$, I^-/I^{3-}	<0.7	0.7	0.05[e]
2015[4]	TiO_2-Z907 dye (DSSC)	Li/Li^+, I^-/I^{3-}	~0.52	3.5	<0.35[f]
2016[5]	n/p Si PV*2	$AQDSH_2/AQDS$, Br^-/Br^{3-}	1.0	0.89	3.2[e]
2016[6]	n/p Si PV*2	$AQDSH_2/AQDS$, $BQDSH_2/BQDS$	1.1	0.45	1.7[e]
2016[7]	α-Fe_2O_3	$AQDSH_2/AQDS$, $Fe(CN)_6^{4-/3-}$	~0.60	0.74	<0.08[c]
2017[8]	Ta_3N_5, GaN-n/p Si PV	$DHAQH_2/DHAQ$, $Fe(CN)_6^{4-/3-}$	1.4	1.2	<3.0[c]
2018[9]	n/p Si PV	$Fe(CN)_6^{4-/3-}$, $[TEMPO\text{-}sulfate]^{0/+}$	0.52	0.35	<1.6[g]
2018[10]	WO_3-$BiVO_4$	I^-/I^{3-}, Br^-/Br^{3-}	~1.0	0.55	1.25[e]
This work	InGaP/GaAs/ Ge PV	$MV^{+/2+}$, $[4\text{-}OH\text{-}TEMPO]^{0/+}$	2.41	1.25	14.1[e]

[a] The cell voltage is calculated from formal potential difference between anodic and cathodic redox reactions, which is usually close to the open circuit voltage of the energy storage device at 50% state-of-charge (SOC). Some of the works shown only utilize a small portion of the total capacity at low SOC range, resulting in a lower actual cell voltage based on Nernst equation.

[b] The solar-to-output electricity efficiency (*SOEE*) defined in this work (equation 1 in the main text) represents the round-trip efficiency of the integrated device from solar energy conversion to delivery. Some works only show the linear scan voltammogram curve of the photoelectrode with certain redox species, thus the SOEE can only be estimated from the power conversion efficiency (*PCE*) of the photoelectrode. Some other works only show photocharging process without actually discharge the SFB, which can only produce solar-to-chemical energy conversion efficiency. In both cases, the actual SOEE for the round-trip process would be smaller than the estimated *SOEE* numbers shown in the table.

[c] *SOEE* is estimated from the PCE of the photoelectrode.

[d] *SOEE* is estimated from the PCE of the photoelectrode and the voltage efficiency of the battery.

[e] *SOEE* is calculated based on equation 1 in main text.

[f] This device requires external bias to charge to device. SOEE is estimated from external voltage difference between pure electrical charging and photo-assisted charging process, and the charging current.

[g] *SOEE* is estimated from solar-to-chemical energy conversion efficiency without considering the discharging process.

A2.3 References

1. Hodes, G., Manassen, J. & Cahen, D. Photoelectrochemical energy conversion and storage using polycrystalline chalcogenide electrodes. *Nature* **261**, 403-404 (1976).

2. Licht, S., Hodes, G., Tenne, R. & Manassen, J. A light-variation insensitive high efficiency solar cell. *Nature* **326**, 863-864 (1987).

3. Liu, P. *et al.* A Solar Rechargeable Flow Battery Based on Photoregeneration of Two Soluble Redox Couples. *ChemSusChem* **6**, 802-806 (2013).

4. Yu, M. *et al.* Aqueous lithium-iodine solar flow battery for the simultaneous conversion and storage of solar energy. *J. Am. Chem. Soc.* **137**, 8332-8335 (2015).

5. Liao, S. *et al.* Integrating a dual-silicon photoelectrochemical cell into a redox flow battery for unassisted photocharging. *Nat. Commun.* **7**, 11474-11478 (2016).

6. Li, W. *et al.* Integrated photoelectrochemical solar energy conversion and organic redox flow battery devices. *Angew. Chem. Int. Ed.* **55**, 13104-13108 (2016).

7. Wedege, K., Azevedo, J., Khataee, A., Bentien, A. & Mendes, A. Direct solar charging of an organic-inorganic, stable, and aqueous alkaline redox flow battery with a hematite photoanode. *Angew. Chem. Int. Ed.* **55**, 7142-7147 (2016).

8. Cheng, Q. *et al.* Photorechargeable high voltage redox battery enabled by Ta_3N_5 and GaN/Si dual-photoelectrode. *Adv. Mater.* **351**, 1700312-1700318 (2017).

9. Wedege, K. *et al.* Unbiased, complete solar charging of a neutral flow battery by a single Si photocathode. *RSC Advances* **8**, 6331-6340 (2018).

10. Zhou, Y. *et al.* Efficient Solar Energy Harvesting and Storage through a Robust Photocatalyst Driving Reversible Redox Reactions. *Adv. Mater.* **103**, 1802294-1802297 (2018).

APPENDIX 3

Supplementary Information for CHAPTER 4: A Long Lifetime Aqueous Organic Solar Flow Battery [*]

---

[*] This appendix was originally made available online as supporting information for *Adv. Energy. Mater.* **9**, 1900918 (2019), in collaboration with Kerr, E., Goulet, M.-A., Fu, H.-C., Zhao, Y., Yang, Y., Veyssal, A., He, J.-H., Gordon, R. G., Aziz, M. J. and Jin, S.

A3.1 Supplementary Table

Table A3.1. SOEE and lifetime of representative early demonstrations of integrated solar rechargeable battery and recent demonstrations of solar flow batteries (SFBs)

Year	Photoelectrode	Redox species	Photovoltage at open circuit (V)	Cell voltage (V)*	*SOEE* (%)*	Continuous cycling time (h)
Early demonstrations of integrated solar rechargeable battery						
1976[1]	CdSe	Ag/Ag_2S, S^{2-}/S	0.45-0.56	0.24	<1.2[c]	15
1987[2]	Cd(Se,Te)	Sn/SnS, polysulfide	~0.65	0. 48	11.3[d]	48
Recent demonstrations of SFBs						
2013[3]	TiO_2-dye (DSSC)	$DMFc^{0/+}$, I^-/I_3^-	<0.7	0.7	0.05	~20
2015[4]	TiO_2-Z907 dye (DSSC)	Li/Li^+, I^-/I_3^-	~0.52	3.5	<0.35	29.2
2016[5]	n/p Si PV×2	$AQDSH_2/AQDS$, Br^-/Br_3^-	1.0	0.89	3.2	~10
2016[6]	n/p Si PV×2	$AQDSH_2/AQDS$, $BQDSH_2/BQDS$	1.1	0.45	1.7	10
2016[7]	α-Fe_2O_3	$AQDSH_2/AQDS$, $Fe(CN)_6^{4-/3-}$	~0.60	0.74	<0.08	n/a
2017[8]	Ta_3N_5, GaN-n/p Si PV	$DHAQH_2/DHAQ$, $Fe(CN)_6^{4-/3-}$	1.4	1.2	<3.0	~10
2018[9]	n/p Si PV	$Fe(CN)_6^{4-/3-}$, $[TEMPO\text{-}sulfate]^{0/+}$	0.52	0.35	<1.6	7
2018[10]	WO_3-$BiVO_4$	I^-/I_3^-, Br^-/Br_3^-	~1.0	0.55	1.25	>20
2018[11]	InGaP/GaAs/Ge PV	$MV^{+/2+}$, $[4\text{-}OH\text{-}TEMPO]^{0/+}$	2.41	1.25	14.1	8
This work	n/p Si PV×2	$BTMAP\text{-}Vi^{3+/4+}$, $BTMAP\text{-}Fc^{2+/3+}$	1.09	0.735	5.4	200

* Cell voltage and *SOEE* data are adopted from a previous paper.[11]

A3.2 Supplementary Figures

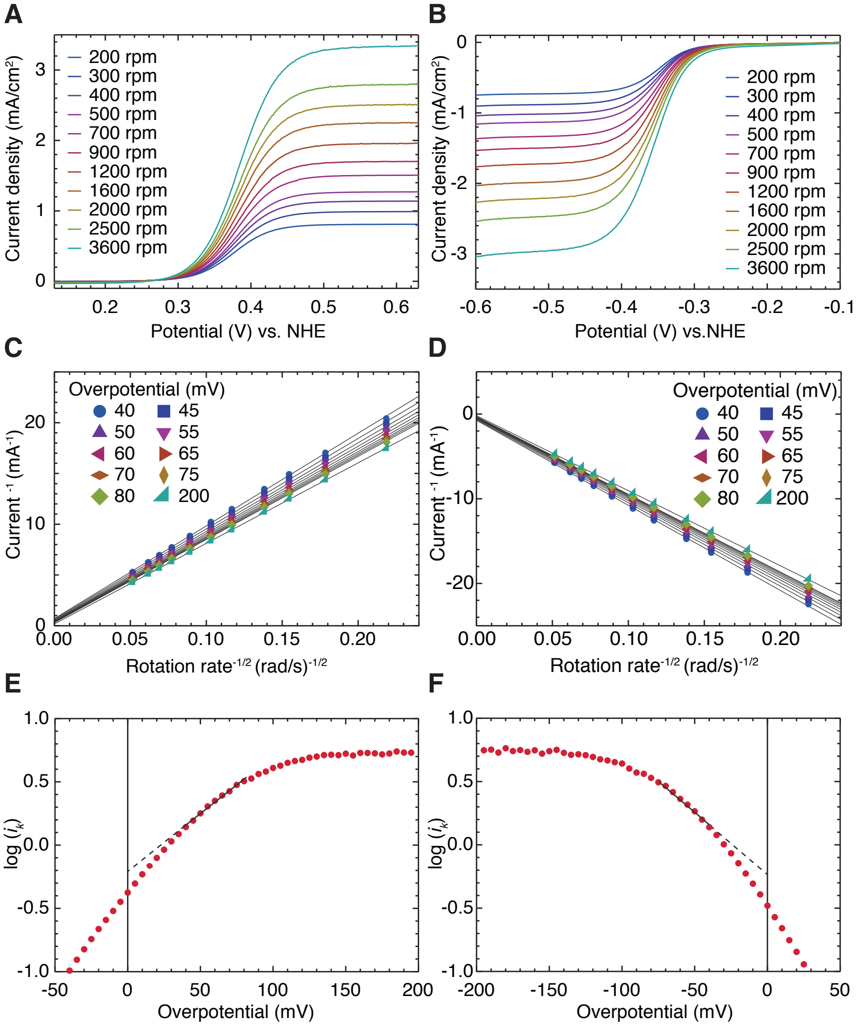

Figure A3.1. Rotating disk electrode (RDE) characterization of BTMAP redox couples. LSV curves of 5.0 mM BTMAP-Fc (**a**) and 5.0 mM BTMAP-Vi (**b**) in 1.0 M NaCl with a 3.0 mm diameter glassy carbon working electrode rotating at different rates. **c-d**, Koutecký–Levich plots derived from (**a-b**) by extracting disk current at different overpotentials (η). Kinetic current (i_k) can be found by extrapolating the fitted $1/i$ *vs.* $\omega^{-1/2}$ lines to $\omega^{-1/2} = 0$. The slopes at $\eta = 200$ mV were used to calculate the diffusion coefficients of BTMAP-Fc and BTMAP-Vi based on the Levich equation. For BTMAP-Fc, $D_R = 5.3 \times 10^{-6}$ cm^2/s; for BTMAP-Vi, $D_O = 4.8 \times 10^{-6}$ cm^2/s.

(E-F) Tafel plots of BTMAP-Fc (**e**) and BTMAP-Vi (**f**). The absolute overpotential ($|\eta|$) region between 40-80 mV was linearly fitted to calculate the standard rate constant (k_0) and transfer coefficient (α) based on the Butler-Volmer equation. For BTMAP-Fc, $k_0 = 1.8 \times 10^{-2}$ cm/s and $\alpha = 0.47$; for BTMAP-Vi, $k_0 = 1.6 \times 10^{-2}$ cm/s and $\alpha = 0.49$.

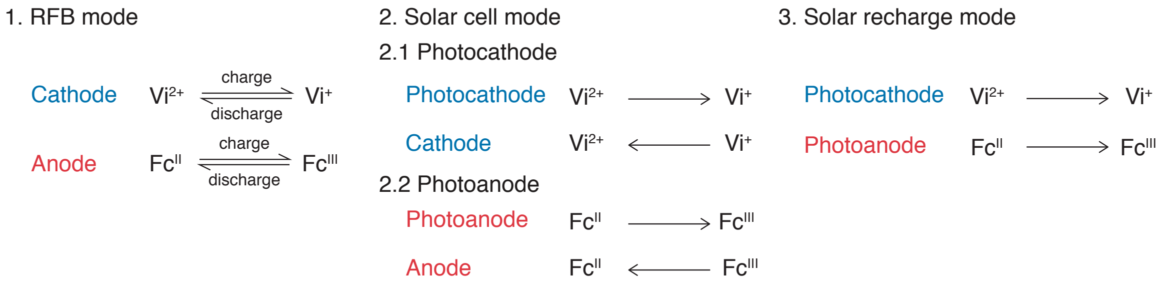

Scheme A3.1. Operation principles and reactions under different operation modes. Under RFB mode, the SFB device can be charged and discharged by a potentiostat like a normal RFB device to store and redeliver electrical energy on demand. Under solar cell mode, the photoelectrode is paired with carbon felt electrode in the same cell chamber to turn over and regenerate one pair of redox couple (BTMAP-Vi or BTMAP-Fc) and directly produce electricity. Both photoanode and photocathode can be operated independently under this mode. Under solar recharge mode, photoanode and photocathode are connected in series to store converted solar energy as chemical energy by creating an electrochemical bias between the two BTMAP redox couples.

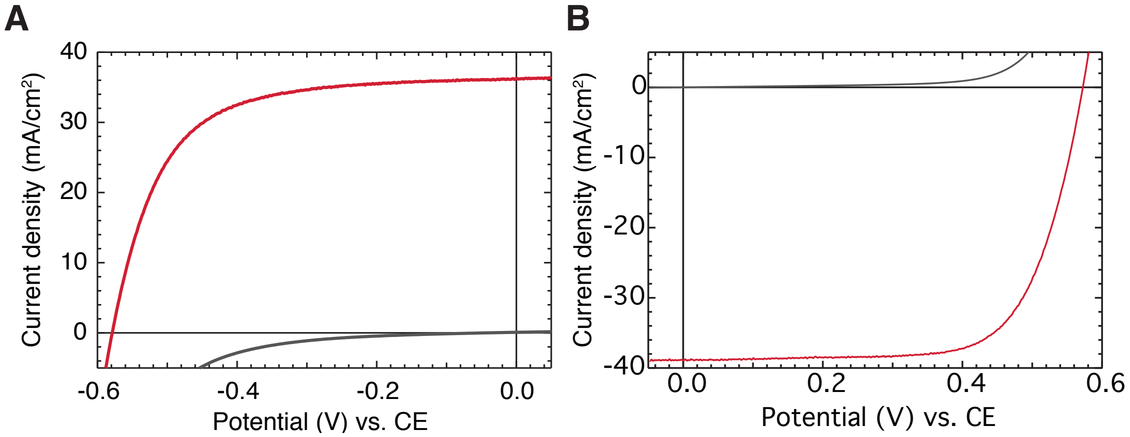

Figure A3.2. *J-V* performance of the solid-state silicon solar cells under 1 sun (AM 1.5 G) illumination (red) and in the dark (gray): (A) n^+np^+ silicon cell, used to fabricate photoanode, with a power conversion efficiency of 13.5%; (B) p^+nn^+ silicon cell, used to fabricate photocathode, with a power conversion efficiency of 15.6%.

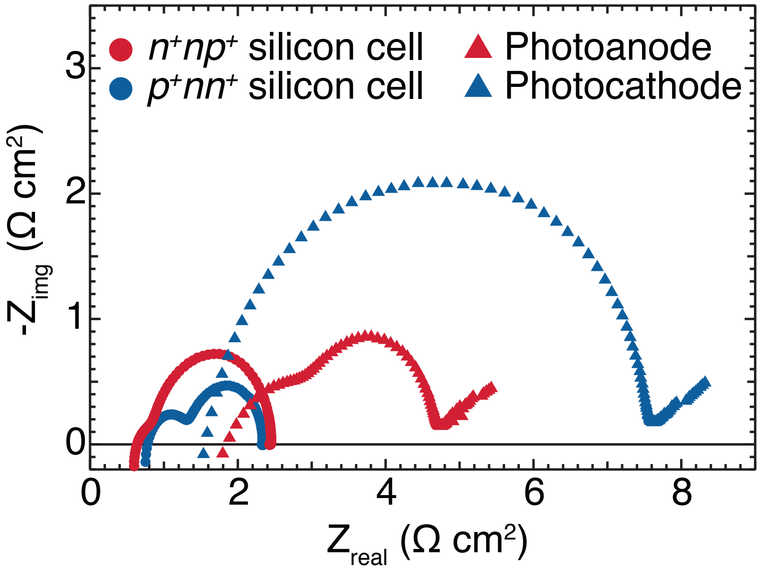

Figure A3.3. Potentiostatic electrochemical impedance spectroscopy (EIS) of the solid state cells and photoelectrodes measured under an illumination intensity of 100 mW/cm^2 (1 Sun) at open circuit voltage. Photoelectrodes are characterized individually under solar cell mode.

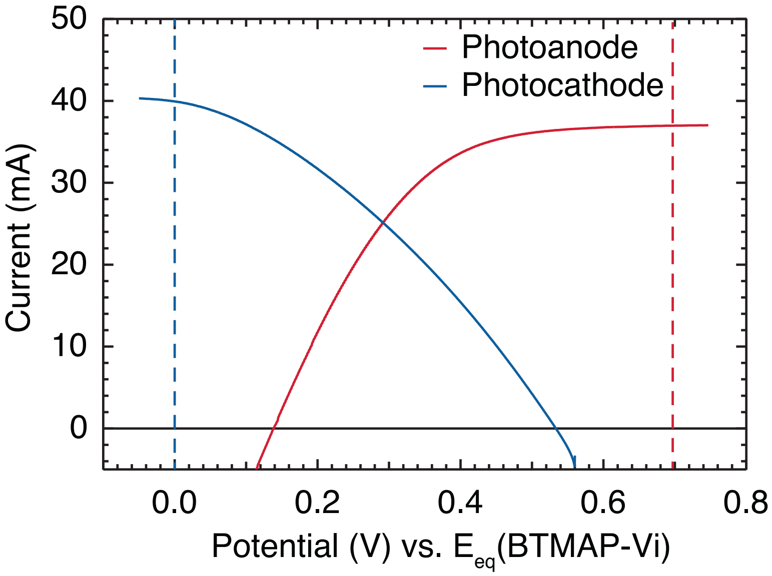

Figure A3.4. Overlaid *J-V* curve for the photoanode and photocathode measured under solar cell mode. Dashed lines showed the equilibrium potentials (E_{eq}) of BTMAP-Fc (red) and BTMAP-Vi (blue) with respect to the E_{eq} of BTMAP-Vi at 50% SOC. Because these *J-V* measurements were carried out with the 2-electrode set-up, the exact potential with respect to SHE cannot be accurately determined. The intersection of the two *J-V* curves shows the operating point of the photoelectrode at current SOC.

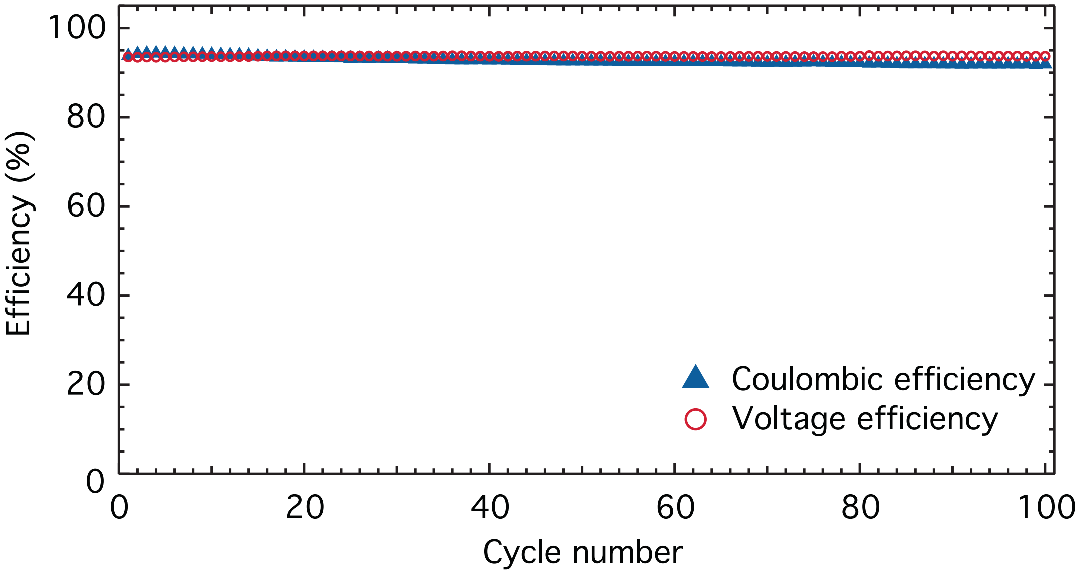

Figure A3.5. Cycling efficiency plots of the integrated SFB device: coulombic efficiency (blue triangles) and voltage efficiency (red circles).

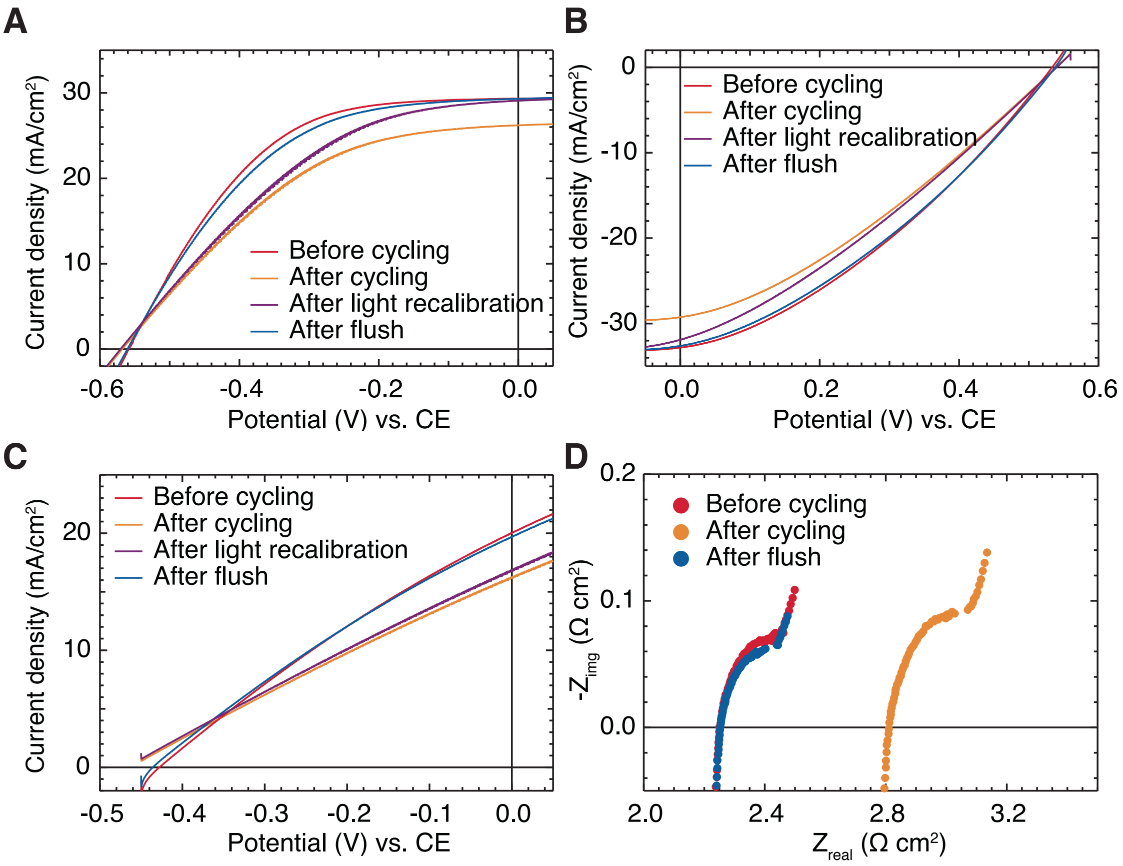

Figure A3.6. Characterization of the SFB device after long term cycling test. The SOEE drop is mainly caused by two reasons: first, slow decay of illumination intensity of the light source from 1 sun (before cycling) to 0.90 sun (after cycling) over 200 h of continues operation; second, bubble accumulation in the SFB chamber, blocking active surface area of photoelectrodes and graphite felt electrodes. After replacing the light bulb, recalibrating the illumination intensity and flushing the SFB at a high flow rate of 130 mL/min (MPM) for 5 mins, the solar performance can be almost fully recovered. *J*-*V* performance of the photoanode (**a**) and photocathode (**b**), measured individually under solar cell mode at different stage of the whole set of tests. (**c**) *J*-*V* performance of the photoanode and photocathode connected in series, measured under solar recharge mode at different stage of the whole set of tests. (**d**) Potentiostatic EIS measured between two RFB current collectors shows significant increase in r_{hf} after the cycling test, which can be completely restored to the original value after a simple flushing process. This proved the hypothesis of bubble accumulation in the SFB cell during cycling test.

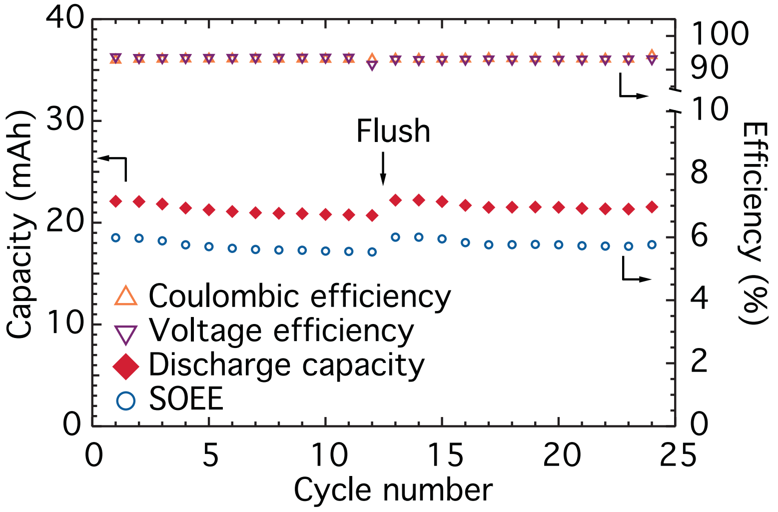

Figure A3.7. Cycling performance of the integrated SFB device with increased flow rate at 10 cycles intervals. The SFB device was flushed using 130 MPM for 5 min at the end of the 12th cycle. The cycling profile shows that the performance of the SFB device can be easily restored with this quick flush procedure, indicating the slight SFB performance decay could be avoided with better flow management and device engineering.

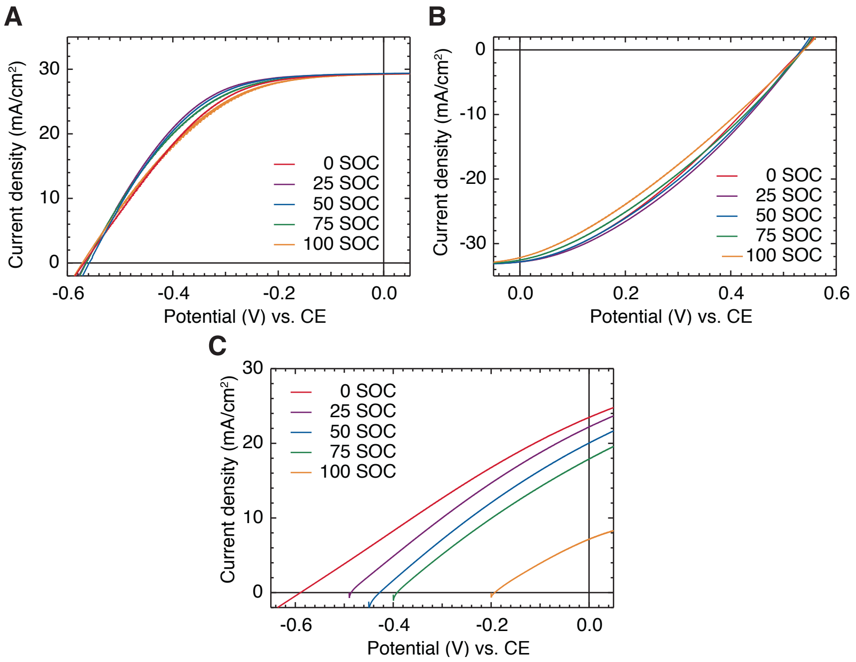

Figure A3.8. Solar performance of the photoelectrode at different SOCs. To perform the measurements at different SOCs, the SFB was first discharged to 0% SOC and then charged to the desired SOC level using potentiostat to avoid the influence of *J-V* measurements on SOC. *J-V* performance of the photoanode (A) and photocathode (B), measured individually under solar cell mode at 20 MPM. Although the overall solar performance of the individual photoelectrodes are rather insensitive to the SOC changes, the change of fill factor (*FF*) at different SOCs is quite distinguishable. Both photoelectrodes show the best *FF* at 25% SOC and worst *FF* at 100% SOC. (C) *J-V* performance of the photoanode and photocathode connected in series, measured under solar recharge mode at 20 MPM. The overall solar performance under solar recharge mode changed significantly at different SOCs, as illustrated in Figure 4.

A3.3 References

1. Hodes, G., Manassen, J. & Cahen, D. Photoelectrochemical energy conversion and storage using polycrystalline chalcogenide electrodes. *Nature* **261**, 403-404 (1976).

2. Licht, S., Hodes, G., Tenne, R. & Manassen, J. A light-variation insensitive high efficiency solar cell. *Nature* **326**, 863-864 (1987).

3. Liu, P., Cao, Y. l., Li, G. R., Gao, X. P., Ai, X. P. & Yang, H. X. A Solar Rechargeable Flow Battery Based on Photoregeneration of Two Soluble Redox Couples. *Chemsuschem* **6**, 802-806 (2013).

4. Yu, M., McCulloch, W. D., Beauchamp, D. R., Huang, Z., Ren, X. & Wu, Y. Aqueous lithium-iodine solar flow battery for the simultaneous conversion and storage of solar energy. *J. Am. Chem. Soc.* **137**, 8332-8335 (2015).

5. Liao, S., Zong, X., Seger, B., Pedersen, T., Yao, T., Ding, C., Shi, J., Chen, J. & Li, C. Integrating a dual-silicon photoelectrochemical cell into a redox flow battery for unassisted photocharging. *Nat. Commun.* **7**, 11474-11478 (2016).

6. Li, W., Fu, H.-C., Li, L., Caban-Acevedo, M., He, J.-H. & Jin, S. Integrated photoelectrochemical solar energy conversion and organic redox flow battery devices. *Angew. Chem. Int. Ed.* **55**, 13104-13108 (2016).

7. Wedege, K., Azevedo, J., Khataee, A., Bentien, A. & Mendes, A. Direct solar charging of an organic-inorganic, stable, and aqueous alkaline redox flow battery with a hematite photoanode. *Angew. Chem. Int. Ed.* **55**, 7142-7147 (2016).

8. Cheng, Q., Fan, W., He, Y., Ma, P., Vanka, S., Fan, S., Mi, Z. & Wang, D. Photorechargeable high voltage redox battery enabled by Ta_3N_5 and GaN/Si dual-photoelectrode. *Adv. Mater.* **351**, 1700312-1700318 (2017).

9. Wedege, K., Bae, D., Dražević, E., Mendes, A., Vesborg, P. C. K. & Bentien, A. Unbiased, complete solar charging of a neutral flow battery by a single Si photocathode. *RSC Adv.* **8**, 6331-6340 (2018).

10. Zhou, Y., Zhang, S., Ding, Y., Zhang, L., Zhang, C., Zhang, X., Zhao, Y. & Yu, G. Efficient Solar Energy Harvesting and Storage through a Robust Photocatalyst Driving Reversible Redox Reactions. *Adv. Mater.* **103**, 1802294-1802297 (2018).

11. Li, W., Fu, H.-C., Zhao, Y., He, J.-H. & Jin, S. 14.1% Efficient Monolithically Integrated Solar Flow Battery. *Chem* **4**, 2644-2657 (2018).

APPENDIX 4

Supplementary Information for CHAPTER 5: Perovskite/Silicon Tandem Solar Cell Powered High Performance Solar Flow Battery [*]

---

[*] This appendix is the supplementary information for a manuscript to be submitted, in collaboration with Zheng, J., Hu, B., Fu, H.-C., Zhao, Y., He, J.-H., Liu, T. L., Ho-Baillie, A. and Jin, S.

A4.1 Supplementary Figures

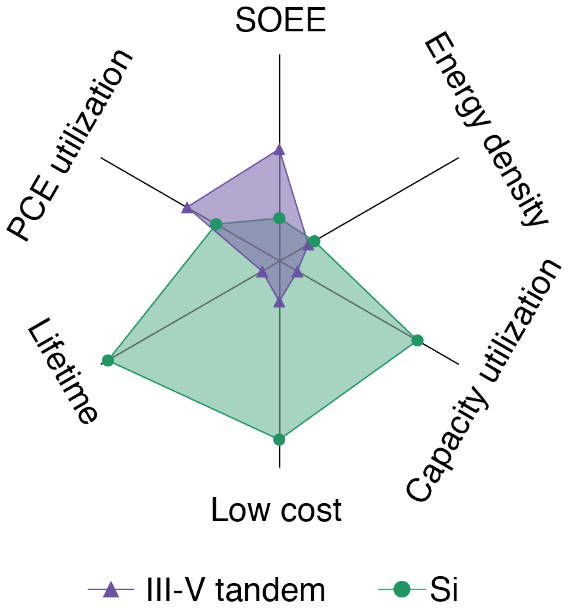

Figure A4.1. Comparison of SFBs in a multivariate radar chart. The figure shows itemized comparison of two previously reported SFBs. The axis limits are stetted to 25%, 100%, 200 h, 100%, 10 Wh L^{-1} for SOEE, PCE utilization, lifetime, capacity utilization, and energy density, respectively. The cost of each SFB was qualitatively estimated based on the manufacture cost of solar cells since the cost for organic electrolytes and other parts were believed to be similar for these two SFBs. The chart reveals that both SFB can only cover a few performance dimensions well, leaving obvious drawbacks in other dimensions.

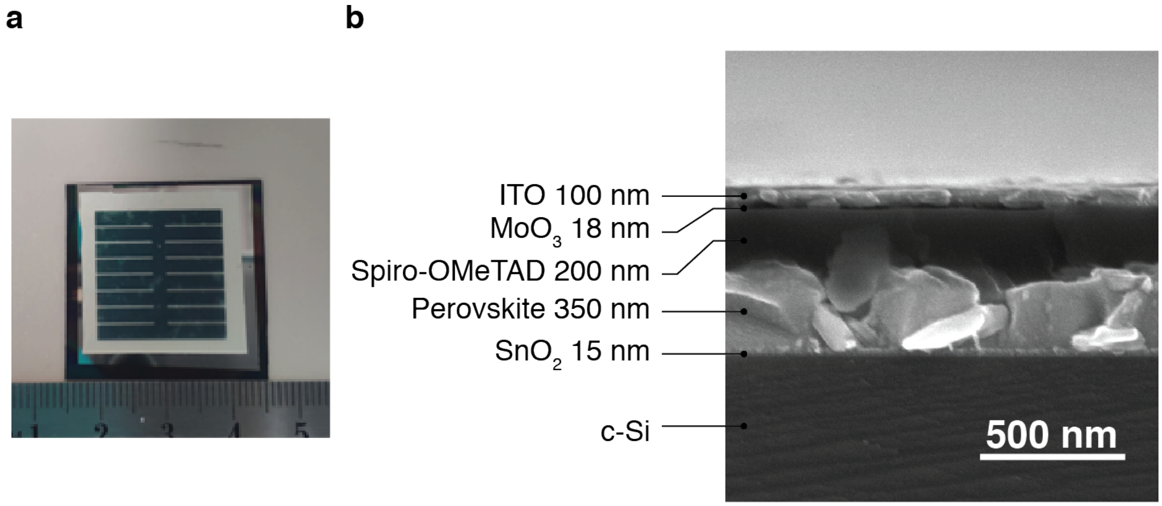

Figure A4.2. Photograph and scanning electron microscopy (SEM) image of perovskite/Si tandem junction solar cell. a, Photo of the perovskite/Si cell (front view). **b,** Cross-sectional SEM image of the perovskite/Si cell.

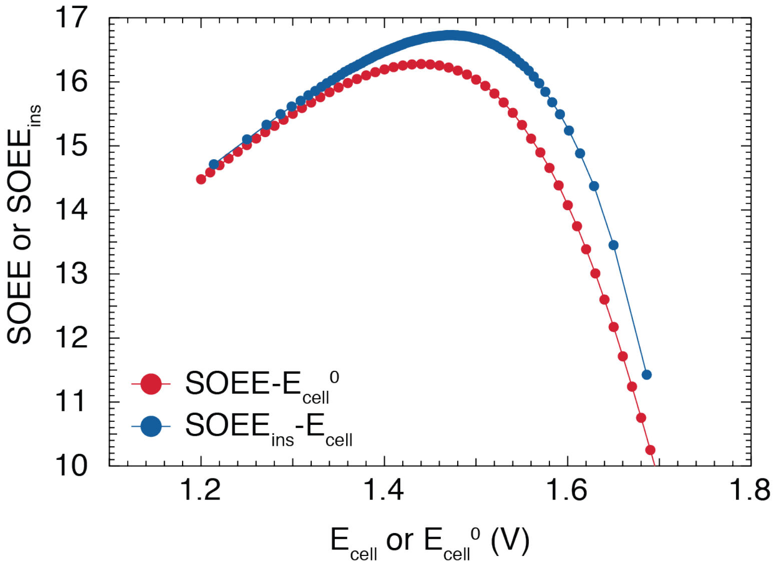

Figure A4.3. Overlaid *SOEE-*E_{cell}^0 and *SOEE*$_{ins}$*-*E_{cell} curves. Although look similar, these two curves show complete different information. *SOEE-*E_{cell}^0 curve can be seen as an weighted moving average of *SOEE*$_{ins}$*-*E_{cell} and the sample window is determined by E_{cell} at 0% and 100% SOC. Note that owing to the non-linear relationship between E_{cell} and SOC, calculating the integral average of *SOEE*$_{ins}$ with respect to E_{cell} would result in a different value from the overall *SOEE* calculated from *SOEE*$_{ins}$-SOC relationship and thus should be avoided.

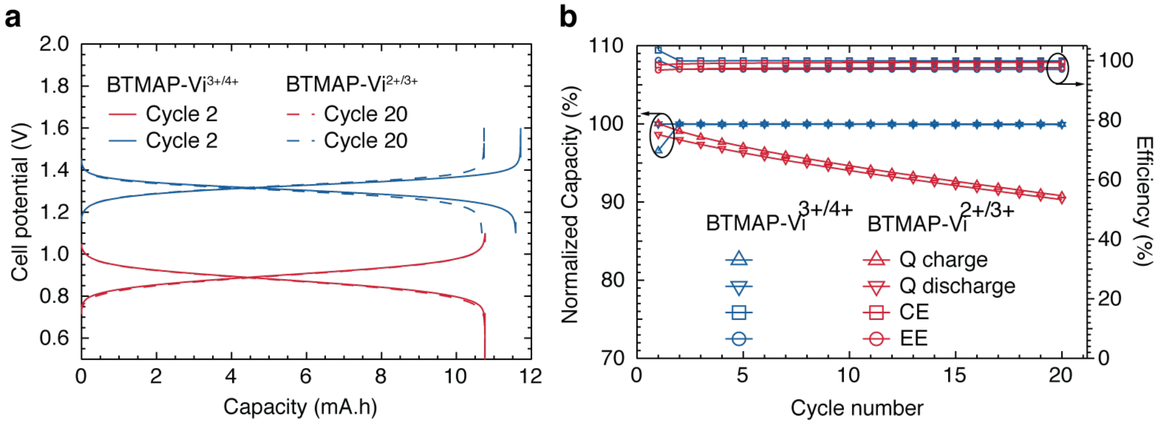

Figure A4.4. Cycling performance of 0.1 M BTMAP-Vi/0.1 M FcNCl RFB. To isolate the two redox states of BTMAP-Vi, 0.5-1.1 V and 1.1-1.6 V were used as cut-off voltages for the first and second redox state of BTMAP-Vi, respectively. **a**, Cell potential profile with respect to cell capacity using different redox states of BTMAP-Vi at the 2nd and 20th cycle, respectively. **b**, RFB charging capacity, discharging capacity, Coulombic efficiency and energy efficiency using different redox states of BTMAP-Vi. The comparison clearly shows that the 2nd redox state of BTMAP-Vi (E^0 = -0.703 V) is not as stable as the 1st redox state (E^0 = -0.353 V), possibly due to the reaction between BTMAP-Vi^{2+} and residual oxygen in the purge box.

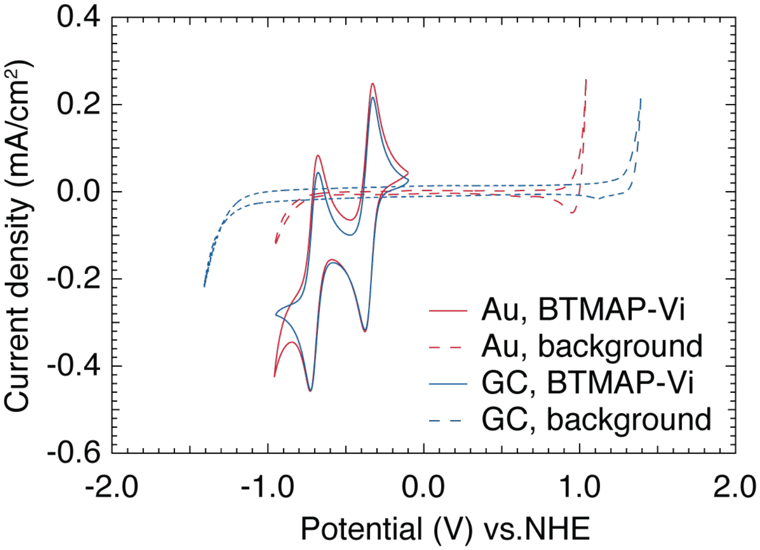

Figure A4.5. Cyclic voltammograms (CVs) of BTMAP-Vi on Au and glassy carbon (GC) electrode. CV was performed in 5 mM BTMAP-Vi/1.0 M NaCl electrolyte and 1.0 M NaCl background electrolyte. Due to the relatively low over potential for hydrogen evolution reaction (HER) on Au electrode, HER would compete with the reduction reaction of BTMAP-Vi^{3+} to BTMAP-Vi^{3+}. The downward bending tail in the solid red curve (between -0.96 to -0.85V) is the result of these two competing reactions. The overpotential for HER on GC is large enough so that HER won't compete with the redox reaction of BTMAP-Vi^{3+}.

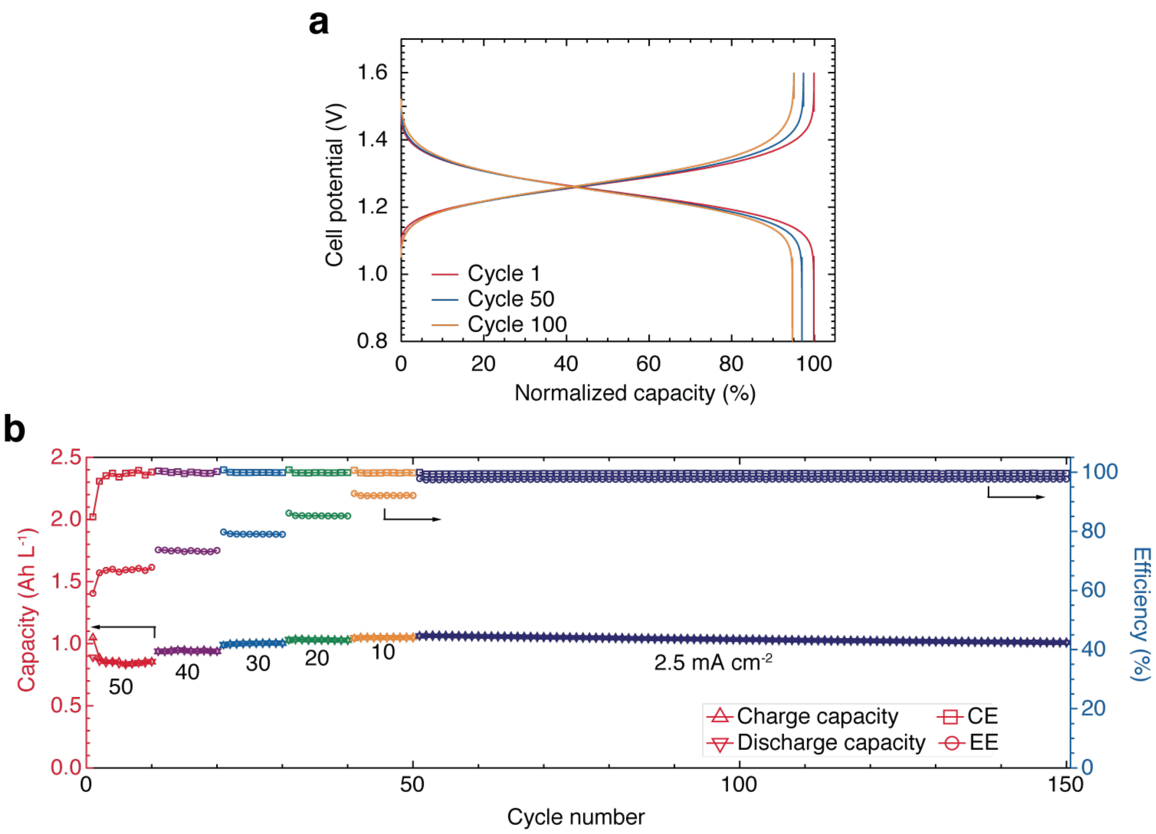

Figure A4.6. Cycling performance of 0.1 M BTMAP-Vi/0.1 M N^{Me}-TEMPO RFB. a, Cell potential profile with respect to the normalized capacity at the 1st, 50th and 100th cycle, respectively. **b.** RFB charging capacity, discharging capacity, Coulombic efficiency and energy efficiency at different galvanostatic current densities.

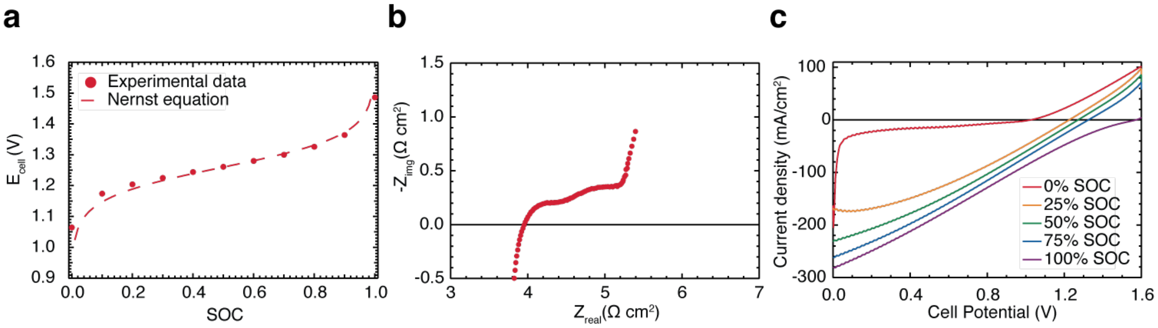

Figure A4.7. Detailed characterization of 0.1 M BTMAP-Vi/0.1 M N^{Me}-TEMPO RFB. a, Experimental and calculated (using a E_{cell}^0 of 1.26 V) open circuit voltage (OCV) of RFB at different SOCs. **b**, Electrochemical impedance spectroscopy (EIS) of RFB at 0% SOC. **c**, DC polarization curves of RFB at different SOCs.

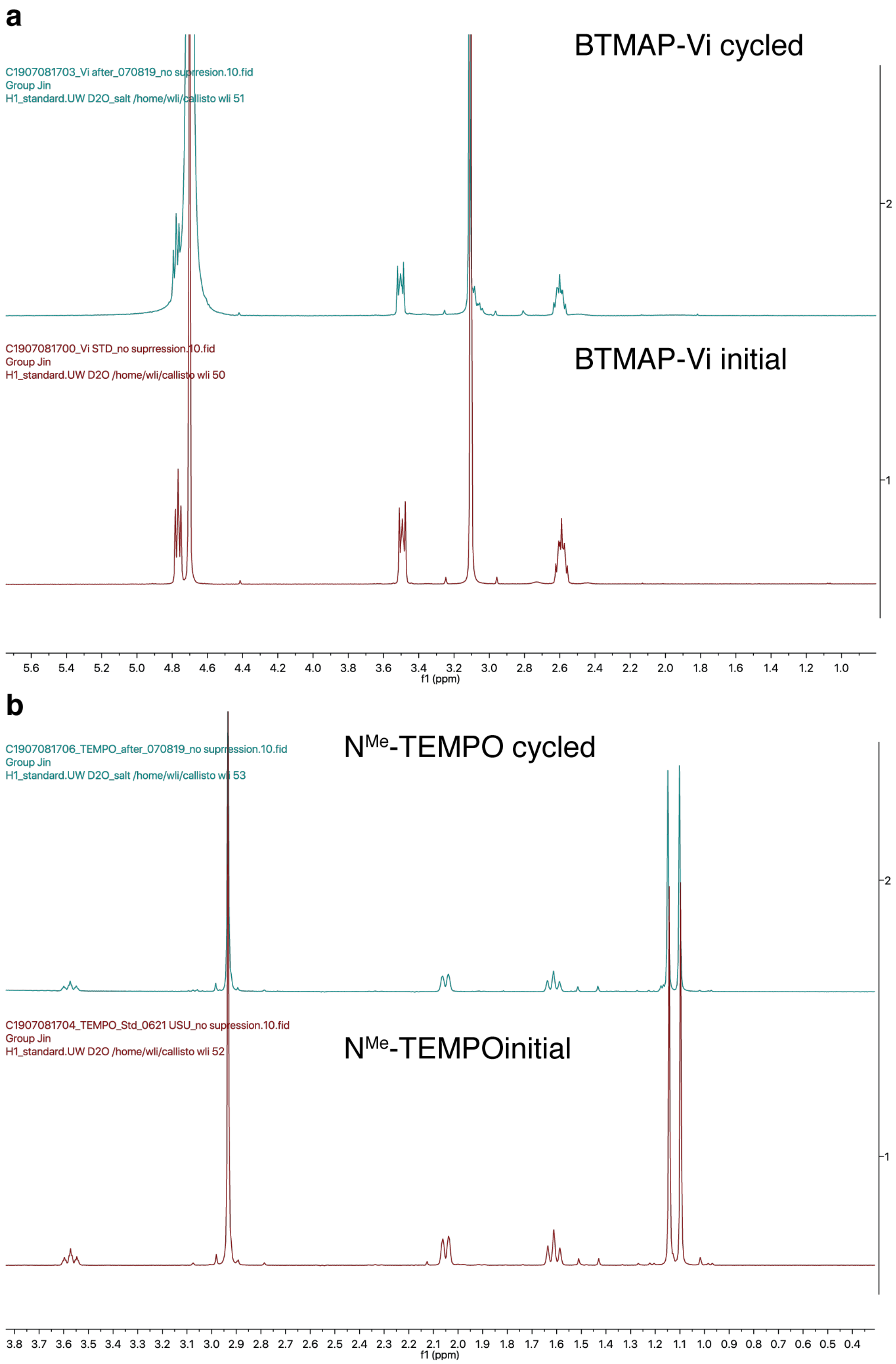

Figure A4.8. ^{1}H-NMR of redox couples before and after RFB cycling tests (150 cycles). a, ^{1}H-NMR of initial BTMAP-Vi (red curve) and cycled BTMAP-Vi (green curve). **b**, ^{1}H-NMR of initial N^{Me}-TEMPO (red curve) and cycled N^{Me}-TEMPO (green curve). Initial NMR spectra were collected with 5 mM active redox species in D_2O; cycled NMR spectral were collected with 1:20 dilution of RFB electrolytes (0.10 M redox species and 1.0 M NaCl in H_2O) in D_2O. 0.05 mL of phenylhydrazine was added to the NMR samples of N^{Me}-TEMPO to quench the radical.

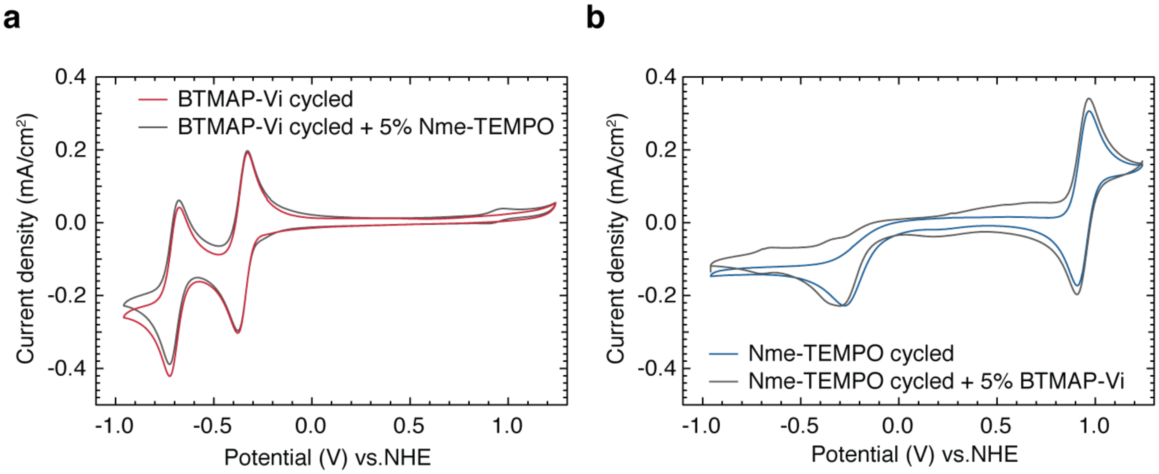

Figure A4.9. CV of electrolytes before and after RFB cycling tests (150 cycles). Cycled electrolytes (0.10 M redox species and 1.0 M NaCl) were diluted with 1.0 M NaCl in a 1:20 (electrolyte:NaCl) ratio. Additional redox species (5%) was added to show the effect of redox species crossover. **a**, CV of cycled BTMAP-Vi electrolyte before (red curve) and after (gray curve) adding 0.25 mM of additional N^{Me}-TEMPO. **b**, CV of cycled N^{Me}-TEMPO electrolyte before (blue curve) and after (gray curve) adding 0.25 mM of additional BTAMP-Vi. CV tests have confirmed a less than 5% crossover of both redox species after 100 cycles.

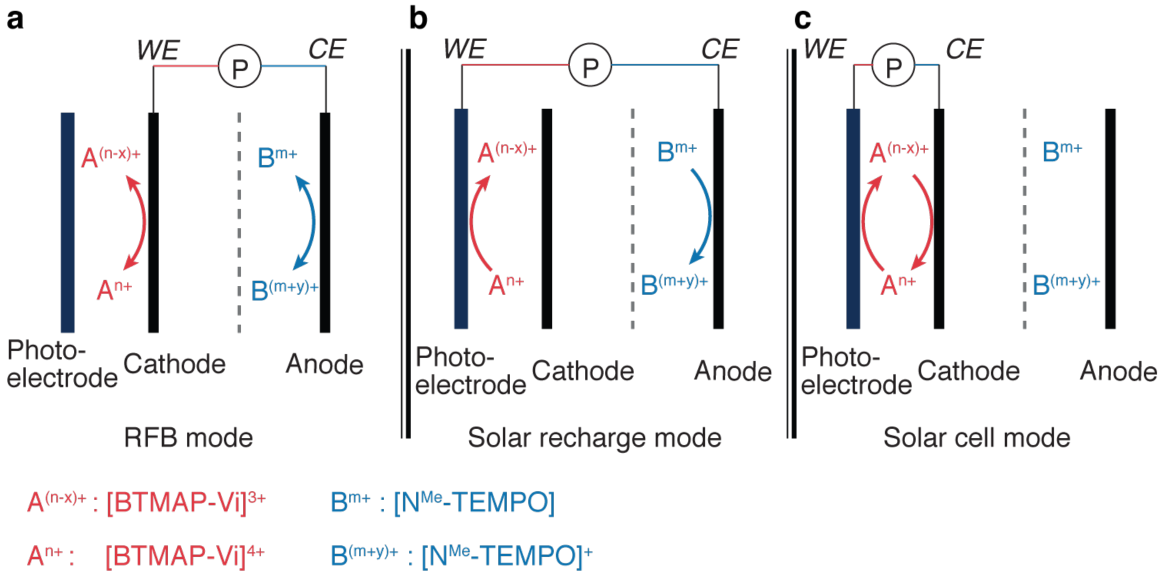

Figure A4.10. Operation modes of SFB. a, RFB mode using anode and cathode; **b**, solar recharge mode using photoelectrode and anode; **c**, solar cell mode using photoelectrode and cathode.